TAUP 2398-96
December 1996

Low–x physics at HERA

Aharon Levy

Raymond and Beverly Sackler Faculty of Exact Sciences
School of Physics, Tel Aviv University, Tel Aviv, Israel

Lectures given in the series of Strong Interactions Study Days
Kloster Banz, Germany, October 10–12, 1995

Contents

1 General Introduction **15**
- 1.1 HERA, H1 and ZEUS . . . 16
- 1.2 HERMES and HERA–B . . . 17
- 1.3 High Q^2 Neutral and Charged Currents . . . 19
- 1.4 Determination of the strong coupling α_S . . . 21
- 1.5 The strong rise of F_2 at low x . . . 22
- 1.6 Large rapidity gap events in DIS . . . 24
- 1.7 Summary . . . 24

2 Introduction to Regge Theory **27**
- 2.1 General introduction . . . 27
- 2.2 One pion exchange (OPE) . . . 28
- 2.3 s and t channel . . . 29
- 2.4 The Froissart bound . . . 30
- 2.5 Regge trajectories . . . 31
- 2.6 Shrinkage . . . 32
- 2.7 The Pomeron . . . 33
  - 2.7.1 The Pomeranchuk Theorem . . . 35
- 2.8 High energy behaviour of $\sigma_{\rm tot}$ . . . 36
  - 2.8.1 $\sigma_{\rm tot}(\gamma p)$ at HERA energies . . . 37
- 2.9 Summary . . . 39

3 Deep Inelastic Scattering at HERA **43**
- 3.1 Kinematics . . . 43
  - 3.1.1 The physical meaning of the Bjorken–x variable . . . 44
  - 3.1.2 Fixed target kinematics ($\vec{p} = 0$) . . . 45
  - 3.1.3 HERA kinematics . . . 47
- 3.2 Inelastic structure function . . . 50
  - 3.2.1 Flux of virtual photons . . . 51
  - 3.2.2 The ratio $R = \sigma_L/\sigma_T$ . . . 52
- 3.3 Radiative corrections . . . 53
- 3.4 Experimental determination of the structure functions . . . 56
- 3.5 Summary . . . 59

4 Parton Distributions in the Proton **61**
- 4.1 The QCD factorization theorem . . . 61
- 4.2 The QCD evolution equation for partons . . . 63
  - 4.2.1 DGLAP equations in leading order . . . 65
- 4.3 The behaviour of F_2 at low x . . . 67
- 4.4 The BFKL evolution equation . . . 68
  - 4.4.1 Some consequences from the BFKL equation . . . 70
  - 4.4.2 Signs for the BFKL dynamics . . . 71
- 4.5 The CCFM equation . . . 72
- 4.6 Saturation . . . 72
- 4.7 Parton parameterizations . . . 73
- 4.8 Gluon distribution in the proton at low x . . . 75
  - 4.8.1 The gluon density from global QCD fits . . . 76
  - 4.8.2 Extracting the gluon density from exclusive processes . . . 78
- 4.9 Summary . . . 83

5 Parton Distribution in the Photon **85**
- 5.1 Introduction . . . 85
- 5.2 Formalism . . . 88
- 5.3 Definition of photon structure functions . . . 90
  - 5.3.1 Definition of parton distributions in the photon . . . 90
- 5.4 Evolution equations for the photon . . . 93
  - 5.4.1 The resolved and direct photon interactions . . . 94
- 5.5 The theoretical importance of F_2^γ . . . 95
  - 5.5.1 Higher order corrections . . . 96
- 5.6 The experimental extraction of F_2^γ . . . 96
- 5.7 Parton distribution in the photon . . . 98
- 5.8 Parton distribution of a virtual photon . . . 100
- 5.9 Summary . . . 101

6 Diffraction in DIS **103**
- 6.1 General introduction . . . 103
- 6.2 Diffraction and regge formalism . . . 105
- 6.3 Diffraction in photoproduction at HERA . . . 108
  - 6.3.1 Ratios of cross sections . . . 111
- 6.4 Large rapidity gap events in DIS . . . 112
- 6.5 DIS on the Pomeron . . . 115
  - 6.5.1 Kinematical variables . . . 117

6.5.2 The diffractive structure function . . . 118
6.5.3 Factorization and the Pomeron structure function . . . 118
6.5.4 The partonic structure of the Pomeron . . . 119
6.5.5 The Pomeron intercept from DIS diffraction . . . 123
6.6 Summary . . . 127

7 Interplay Between Soft and Hard Interactions 129
7.1 Introduction . . . 129
7.2 Operational definition . . . 129
7.3 The models for the low x low Q^2 region . . . 131
7.3.1 Donnachie and Landshoff (DL) . . . 131
7.3.2 Capella, Kaidalov, Merino, Tran–Than–Van (CKMT) . . . 131
7.3.3 Badelek and Kwiecinski (BK) . . . 131
7.3.4 Abramowicz, Levin, Levy, Maor (ALLM) . . . 131
7.3.5 Some general comments . . . 131
7.3.6 Details of the parametrizations . . . 132
7.4 Comparison to data . . . 134
7.4.1 The total $\gamma^* p$ cross section, $\sigma_{tot}^{\gamma^* p}$ . . . 134
7.4.2 Vector meson production in γp and in $\gamma^* p$ . . . 136
7.5 DIS processes - hard or soft? . . . 141
7.6 Summary . . . 145

List of Figures

1.1 A contour of the x–Q^2 plane, indicating the regions covered by the fixed target experiments and those at the HERA collider. . . . 16
1.2 The H1 detector. . . . 17
1.3 The ZEUS detector. . . . 18
1.4 The delivered luminosity by HERA versus time for the years 1992–1995. . . . 18
1.5 A typical example of a neutral current event (upper part) and charged current event (lower part) as observed in the ZEUS detector. . . . 20
1.6 The differential cross section $\mathrm{d}\sigma/\mathrm{d}Q^2$ as function of Q^2 for NC and CC events as measured in the ZEUS detector using the 1993 data. The dashed line which does not describe the data assumes an infinite mass for the W. 21
1.7 Measured value of $\alpha_S(Q)$ for three different Q^2 regions. . . . 22
1.8 The structure function $F_2(x, Q^2)$ as function of Bjorken–x, for fixed Q^2 values. . . . 23
1.9 The total $\gamma^* p$ cross section as function of W^2, for different Q^2 values. The curves are the expectations of the ALLM parameterization. . . . 25
1.10 The distribution of the maximum rapidity $\eta_{\max}$ of a calorimeter cluster in a DIS event. . . . 26

2.1 Chew–Frautschi plot: Spin J versus mass squared for different mesons. The lines are the corresponding Regge trajectories. . . . 28
2.2 The ρ trajectory as determined from the charge exchange reaction $\pi^- p \to \pi^0 n$. . . . 31
2.3 $\frac{\mathrm{d}\sigma}{\mathrm{d}t}$ for different s for pp reactions. . . . 34
2.4 Total cross section measurements for various reactions. . . . 35
2.5 Total cross section differences for various reactions . . . 36
2.6 Fits of a simple Regge form containing two terms to total cross section measurements of pp, $\bar{p}p$, $\pi^{\pm}p$, $K^{\pm}p$, pn and $\bar{p}n$ reactions. . . . 38
2.7 A diagramatic example of a photoproduction event in the ZEUS detector, where the scattered electron is detected in the small angle electron calorimeter LUMIE. . . . 39

2.8 The HERA first measurement of $\sigma_{\mathrm{tot}}(\gamma p)$, together with lower energy data. The curves are predictions of different models for the HERA energy range region. . . . 40

3.1 Deep inelastic lepton–proton–scattering. . . . 43
3.2 Explanation of the Bjorken x variable . . . 45
3.3 A sketch for understanding the Jacquet–Blondel method. . . . 48
3.4 The two angles used in the double angle method. . . . 49
3.5 The differential cross section as function of the photon polarization ϵ for fixed ν and Q^2. . . . 54
3.6 QED radiative corrections: (a) from the lepton line, (c) from the quark lines, and (b) from their interference. . . . 55
3.7 The structure function $F_2(x, Q^2)$ as function of Q^2, for fixed x values. . . . 58

4.1 Diagram showing the increase in local density in an evolution in x. . . . 71
4.2 Diagram showing the evolution from point (x_0, Q_0^2) to (x, Q^2). . . . 72
4.3 Parameterizations of parton distributions compared to ZEUS and H1 data. 75
4.4 $\sigma_{tot}(\gamma^* p)$ vs W^2 compared to the GRV parameterization. . . . 76
4.5 Low Q^2 measurements of the F_2 structure function at HERA, compared to the GRV and DL parameterizations. . . . 77
4.6 The gluon density distribution, $xg(x)$, as function of x at a fixed Q^2 of 20 GeV^2, obtained from LO and NLO approximate methods (Prytz and EKL). The result of a global fit is shown for comparison. . . . 78
4.7 The gluon density distribution, $xg(x)$, as function of x at a fixed Q^2 of 20 GeV^2, obtained from a NLO QCD analysis of F_2. . . . 79
4.8 The gluon density distribution as function of x at $Q^2 = 30\,\mathrm{GeV}^2$ as determined from a leading order analysis of 2–jet events. The results are compared with those from a global QCD fit and from an approximate method. . . . 80
4.9 Inelastic J/Ψ cross section data as function of W compared with different choices of gluon distribution in the proton. . . . 81
4.10 $M(K\pi)$ (top) and ΔM (bottom) distributions for events with $143 < \Delta M < 148\,\mathrm{MeV}$ and $1.80 < M(K\pi) < 1.92\,\mathrm{GeV}$. . . . 82
4.11 The cross section measurements for the process $\gamma p \to c\bar{c}X$ as function of the γp center of mass energy W. The solid and dashed lines represent predictions on NLO calculations using different gluon density shapes. . . . 83
4.12 Elastic J/Ψ cross section data as function of W compared with different choices of gluon distribution in the proton. . . . 84

5.1 Two–photon exchange in e^+e^- scattering. . . . 88
5.2 The photon structure function as function of Q^2 for different x intervals. . 92
5.3 The splitting functions utilized in the DGLAP equations for the photon. . 93

5.4 Diagrams representing direct and resolved photon interactions. 94
5.5 The x_γ distribution as obtained from two jet events, compared to direct and resolved photon interactions as simulated by Monte Carlo generators, . . . 95
5.6 Comparison between the visible and the true W. 97
5.7 Comparison of the data on energy flow as function of the pseudorapidity with predictions of different Monte Carlo generators. The Q^2 values are in units of GeV^2. 97
5.8 Compilation of all existing data on F_2^γ, compared to predictions of some parton parameterizations. 98
5.9 The estimated gluon density distribution in the photon, $x_\gamma g(x_\gamma)/\alpha$, compared to predictions of some parameterizations. 99
5.10 The $x_\gamma^{\rm obs}$ distribution (a) for photons of virtuality $0.1 < P^2 < 0.6\,{\rm GeV}^2$ and (b) for quasi–real photons. 100
5.11 The ratio of resolved to direct photon reactions as a function of the photon virtuality P^2. 101

6.1 The dependence of the slope b on the laboratory momentum of the incoming projectile for (a) pp elastic scattering and for (b) $\pi^- p$ elastic scattering. On the right–hand side of the vertical axis the scale is the total cross section σ_T for (a) pp and (b) $\pi^- p$ reaction. The corresponding data are approximated by the solid line. 106
6.2 The differential cross section for the inelastic diffractive reaction $pp \to Xp$ as function of the scaled diffractive mass M_X^2/s. 107
6.3 The rapidity distribution of the different photoproduction processes at HERA. The regions covered by the ZEUS detector are indicated. 110
6.4 The total photoproduction cross section measurements at HERA and at lower energies, compared to different models. 111
6.5 The contribution of the (a) elastic and (b) single diffraction processes relative to the total cross section for hadron–proton and γ–proton interactions. . . 112
6.6 A DIS NC event in the ZEUS detector which has a large rapidity gap between the outgoing proton and the other produced particles in the ep collision. . 113
6.7 The energy flow of DIS events without a large rapidity gap (open dots) and those with a large rapidity gap ($\eta_{\rm max} < 1.8$, full dots), for different x, Q^2 bins. 114
6.8 The F_2 structure function for the inclusive DIS sample (open circles) and for the large rapidity gap events (full dots) as function of Bjorken–x, for fixed Q^2 intervals. On the right hand side of the figure, their ratio is plotted as function of x for the same Q^2 intervals. 115
6.9 The x of two–jet events in diffractive proton dissociation in the UA8 experiment. 116

6.10 (a) Transverse energy deposition in η–ϕ space for a large rapidity gap event with one hadronic jet balancing the electron's transverse momentum. (b) A similar display for a large rapidity gap two–jet event. 116
6.11 The distribution of the total hadronic transverse energy seen in the calorimeter E_T, for DIS events with a large rapidity gap and those with, in addition, ≥ 1 (hashed) and ≥ 2 jets (cross-hashed). On the left hand side, the quantity in the ep frame is presented while on the right hand side, in the $\gamma^* p$ frame. 117
6.12 Diagram of a diffractive event. 118
6.13 The diffractive structure function $F_2^{D(3)}$ as a function of $x_{I\!P}$ for fixed β and Q^2 intervals. 120
6.14 The results of $F_2^{D(3)}$ compared to an Ingelman–Schlein type model for which the momentum sum rule (MSR) for quarks within the Pomeron is assumed. 121
6.15 Measured differential cross section for inclusive jet production for $E_T^{\rm jet} > 8\,{\rm GeV}$ in the kinematic region $Q^2 < 4\,{\rm GeV}^2$. The shaded band displays the uncertainty due to the energy scale of the jets. The lines are predictions using the POMPYT generator for various parameterizations of the Pomeron parton densities. 122
6.16 The plane of the variables $\Sigma_{I\!P}$ (momentum sum) and c_g (relative contribution of hard gluons in the Pomeron). The thick solid line displays the minimum for each value of c_g obtained from the χ^2 fit (the shaded area represents the $1\,\sigma$ band around these minima) to the measured ${\rm d}\sigma/{\rm d}\eta^{\rm jet}(\eta_{\rm max}^{\rm had} < 1.8)$ using the predictions of POMPYT. The constraint imposed in the $\Sigma_{I\!P} - c_g$ plane by the measurement of the diffractive structure function in DIS ($F_2^{D(3)}$) for two choices of the number of flavours (upper dot-dashed line for $\Sigma_{I\!P q} = 0.40$ and lower dot-dashed line for $\Sigma_{I\!P q} = 0.32$) is also shown. The horizontal dashed line displays the relation $\Sigma_{I\!P} = 1$. 123
6.17 The Pomeron structure function $\tilde{F}_2^{I\!P}(\beta, Q^2)$ as function of Q^2 for fixed β regions (left hand side). The gluon momentum density distribution at a scale of $Q^2 = 5\,{\rm GeV}^2$ (upper right hand side). The evolution of the fractional momentum carried by the partons in the Pomeron as function of Q^2 (lower right hand side). 124
6.18 The dependence of the exponent of the Pomeron flux n on (a) β and on (b) Q^2. 125
6.19 Differential cross section ${\rm d}\sigma/{\rm d}t$ for diffractive DIS events with a leading proton with a longitudinal momentum fraction $x_L > 0.97$, in the range $4 < Q^2 < 30\,{\rm GeV}^2$, $70 < W < 210\,{\rm GeV}$ and $0.02 < \beta < 0.4$. 126
6.20 Distribution of $\ln M_X^2$ for the W intervals indicated at $Q^2 = 31\,{\rm GeV}^2$. The solid lines show the extrapolation of the non–diffractive background. . . . 127

7.1 The total $\gamma^* p$ cross section as function of W^2 from the F_2 measurements for different Q^2 values. The lines are the expectations of a new ALLM type parametrization. 135
7.2 The Q^2 dependence of the parameter Δ obtained from a fit of the expression $\sigma_{tot}^{\gamma^* p} = \sigma_1 W^{2\Delta}$ to the data in each Q^2 bin. The curves are the expectations of the parameterizations mentioned in the text. 136
7.3 The total and 'elastic' vector meson photoproduction measurements as function of W, for the vector mesons ρ, ω, ϕ and J/Ψ. The curve to the total photoproduction cross section is the DL parametrization ($W^{0.16}$). The other lines are curves of the form $W^{0.22}$ and $W^{0.8}$. 137
7.4 The dependence of the cross section for the reaction $\gamma^* p \to \rho^0 p$ on W, for different Q^2 values. 138
7.5 The dependence of the cross section for the reaction $\gamma^* p \to \phi p$ on W, for different Q^2 values. 139
7.6 The dependence of the cross section for the reaction $\gamma^* p \to J/\Psi p$ on W, for different Q^2 values. 140
7.7 The ratio of the cross sections of vector mesons ϕ, ρ', J/Ψ and Ψ' to ρ^0 at different values of Q^2 as indicated in the figure. 141
7.8 The dependence of the slope of the differential cross section 142
7.9 The dependence of the slope of the differential cross section for the reaction $\gamma^* p \to \rho^0 p$ on W, for $8 < Q^2 < 50\,\mathrm{GeV}^2$ (H1) and $5 < Q^2 < 30\,\mathrm{GeV}^2$ (ZEUS). The NMC data point is at $Q^2 \approx 10\,\mathrm{GeV}^2$. 143
7.10 The dependence of the slope of the differential cross section for the reactions $\gamma^* p \to \rho^0 p$ (left) and $\gamma^* p \to J/\Psi p$ (right) on Q^2, for $< W > \approx 80\,\mathrm{GeV}$ (ρ^0) and $90\,\mathrm{GeV}$ (J/Ψ). 143
7.11 Fluctuation of the photon into a $q\bar{q}$ pair in (a) asymmetric small k_T configuration, (b) into a symmetric large k_T configuration 144
7.12 Diagrams describing examples of (a) 'direct' photon process, (b) 'resolved' photon process 145

List of Tables

2.1 Coefficients α_{eff} and the possible exchanged–particles for various processes. 33

6.1 Cross–section for the different diffractive contributions at $W = 200$ GeV. . 110

7.1 Expected behaviour of soft and hard processes. 130

Chapter 1

General Introduction

The dynamical structure of the proton [1] evolved from the pioneering deep inelastic scattering (DIS) experiments at SLAC, through higher energy fixed target lepton–proton DIS measurements till the present results of the HERA ep collider. The proton has three valence quarks and a vast number of additional sea partons, each carrying a fraction x of the proton's momentum. This information is obtained by 'looking' at the proton with a probe of virtuality represented by its negative squared mass Q^2. The higher the Q^2 the smaller the objects 'inside' the proton that can be 'observed'. These objects carry a fraction x of the proton's momentum. The regions in the x–Q^2 plane studied before HERA started to operate were up to about $300\,\mathrm{GeV}^2$ in Q^2 and down to about 10^{-2} in x. The HERA collider has extended the plane in both directions by more than two orders of magnitude, as can be seen in figure 1.1.

What do we expect to learn in this new kinematic region? How does the proton 'look' when probed at very high Q^2? Can one detect substructure in the partons or in the electron? Are there 'exotic' particles such as leptoquarks? Can one detect supersymmetric particles? What is the x distribution of the partons within the proton when probed at different values of Q^2? How many partons are there as x becomes smaller and smaller?

The above is only a partial list of questions hoped to be answered by the HERA data. The topic of these lectures is 'Low–x physics at HERA'. Studying the low–x region actually means studying the high probe–proton center of mass energy W. We will discuss the new results obtained in this wider kinematic region. Since high energy phenomena have been well described within the Regge picture, there will be a chapter devoted to this subject. Next, the DIS kinematics will be introduced and the proton structure functions will be defined. This will lead to the chapter discussing the QCD factorization theorem, the definitions of the parton distributions and their evolution with Q^2, with a special emphasis on their behaviour at low x. The DGLAP and the BFKL evolution equations will be reviewed, different parton density parameterizations will be compared and some methods to obtain the gluon density distribution in the proton will be described. The following chapter discusses the structure function of the photon, the parton density distributions

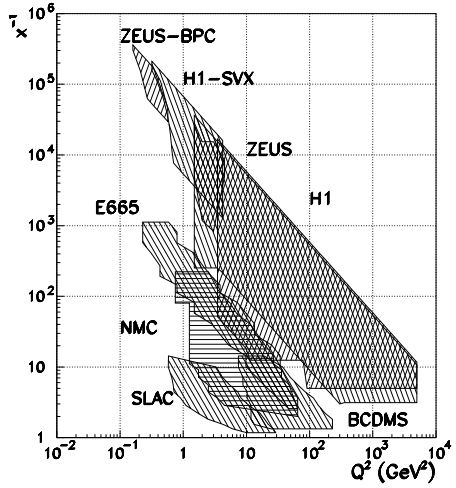

Figure 1.1: A contour of the x–Q^2 plane, indicating the regions covered by the fixed target experiments and those at the HERA collider.

in the photon and the picture of the photon, real and virtual, emerging from the HERA results. One of the unexpected results of HERA, diffraction in DIS, is preceded in the next chapter by a general introduction about diffraction in hadroproduction, the concept of the Pomeron is introduced and the large rapidity gap events in DIS are analysed from the point of view of a partonic structure of the Pomeron. The final chapter is an attempt to give an operational definition to 'hard' and 'soft' interactions and the interplay between the two. This will include a discussion about the energy behaviour of the total DIS cross section as well as that of exclusive production of vector meson in DIS.

Before indulging on this extensive program, I would like, as part of this general introductory chapter, to summarize the highlights of the HERA results so far. We start with a short description of the machine and the two detectors.

1.1 HERA, H1 and ZEUS

HERA [2] is the $e^{\pm}p$ colliding beam facility at DESY in Hamburg. It collides at present $27.5\,\mathrm{GeV}$ $e^{\pm}$ with $820\,\mathrm{GeV}$ protons, providing a center–of–mass energy of $300\,\mathrm{GeV}$. The two beams can be stored in up to 210 bunches each, and collide every 96 nanoseconds at two interaction points.

Each of the two interaction regions is surrounded by a 4π detector. In the so–called north hall, the H1 detector [3] is stationed, while the ZEUS detector [4] is in the south

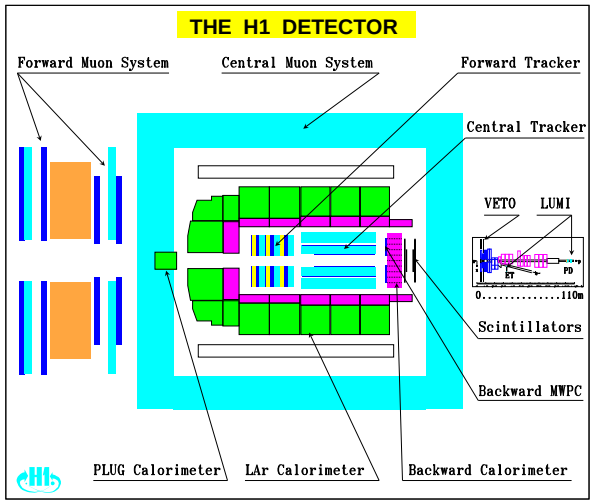

Figure 1.2: The H1 detector.

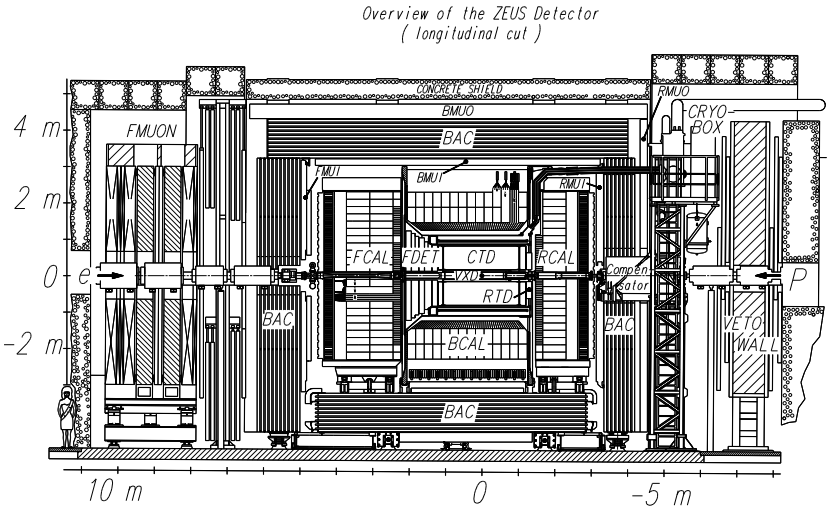

Figure 1.3: The ZEUS detector.

hall. Both detectors use a sampling calorimeter, tracking detectors and muon detectors. The H1 detector is depicted in figure 1.2 and the ZEUS detector is shown in figure 1.3.

Both the H1 and the ZEUS experiments have additional detectors downstream and upstream up to a distance of about 100 meters from the interaction point. Their purpose is to measure protons and neutrons in the proton beam direction (denoted throughout this text as the 'forward' region), and electrons and photons in the electron beam direction. The photon detector is used to measure the luminosity by using the bremsstrahlung process $ep \to ep\gamma$ which can be accurately calculated through Quantum Electrodynamics (QED). This measurement provides the luminosity with an accuracy of about 1–2 %.

As is the case with any new machine, the integrated luminosity starts at a low value but gradually keeps increasing, as shown in figure 1.4.

The present level of luminosities is very well suited for studying the low and intermediate Q^2 physics. It is planned to upgrade [5] HERA in about 2–3 years to increase the integrated luminosity by an order of magnitude by going to the low β mode.

1.2 HERMES and HERA–B

The two beams are in separate rings and can be used also for other purposes. Thus, in addition to the two collision points, the electron beam, which can have a polarization of about 60 %, interacts with a polarized stationary target. At that interaction point, situated

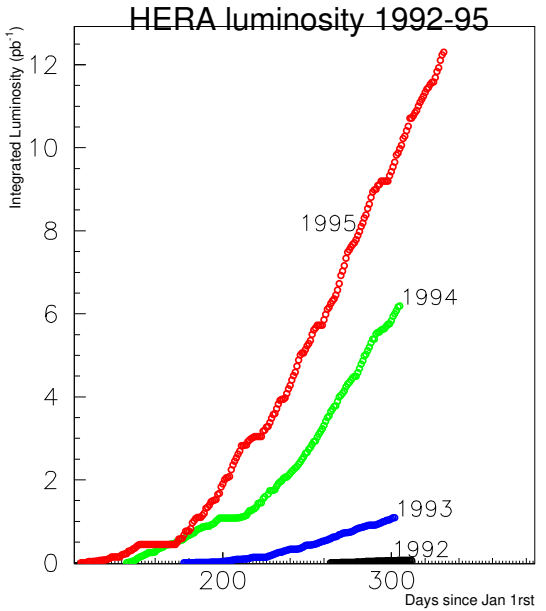

Figure 1.4: The delivered luminosity by HERA versus time for the years 1992–1995.

in the east straight section, the HERMES detector [6] records the results of the interactions of the polarized particles. The aim of this experiment is to investigate the origin of proton and neutron spin in inelastic electron–nucleon collision.

The proton beam will be used by the HERA–B experiment [7] to be installed in the west area. This experiment will use the halo of the proton beam to produce B–mesons. The experiment objective is to study CP violation in the B–meson system.

1.3 High Q^2 Neutral and Charged Currents

The ep reactions can be classified into two categories. The events in which the outgoing lepton is an electron are called neutral current (NC) events. In this case the particle exchanged between the initial lepton and the proton is a neutral particle, predominantly a γ at lower Q^2 values and when Q^2 becomes high enough the Z^0 starts to also contribute appreciably. The other class of events are those where the outgoing lepton is a neutrino. In this case the charged $W^{\pm}$ is exchanged and the events are called charged current (CC) events. These two classes of events can be represented by the two simple exchange diagrams below:

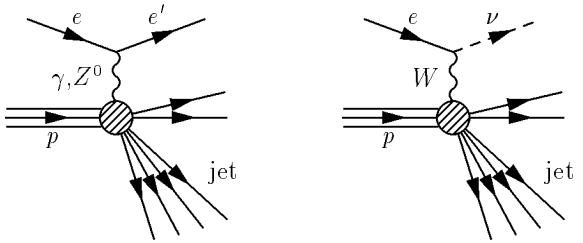

(1.1)

neutral current DIS charged current DIS

The NC events can be identified by observing the scattered electron which makes sure to balance the transverse momentum, p_T. In the case of CC events, the neutrino is undetected, resulting in a large missing transverse momentum. Figure 1.5 shows on the top a typical NC event in the ZEUS detector, where one sees the scattered electron leaving a track in the central tracking detector and depositing energy in the rear part of the calorimeter (RCAL). The current jet is produced in the upper part of the forward calorimeter (FCAL) and the remnants of the proton produce energy in FCAL around the beam pipe. In the lower part of the figure one sees an example of a CC event, identified by the large missing p_T. Also here one can see the current jet and the remnants depositing energy in the FCAL.

Using the transverse momentum information and the electron identification it is possible for both (e^+ and e^-) beams to isolate the NC and CC events. In the 1993 data sample 436 NC events and 23 CC events with $Q^2 > 400\,\mathrm{GeV}^2$ were found.

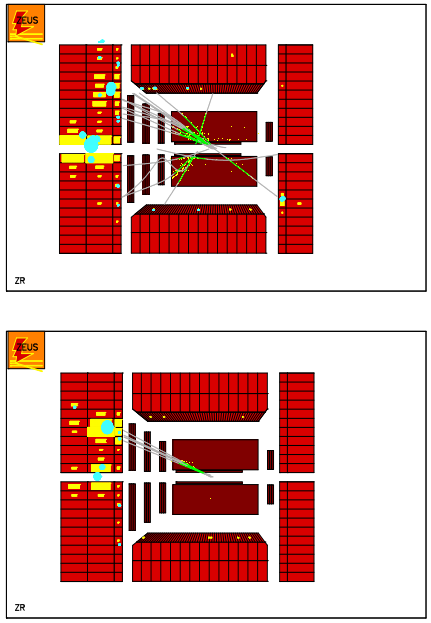

Figure 1.5: A typical example of a neutral current event (upper part) and charged current event (lower part) as observed in the ZEUS detector.

The cross–section for the unpolarized e^-p NC DIS can be expressed as [8]:

$$\frac{\mathrm{d}^2\sigma}{\mathrm{d}x\,\mathrm{d}Q^2} = \frac{2\pi\alpha^2}{xQ^4}\left\{\left[1+(1-y)^2\right]\mathcal{F}_2 + \left[1-(1-y)^2\right]x\mathcal{F}_3\right\} \tag{1.2}$$

The NC structure function $\mathcal{F}_2$ can be written as:

$$\mathcal{F}_2^{NC} = \sum_f q_f^+\left[e_f^2 + 2v_e v_f e_f\left(\frac{Q^2}{Q^2+M_Z^2}\right) + \left(v_e^2+a_e^2\right)\left(v_f^2+a_f^2\right)\left(\frac{Q^2}{Q^2+M_Z^2}\right)^2\right] \tag{1.3}$$

where q_f^+ is the sum of the momentum density distributions of the quarks and antiquarks of flavour f, each having the electric charge e_f. The a's and the v's are axial and vector couplings of the electron or the quark to the Z^0 which has the mass M_Z.

For CC reactions, neglecting heavy quarks, the cross section is given by:

$$\frac{\mathrm{d}^2\sigma}{\mathrm{d}x\mathrm{d}Q^2} = \frac{G_F^2}{2\pi}\left(\frac{M_W^2}{M_W^2+Q^2}\right)^2 2x\cos^2\theta_c\left[u+c+(1-y)^2\left(\overline{d}+\overline{s}\right)\right] \tag{1.4}$$

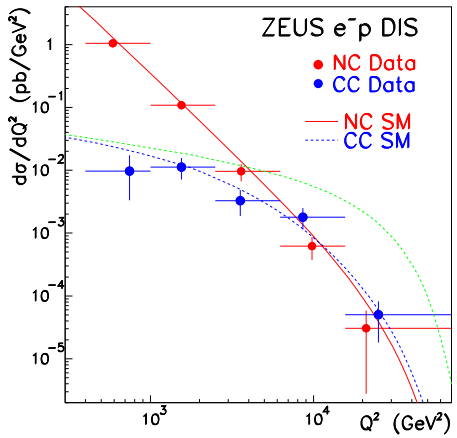

Figure 1.6: The differential cross section $\mathrm{d}\sigma/\mathrm{d}Q^2$ as function of Q^2 for NC and CC events as measured in the ZEUS detector using the 1993 data. The dashed line which does not describe the data assumes an infinite mass for the W.

where G_F is the Fermi constant and M_W is the mass of the W.

While the CC events are produced purely by a weak interaction, the NC events will be dominanted by electromagnetic interactions at lower Q^2, while at higher Q^2 the weak interactions will start to play an important role. The expectations were thus that at some high enough value of Q^2 the cross sections of the NC and CC will be of comparable magnitude. These expectations have been borne out by the first HERA data, taken in 1993 where both collaborations, H1 [9] and ZEUS [10] have measured NC and CC events at high Q^2. The differential cross section of the NC and CC reactions as function of Q^2 are shown in figure 1.6.

One can see that in the region of Q^2 of the order of M_Z^2, the two cross sections are equal. In addition one observes that the shape of the CC cross section is sensitive to the W mass. By fitting the distribution to equation 1.4, one obtains the result $M_W = 76 \pm 16 \pm 13\,\mathrm{GeV}$.

1.4 Determination of the strong coupling α_S

Multi–jet production in NC DIS events can be used to determine the strong coupling constant α_S. In particular, the measured rate of $2+1$ jets, where the '+1' stands for the proton remnant jet, can be compared to theoretical calculations in which α_S is the only free parameter.

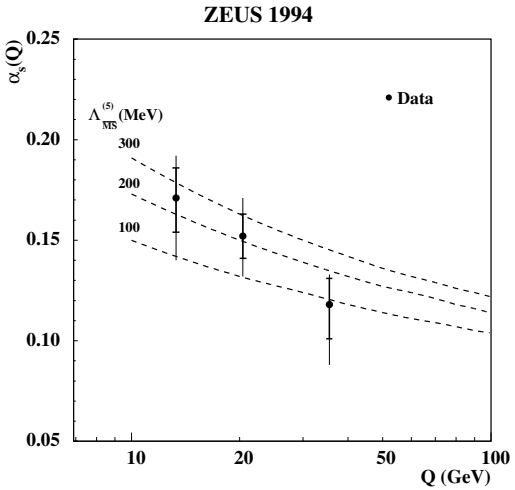

Figure 1.7: Measured value of $\alpha_S(Q)$ for three different Q^2 regions.

By using some kinematical cuts [11] which exclude the problematic region where higher order effects are important and jets are not well measured in the experiment, the value of α_S was determined [12, 13] in three Q^2 regions in the range $120 < Q^2 < 3600\,\mathrm{GeV}^2$, and was found to decrease with Q^2 (figure 1.7), consistent with the running of the strong coupling constant.

The value of α_S expressed at the Z^0 mass was determined to be:

$$\alpha_S(M_{Z^0}) = 0.117 \ \pm 0.005(\mathrm{stat}) \ {}^{+0.004}_{-0.005}(\mathrm{sys_{exp}}) \ \pm 0.007(\mathrm{sys_{th}})$$

which is in good agreement with the results obtained from the e^+e^- event shape (0.121 ± 0.006) and Z^0 width (0.124 ± 0.007).

1.5 The strong rise of F_2 at low x

From the measurements of the cross section of NC DIS events one can unfold the proton structure function [14] F_2 which is a function of x and of Q^2. The data from fixed target experiments indicated that for a given value of Q^2 the structure function F_2 rose slowly with decreasing x and seemed to level off with further decrease. The new data [15, 16] of HERA, which allowed to measure F_2 for higher Q^2 and lower x, showed that it rises sharply with decreasing x. This can be seen in figure 1.8 where the measurements of F_2 are shown for Q^2 values from $1.5\,\mathrm{GeV}^2$ up to $5000\,\mathrm{GeV}^2$ and down to x values close to 10^{-5}. The

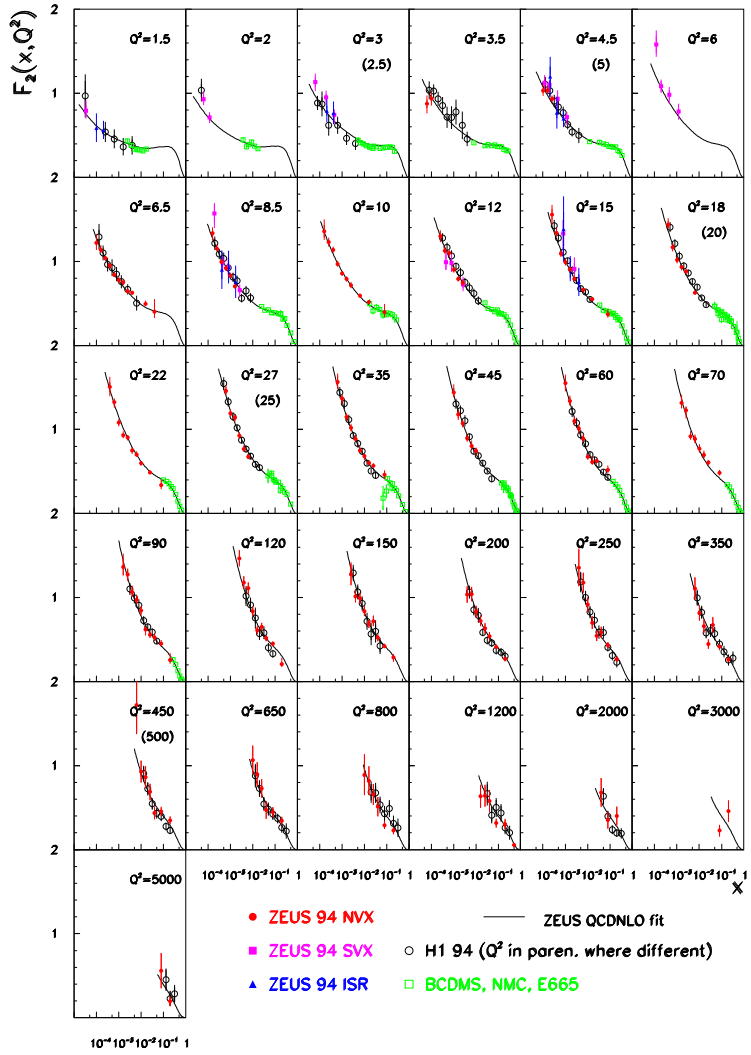

Figure 1.8: The structure function $F_2(x, Q^2)$ as function of Bjorken–x, for fixed Q^2 values.

rise with decreasing x is associated to the increase of the gluon density as x gets smaller. One can see from the lines in figure 1.8 that QCD can accommodate this behaviour in the whole kinematic region where data exist.

Another way [17] to look at the behaviour of F_2 is through its connection to the total $\gamma^* p$ cross section:

$$\sigma_{tot}(\gamma^* p) = \frac{4\pi^2\alpha}{Q^2(1-x)} \frac{Q^2 + 4m_p^2 x^2}{Q^2} F_2(W^2, Q^2) \tag{1.5}$$

Figure 1.9 shows the behaviour of $\sigma_{tot}(\gamma^* p)$ as calculated from the data of $F_2(W^2, Q^2)$ through equation 1.5. Also included are measurements of the real γp cross sections as function of W^2. The curves are the expectations of the ALLM [18, 19] parameterization. While the real photoproduction cross section shows a mild rise with energy, one sees a steeper rise for the higher Q^2 data. There clearly is a transition. At which Q^2 value does it happen? Is it gradual or is it sharp? What does the transition mean? We will discuss these questions in later chapters.

1.6 Large rapidity gap events in DIS

The characteristic topology of a NC DIS event is expected to include a current jet as a result of the interaction of the probing virtual photon with one of the partons from the proton. In addition there is the proton remnant jet, usually concentrating around the beam pipe. The region between the two is filled with more particles resulting from colour forces and gluon radiation. Thus the distribution of the angle θ between a produced particle and the incoming proton direction, or equivalently the pseudorapidity η, defined as $\eta = -\ln\tan\theta/2$, is expected to fall exponentially.

One can look at the variable $\eta_{\max}$, defined as the maximum rapidity of a calorimeter cluster of DIS events, displayed in figure 1.10. While the shaded area is the behaviour which was expected of $\eta_{\max}$ as described above, the data [20] had a large excess of events in the region of $\eta_{\max} < 1.5$. This corresponds to events with a large rapidity gap, of at least 2.8 units. The properties of these events were consistent with being diffractively produced. Thus the HERA experiments [20, 21] found that about 10 % of all the DIS events are due to a diffractive process, a fact that came as a surprise and was not included in any of the DIS generators written before the HERA experiments.

1.7 Summary

In this introductory chapter, some of the highlights of HERA have been described in a very general way. The following have been mentioned:

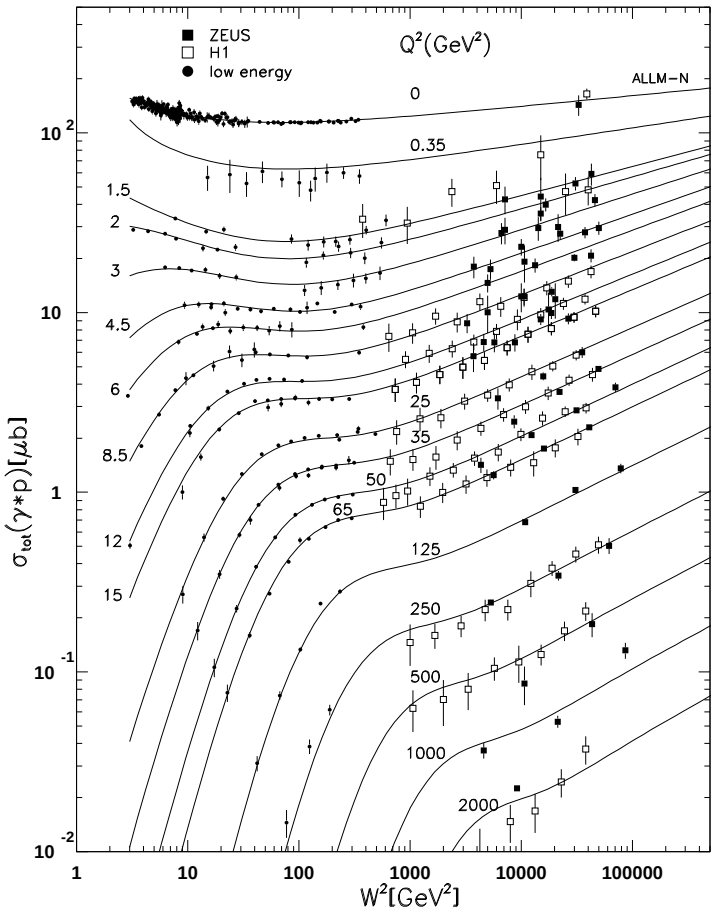

Figure 1.9: The total $\gamma^* p$ cross section as function of W^2, for different Q^2 values. The curves are the expectations of the ALLM parameterization.

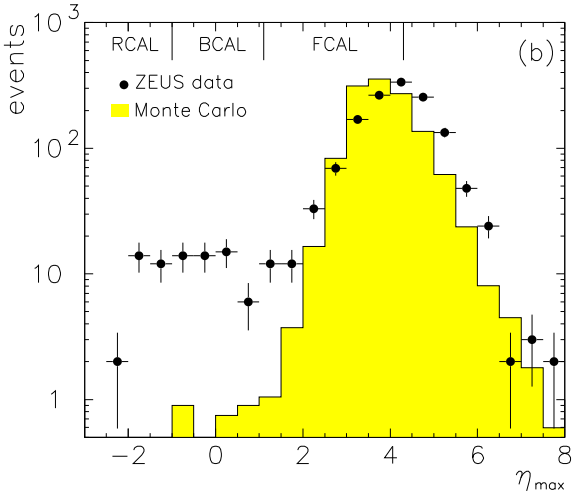

Figure 1.10: The distribution of the maximum rapidity $\eta_{\max}$ of a calorimeter cluster in a DIS event.

- The first experimental evidence to the expectation of the electroweak theory that when Q^2 is close to M_Z^2, the electromagnetic and the weak force become of equal magnitude.
- From the jet rates of the NC DIS events one can determine α_S with high precision and can observe the running of α_S in one experiment.
- The proton structure function $F_2(x, Q^2)$ shows a dramatic increase as x decreases for a large span of Q^2 values.
- Large rapidity gap events were observed in NC DIS reactions, indicating the presence of diffractive mechanisms also at higher Q^2.

The first two items do not belong to the scope of these lectures and thus one is referred to the original publications for further details. The last two items will be expanded in the future chapters.

Chapter 2

Introduction to Regge Theory

2.1 General introduction

Our understanding of particle physics has evolved in two directions. The static properties of the hadronic spectrum profitted from the breakthrough of the SU(3) theory of Gell–Mann and Ne'eman [22], which relates particles of different internal quantum numbers but the same spin–parity (and mass, in perfect SU(3) symmetry). The hadron dynamics has been investigated by many theories. One of the successful ones which we will describe in more detail here is the Regge theory [23, 24].

The Regge theory investigates the dynamics of hadrons by studying the two–particle scattering $A + B \to C + D$. It relates the spin J and the mass M of particles with the same internal quantum numbers (strangeness, isospin, baryon number, etc.). When one plots all known particles in the Chew–Frautschi [25] plane (J vs M^2) they all seem to lie on a straight line called a Regge trajectory. As an example we show this plot for some of the meson particles (figure 2.1). A similar one exists for the baryons.

The Regge theory predicts some characteristics which can be tested experimentally for the behaviour of hadronic interactions at high energies. One such prediction is that the high energy behaviour of all processes where one exchanges the same quantum numbers should be similar.

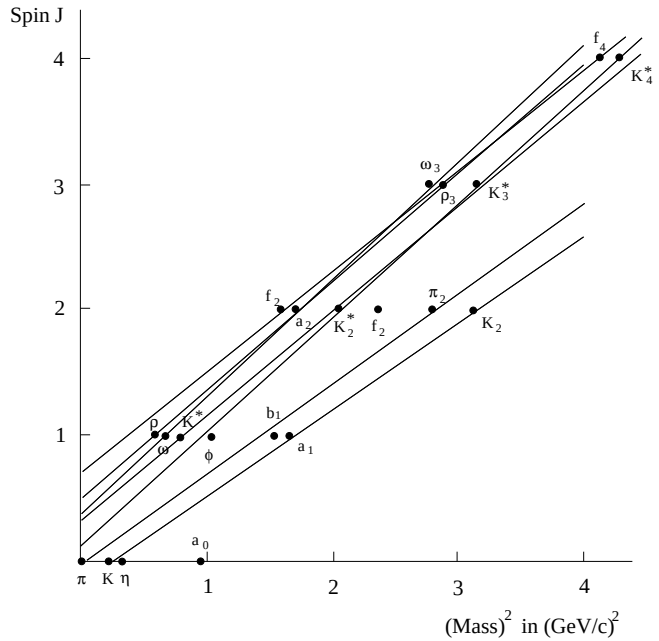

Figure 2.1: Chew–Frautschi plot: Spin J versus mass squared for different mesons. The lines are the corresponding Regge trajectories.

2.2 One pion exchange (OPE)

The early description of two-body reactions was the picture of one pion exchange (OPE). For instance, the reaction $\pi p \to \rho p$ could be well described by the following diagram:

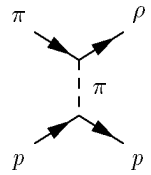

(2.1)

It was realized soon that this picture is incomplete. There is no justification for ignoring the exchange of two or more pions or of other particles. In some reactions the exchange of a pion is even not possible, like in elastic πp scattering where, due to G–parity, one cannot

exchange a pion but a ρ:

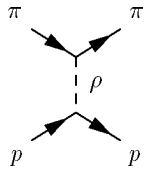

(2.2)

Such problems are avoided in the Regge theory. Here one exchanges one or more trajectories and instead of speaking about a particle that is exchanged one talks about a Reggeon exchange. The exchange of a Reggeon is equivalent to the exchange of many particles with different spins:

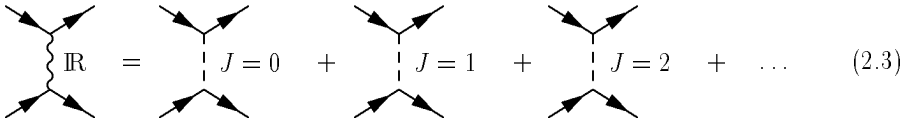

(2.3)

2.3 s and t channel

Before continuing with the development of the Regge theory, a short section to define two Lorentz invariant variables which are useful for further discussion. Let us denote by p_i the four–vector of particle i. The four momentum transfer squared t between A and C (or equivalently between B and D) is then defined as:

$$t = (p_C - p_A)^2 = (p_{\bar{A}} + p_C)^2 = (p_B - p_D)^2 = (p_B + p_{\bar{D}})^2 \tag{2.4}$$

Note that t can also be viewed as the center of mass squared of the crossed reaction $B + \bar{D} \to \bar{A} + C$. The center of mass squared s of the system $A + B$ $(= C + D)$ is given by:

$$s = (p_A + p_B)^2 = (p_B - p_{\bar{A}})^2 = (p_C + p_D)^2 = (p_C - p_{\bar{D}})^2 \tag{2.5}$$

Thus s can also be interpreted as the four momentum transfer squared from B to $\bar{A}$ of the process $B + \bar{D} \to \bar{A} + C$.

One can therefore look at a given two–body reaction either in the s–channel or in the t–channel, as described in the following diagram:

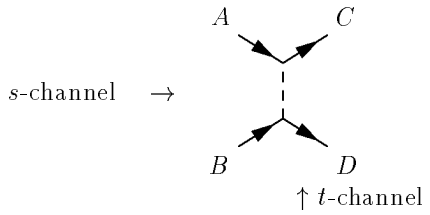

(2.6)

We can now resume the Regge theory discussion.

2.4 The Froissart bound

A fundamental reason why single particle exchange as described above cannot be the correct description of the two–particle hadronic processes at high energies is the following. Assume an elastic collision between spinless particles, all of mass m, exchanging a meson of mass M and spin J:

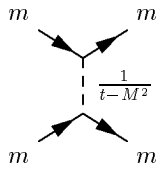

(2.7)

The transition amplitude can be written as:

$$T(s,t) \sim \frac{P_J(\cos\theta_t)}{t - M^2} \tag{2.8}$$

where P_J is the Legendre-function and θ_t the scattering angle in the center of mass system of the t–channel reaction $B + \bar{D} \to \bar{A} + C$. The angle can be expressed as:

$$\cos\theta_t = 1 + \frac{2s}{t - 4m^2} \tag{2.9}$$

At fixed t, as s grows, $\cos\theta_t \sim s$, and thus

$$T(s,t) \overset{s\to\infty}{\longrightarrow} s^J \tag{2.10}$$

For $J > 1$ this violates the Froissart [26] bound. What is the Froissart bound?

Froissart showed, that in the partial wave expansion of the scattering amplitude all partial waves with $l \geq l_{\max} = c\sqrt{s}\ln s$ (where c is some constant) are negligible. Summing the partial wave series and assuming maximum scattering in each partial wave he obtained:

$$\sigma \leq c \ln^2 s \quad \text{as} \quad s \to \infty. \tag{2.11}$$

The constant c is limited theoretically:

$$c \leq \frac{\pi}{m_\pi^2}. \tag{2.12}$$

Thus the cross section is bound by:

$$\sigma \leq \frac{\pi}{m_\pi^2} \ln^2 s \simeq (60\,\text{mb}) \ln^2 s. \tag{2.13}$$

This bound is known as the Froissart bound, also referred to sometimes as the Martin [27]–Froissart bound.

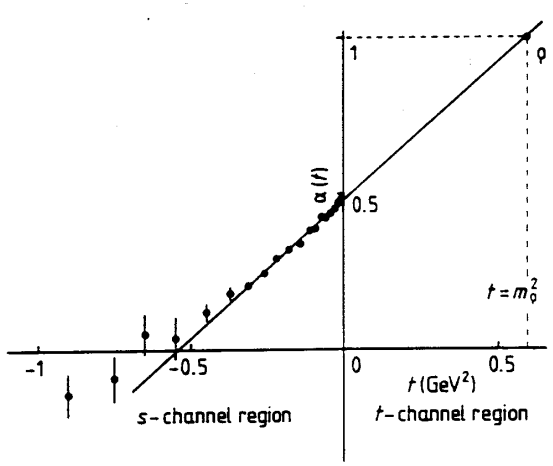

Figure 2.2: The ρ trajectory as determined from the charge exchange reaction $\pi^- p \to \pi^0 n$.

2.5 Regge trajectories

In this section we will describe the main steps leading to the Regge trajectory. Let us assume that there exists a bound state in the t–channel with angular momentum $l = L$ and mass $M_B < 2m$. The t–channel partial wave amplitude $f_L(t)$ has then a pole at $t = t_B \equiv M_B^2$. Similarly, if in the t–channel there is a resonance with mass M_R, width Γ and $l = L$, one gets a pole at a complex value $t = t_R \equiv M_R^2 - \mathrm{i}M_R\Gamma$.

The sequence $f_l(t), \quad l = 0, 1, 2, ...$ can be generalized to a function $f(l, t)$ which should be equal to $f_l(t)$ for $l = 0, 1, 2, ...$ This function is defined also for complex l. The sequence of poles for $l = L_1$ at $t = t_1$, $l = L_2$ at $t = t_2, \ldots$ is interpreted as a single moving Regge pole at $l = \alpha(t)$. The function $\alpha(t)$ is a trajectory function such that $\alpha(t_1) = L_1, \ldots$.

When $\alpha(t)$ is equal to an integer value L at $t = t_L$, this corresponds to a bound state or resonance with $l = L$ and mass and width given by $t_l = M_L^2 - iM_L\Gamma$. The trajectory which gives a resonance with $l = L$ and complex t_L will also cause a pole at the real value $t = M_L^2$ when l has the complex value $L + \mathrm{Im}\,\alpha(t)$. Therefore the real values t_l where $\mathrm{Re}\,\alpha(t_l) = L$ give the masses $M_L^2 = t_l$ of the particles with spin L. This can be demonstrated in figure 2.2 where the ρ trajectory is determined from the charge exchange reaction $\pi^- p \to \pi^0 n$. When the trajectory gets to the mass of the ρ its value is equal to the spin of the ρ: $\alpha(M_\rho^2) = 1$. In the Chew–Frautschi plot shown earlier in figure 2.1 one sees more examples of trajectories having the same feature.

Originally, Regge was interested in the behaviour of the t–channel scattering amplitude in the unphysical limit $\cos\theta_t \to -\infty$. The usual partial-wave series diverges when $|\cos\theta_t| = 1+\epsilon$. So he used the function $f(l, t)$ to convert the sum into a contour integral in the complex

l plane, which allowed $\cos\theta_t \to -\infty$. He obtained

$$T_t(t, s) \sim (\cos\theta_t)^{\alpha(t)} \tag{2.14}$$

where $\alpha(t)$ is the trajectory whose real part is largest for the given t.

It was Mandelstam who realised that the limit $\cos\theta_t \to -\infty$ in the t–channel reaction $B + \bar{D} \to \bar{A} + C$ corresponds to $s \to \infty$ in the s–channel reaction $A + B \to C + D$ (see Eqn. 2.9 with fixed (negative) t).

Since the transition amplitude fulfils $T_s(s, t) = T_t(t, s)$ one gets at fixed t:

$$T_s(s, t) \sim s^{\alpha(t)} \tag{2.15}$$

More precisely, at fixed t:

$$T_s(s, t) \overset{s\to\infty}{\longrightarrow} \gamma(t) \left(\frac{s}{s_0}\right)^{\alpha(t)} \tag{2.16}$$

where s_0 is a scale factor. The function $\gamma(t)$ is closely related to the residue of $f(l, t)$ at the pole $l = \alpha(t)$.

In the relativistic case one needs to consider the signature (+ for even J, - for odd J) and one gets:

$$T_s(s, t) = \gamma_\pm(t) \frac{1 \pm \mathrm{e}^{-\mathrm{i}\pi\alpha(t)}}{\sin\pi\alpha(t)} \left(\frac{s}{s_0}\right)^{\alpha(t)}. \tag{2.17}$$

The functions $\gamma_\pm(t)$ factorize. This means that for $A + B \to C + D$ one can write:

$$\gamma(t) = \gamma_{\mathrm{AC}}(t)\gamma_{\mathrm{BD}}(t). \tag{2.18}$$

If several sets of t–channel internal quantum numbers are possible, one includes a contribution from the leading trajectory of each type.

2.6 Shrinkage

Before the Regge theory was fully developed, one had a simple phenomenological description of a large number of two–body reactions. The energy behaviour of the forward differential cross section of these reactions could be described by the form:

$$\frac{\mathrm{d}\sigma}{\mathrm{d}t}(s, t = 0) = \frac{A}{s^2} \left(\frac{s}{s_0}\right)^{2\alpha_{\mathrm{eff}}} \tag{2.19}$$

The values of α_{eff} obtained from fitting the data are given in table 2.1. Regge theory identifies α_{eff} with $\alpha(t = 0)$ of the dominant Regge trajectory contributing to the reaction. The value $\alpha(t = 0)$, also denoted sometimes by α_0, is called the intercept of the Regge trajectory.

Table 2.1: Coefficients α_{eff} and the possible exchanged–particles for various processes.

Reaction	t-channel	$\approx \alpha_{\text{eff}}$
$\pi^- p \to \pi^0 n$	ρ	0.5
$K^- p \to \bar{K}^0 n$	ρ, a_2	0.5
$\gamma p \to \pi^0 p$	ρ, ω	0.5
$\pi^- p \to K^0 \Lambda$	K^*, K_2^*	0.2
$K^- p \to \pi^0 \Lambda$	K^*, K_2^*	0.2
$\pi^- p \to p\pi^-$	Δ	0
$\pi^+ p \to p\pi^+$	N, Δ	0

The Chew–Frautschi plot shows that the trajectories are linear in t and can be expressed in a simple form:

$$\alpha(t) = \alpha_0 + \alpha' t \tag{2.20}$$

The slope of the trajectory, α' is positive and has the value $\alpha' \approx 1\,\text{GeV}^{-2}$ for most trajectories.

If one pole dominates one can write the differential cross section in the form:

$$\frac{\mathrm{d}\sigma}{\mathrm{d}t} = \frac{\gamma(t)}{s^2}\left(\frac{s}{s_0}\right)^{2\alpha(t)} = \frac{\gamma(t)}{s^2}\left(\frac{s}{s_0}\right)^{2\alpha_0 + 2\alpha' t} \tag{2.21}$$

$$= \frac{\gamma(t)}{s_0^2}\left(\frac{s}{s_0}\right)^{2(\alpha_0 - 1)} \mathrm{e}^{2\alpha' t \ln\left(\frac{s}{s_0}\right)} \tag{2.22}$$

This expression gives both the s and the t dependence of the cross section. Since $t < 0$, the exponential cutoff in t becomes sharper as s increases. In other words, the higher the energy, the larger the exponential coefficient of the differential cross section, where the growth of the steepness is determined by α'. This phenomena is called shrinkage and one says that $\frac{\mathrm{d}\sigma}{\mathrm{d}t}$ shrinks as s grows. An example [28] of the shrinkage phenomena is shown in figure 2.3 for the elastic pp reactions. We will return to the shrinkage phenomena in the last chapter.

2.7 The Pomeron

From the form of equation 2.19 one can see that the forward scattering amplitude of the elastic scattering has an energy dependence given by:

$$\frac{\mathrm{d}\sigma}{\mathrm{d}t}(s, t = 0) \sim \left(\frac{s}{s_0}\right)^{2(\alpha_0 - 1)} . \tag{2.23}$$

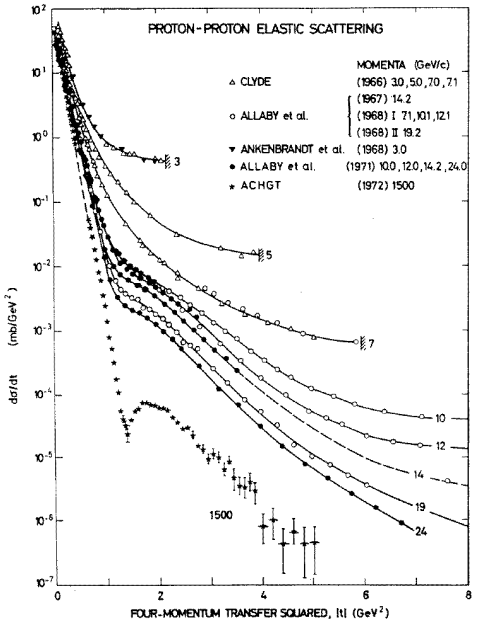

Figure 2.3: $\frac{\mathrm{d}\sigma}{\mathrm{d}t}$ for different s for pp reactions.

The total cross section is related to the imaginary part of the forward elastic scattering amplitude by the optical theorem. Therefore one can write:

$$\sigma_{\text{tot}} \sim \left(\frac{s}{s_0}\right)^{\alpha_0 - 1} . \tag{2.24}$$

Since all the known trajectories of existing particles have $\alpha_0 < 1$, the conclusion from equation 2.24 is that σ_{tot} should decrease with energy. Experimentally, however, σ_{tot} seemed to approach a constant value as s increased. This is shown in figure 2.4 where the total cross section for various particles on proton target is plotted as function of the incoming beam momentum [28]. Note that this figure already includes later data which showed that at high energies the total cross section starts to increase. This was not yet known at that time and the belief was that it reaches a constant energy–independent value.

In order to keep the Regge picture consistent with the experimental data, one needed to assume the existence of a trajectory with an intercept $\alpha_0 \simeq 1$. Though this idea was originally suggested by Gribov, the trajectory was named by Gell–Mann after Pomeranchuk, who derived in 1958 his theory [29] about the asymptotic behaviour of the differences of cross sections. The trajectory was first called the Pomeranchukon trajectory, and was later

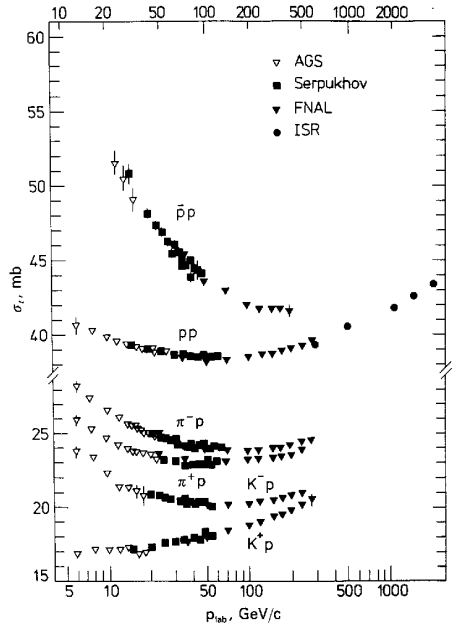

Figure 2.4: Total cross section measurements for various reactions.

abbreviated to the Pomeron. This trajectory ($\mathbb{P}$) was assumed to have the form:

$$\alpha_{\mathbb{P}}(t) = \alpha_{\mathbb{P}}(0) + \alpha'_{\mathbb{P}} t \tag{2.25}$$

with an intercept of $\alpha_{\mathbb{P}}(0) \simeq 1$ and a slope [30] of $\alpha'_{\mathbb{P}} \simeq 0.25\,\mathrm{GeV}^{-2}$. These values are different from all those of the known trajectories, some of which are given in table 2.1. So far no particle was found which corresponds to the Pomeron trajectory.

2.7.1 The Pomeranchuk Theorem

Since we mentioned earlier the Pomeranchuk theorem, lets say a few words about it. Pomeranchuk studied [29] the high energ behaviour of the differences between the total cross sections, $\Delta\sigma$, defined as:

$$\Delta\sigma \equiv \sigma(\bar{A}B) - \sigma(AB) \tag{2.26}$$

for any particles A, $\bar{A}$ and B. The scattering should become purely 'diffractive' (in the optical sense) at high energies. The elastic scattering should be just the shadow of the inelastic reactions. In this picture, via the optical theorem, one expects the amplitudes to

be almost purely imaginary. Under the assumption that

$$\frac{\mathrm{Re}\,T(s,0)}{\mathrm{Im}\,T(s,0)} \xrightarrow{s\to\infty} 0 \tag{2.27}$$

and if $\sigma(\bar{A}B) \to C_1$ and $\sigma(AB) \to C_2$, Pomeranchuk proved that $C_1 = C_2$. This led to his theorem that at high energies the differences between particle and antiparticle cross sections should vanish:

$$\Delta\sigma \to 0 \tag{2.28}$$

This is known as the Pomeranchuk theorem. The experimental data seem to support this prediction, as can be seen from figure 2.5.

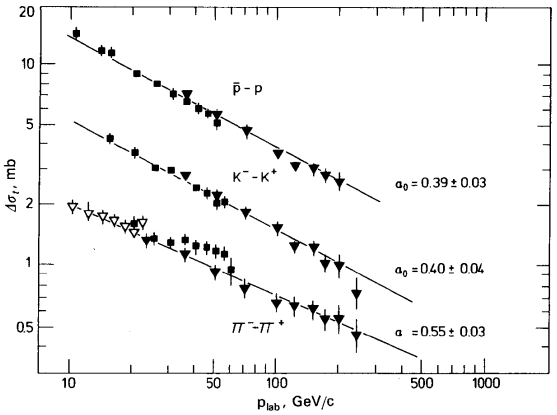

Figure 2.5: Total cross section differences for various reactions

2.8 High energy behaviour of σ_{tot}

As we mentioned above, the total cross section actually starts rising with energy. What changes does one have to make to the Pomeron trajectory parameters? Clearly, in order to describe the rise, the intercept has to be bigger than 1. By how much? One way to find out is to fit the total cross section data to the form given in equation 2.24. However, we know that there are also other trajectories which can be exchanged in addition to the Pomeron.

Donnachie and Landshoff (DL) [31] attempted a global fit to all existing σ_{tot} data. They realized that all the Reggeon intercepts can be represented by one effective intercept having

a value of $\alpha_{\mathbb{R}}(0) \sim 0.55$. Also, the elastic scattering data can be described by having two exchanges, a Reggeon and a Pomeron.

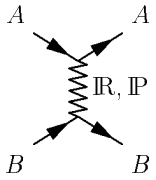

(2.29)

When a Reggeon is being exchanged, one usually exchanges quantum numbers, while in the case of the Pomeron exchange there is the exchange of vacuum quantum numbers. Using the optical theorem, one expects also the total cross section to be described by the sum of these two exchanges. Thus motivated, DL fitted the total cross section data to a sum of two terms:

$$\sigma_{\text{tot}} = Xs^{\alpha_{\mathbb{P}}(0)-1} + Ys^{\alpha_{\mathbb{R}}(0)-1} \tag{2.30}$$

In order to get the rising cross section at high energies they parametrized the Pomeron intercept as $\alpha_{\mathbb{P}}(0) = 1 + \epsilon$. The value of the Reggeon intercept was fixed to 0.55 (actually 0.5475). In addition, DL used the Pomeranchuk theorem for the first term which describes the Pomeron exchange. Since at high energies only the Pomeron term remains, they constrained the coefficients X to be the same for particle and for antiparticles. For example, they require $X(\pi^+) = X(\pi^-)$. The combined fit can be seen in figure 2.6 and gives a good description of the data. The resulting value for the Pomeron parameter was $\epsilon \simeq 0.08$ (actually 0.0808). The rising power of the total cross section is small enough and violates the Froissart bound only at energies of about 10^3 TeV.

2.8.1 $\sigma_{\text{tot}}(\gamma p)$ at HERA energies

By using the results of their fit and Vector Dominance Model (VDM) [32] arguments, DL [31] predicted the behaviour of the total photoproduction cross section:

$$\sigma_{\text{tot}}(\gamma p) = 0.0677 s^{0.0808} + 0.129 s^{-0.4525} \tag{2.31}$$

where the units are such that the cross section is in mb. All existing data above $\sqrt{s} = 6\,\text{GeV}$ up to the highest center of mass energy for which data existed on $\sigma_{\text{tot}}(\gamma p)$, about 20 GeV, were well described by the predictions of DL. It was very interesting whether the prediction would hold also for higher energies and thus the first measurements of HERA were eagerly awaited. This was in particular the case since in addition to DL and other [18] Regge motivated predictions, there were so–called 'mini-jet' models [33] which predicted that the total photoproduction cross section at HERA energies ($\sqrt{s} \sim 200\,\text{GeV}$) could be as large as about 1 mb, compared to about 0.15 mb as predicted by the Regge based models.

What does photoproduction have to do with HERA? As already mentioned in the earlier chapter, the exchanged particle at the lepton vertex in NC events is a virtual photon,

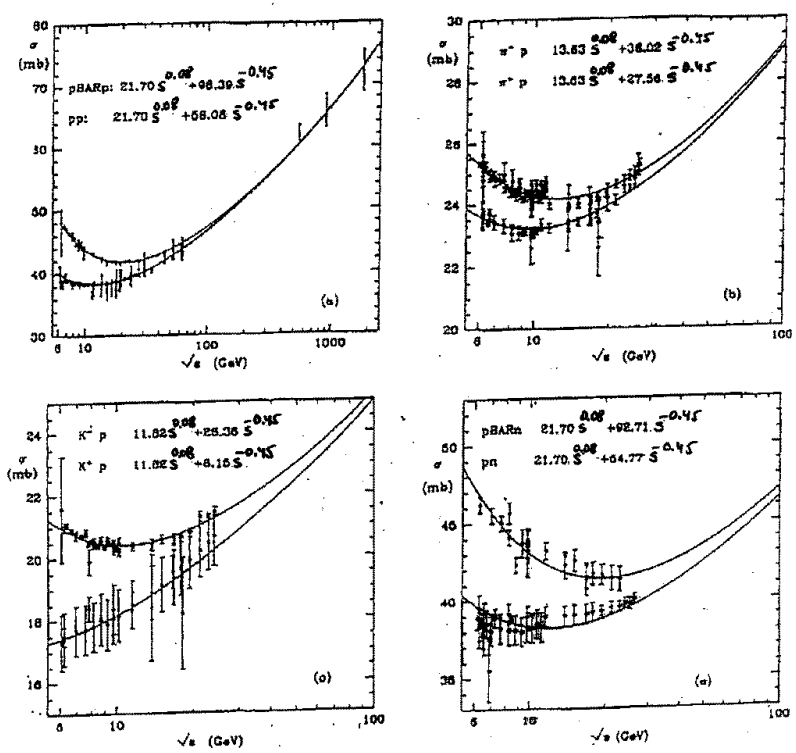

Figure 2.6: Fits of a simple Regge form containing two terms to total cross section measurements of pp, $\bar{p}p$, $\pi^{\pm}p$, $K^{\pm}p$, pn and $\bar{p}n$ reactions.

provided the Q^2 is not very large. As we will show in the next chapter, Q^2 is a function of the energies of the incoming (E) and outgoing (E') electrons and the scattering angle θ of the outgoing electron with respect to the incoming proton direction. The exact relation is:

$$Q^2 = 2EE'(1 + \cos\theta) \tag{2.32}$$

One sees that when the outgoing electron continues close to the incoming electron's direction ($\theta \approx \pi$), $Q^2 \approx 0$ and can be considered as the exchange of an almost–real photon. The two experiments, H1 and ZEUS, have each [34, 35, 36, 37] a small calorimeter at a distance of about 30 m from the interaction point which allows to detect electrons which are scattered by less than 5 mrad with respect to the incoming electron direction. This ensures that the virtuality of the photons is in the range $10^{-8} < Q^2 < 0.02\,\text{GeV}^2$, with the median $Q^2 \sim 10^{-5}\,\text{GeV}^2$. A diagramatic example of a photoproduction event is shown

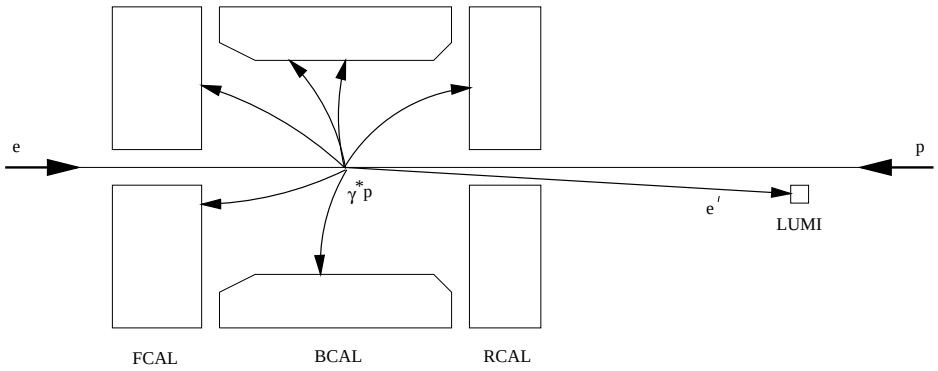

Figure 2.7: A diagramatic example of a photoproduction event in the ZEUS detector, where the scattered electron is detected in the small angle electron calorimeter LUMIE.

in figure 2.7. Since the cross section for photoproduction reactions is large compared to that of DIS events, even a low luminosity run can be sufficient for determining $\sigma_{\rm tot}(\gamma p)$. Thus this was the first measurement [38, 39] done when the HERA collider was turned on in summer of 1992. Using the photoproduction events taken during a net running time of 7 minutes, the first measurement of $\sigma_{\rm tot}(\gamma p)$ was obtained at $\sqrt{s} = 200\,\mathrm{GeV}$ (figure 2.8). Although the measurement had a large uncertainty, it was enough to establish that there is no dramatic rise of the cross section between 20 and 200 GeV, thus excluding some of the predictions. Clearly the Regge based predictions, labelled DL [31] and ALLM [18], were consistent with the data.

2.9 Summary

In this chapter the following subjects have been covered:

- We have shown that the simple single particle exchange picture is in variance with the Froissart bound.
- The Regge trajectory has been introduced and some of the properties have been reviewed for the trajectories which have corresponding particles. All known trajectories seem to be linear and can be expressed as $\alpha(t) = \alpha_0 + \alpha' t$, with an intercept not bigger than 0.5 and a slope of about $1\,\mathrm{GeV}^{-2}$.
- The shrinkage phenomena has been introduced for further discussion in the chapter on diffraction. As long as the slope of the Regge trajectory is non–zero, one expects to have a steeper fall of the differential cross section as one goes to higher energies.

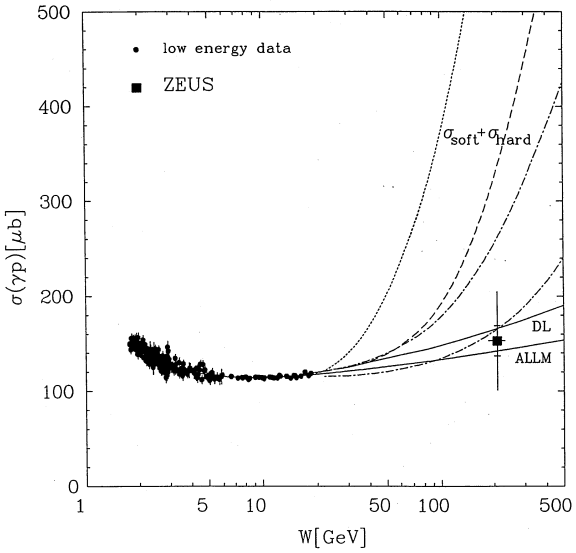

Figure 2.8: The HERA first measurement of $\sigma_{\rm tot}(\gamma p)$, together with lower energy data. The curves are predictions of different models for the HERA energy range region.

- The Pomeron trajectory was introduced in order to explain the behaviour of the total cross section at higher energies. This trajectory has so far no corresponding particle. It has an intercept which is somewhat bigger than 1 and a slope of about $0.25\,\mathrm{GeV}^{-2}$.
- The Pomeranchuk theorem was mentioned. It predicts that the differences between the total cross section of particles and antiparticles should approach zero at high energies.
- We introduced the two–term expression of Donnachie and Landshoff which is based on the Regge approach and can explain all the data on total cross sections. By using a fixed effective intercept of about 0.55 for the Reggeon trajectory, and by using the Pomeranchukon theorem for the Pomeron term, DL obtained an intercept of 1.08 for the Pomeron by performing a joint fit to all the data existing in 1992.

- After explaining how the total γp cross section can be measured at HERA, we showed that the measurement of $\sigma_{\rm tot}(\gamma p)$ at HERA shows a mild increase, like other hadronic cross sections and thus consistent with the predictions of Regge based models and excluding those which predicted a dramatic rise.

Chapter 3

Deep Inelastic Scattering at HERA

In this chapter we will first discuss the kinematical variables used in DIS, describing first the fixed target configuration and then that of the colliding beams at HERA. The second section will be devoted to defining the inelastic structure function and its relation to the total $\gamma^* p$ absorption cross section. The ratio of the longitudinal to transverse part of that cross section, R will also be discussed. In the third section we will mention shortly the important issue of radiative corrections and the chapter will finish with a section describing the experimental determination of the structure function.

3.1 Kinematics

We shall start with the most general case of a deep inelastic scattering of a lepton with mass m_l and four vector $k(E_l, \vec{k})$ on a proton with mass m_p and four vector $p(E_p, \vec{p})$, as depicted in figure 3.1. The outgoing lepton has a mass of m_l' with four vector $k'(E_l', \vec{k'})$ and the scattered hadrons emerge with a mass m_h and four vector $p_h(E_h, \vec{p_h})$. The exchanged particle can be a gauge boson γ, Z^0 or $W^{\pm}$, depending on the circumstances. The four vector of the exchanged boson is $q(q_0, \vec{q})$.

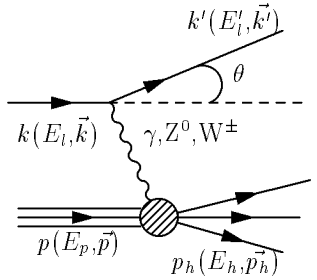

Figure 3.1: Deep inelastic lepton–proton–scattering.

With these notations one can define the following variables:

$$q = k - k' = p_h - p \tag{3.1}$$

$$\nu \equiv \frac{p \cdot q}{m_p} \tag{3.2}$$

$$y \equiv \frac{p \cdot q}{p \cdot k} \tag{3.3}$$

$$W^2 = (p+q)^2 \tag{3.4}$$

$$s = (k+p)^2 \tag{3.5}$$

The meaning of the variables ν and y is most easily realized in the rest frame of the proton (see fixed target subsection). The variable W^2 is the center of mass squared of the gauge–boson proton system, and thus also the invariant mass squared of the hadronic final state. The variable s is the center of mass squared of the lepton proton system.

The four momentum transfer squared at the lepton vertex can be approximated as follows (for $m_l, m_l' \ll E, E'$):

$$q^2 = (k-k')^2 = m_l^2 + m_l'^2 - 2kk' \approx -2EE'(1-\cos\theta) < 0 \tag{3.6}$$

Note that in this expression the scattering angle θ is defined with respect to the incoming lepton direction. The variable which is mostly used in DIS is the negative value of the four momentum transfer squared at the lepton vertex:

$$Q^2 \equiv -q^2 \tag{3.7}$$

One is now ready to define the other variable most frequent in DIS, namely the dimensionless scaling variable x:

$$x \equiv \frac{Q^2}{2p \cdot q} \tag{3.8}$$

3.1.1 The physical meaning of the Bjorken–x variable

In order to understand the physical meaning of the scaling variable x, defined by Bjorken, let us consider the diagram presented in figure 3.2.

An exchanged boson with four momentum q interacts with a parton having a fraction z of the incoming proton four momentum, producing a parton with four momentum p'. Using the definitions in the previous section one can obtain the following:

$$(zp+q)^2 = p'^2 \tag{3.9}$$

$$z^2 p^2 - Q^2 + 2zp \cdot q = m_{p'}^2 \tag{3.10}$$

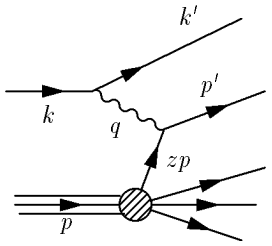

Figure 3.2: Explanation of the Bjorken x variable

which finally leads to:

$$z = \frac{Q^2 + m_{p'}^2 - z^2 p^2}{2p \cdot q} = x\left(1 + \frac{m_{p'}^2 - z^2 m_p^2}{2p \cdot q}\right) \tag{3.11}$$

If one can assume that the partons have zero mass, which is a good assumption in the infinite momentum frame, then one gets:

$$x = z \tag{3.12}$$

This means that x is the fraction of the proton momentum taken by the parton which is hit by the exchanged boson in the DIS interaction.

3.1.2 Fixed target kinematics ($\vec{p} = 0$)

Before HERA started to operate, all DIS experiments [40, 41, 14] were on fixed targets ($\vec{p} = 0$). For this case, some of the variables defined earlier have a simple physical interpretation. The variable ν:

$$\nu \equiv \frac{p \cdot q}{m_p} = \frac{p \cdot (k - k')}{m_p} = \frac{m_p(E - E')}{m_p} = (E - E') = q_0 \tag{3.13}$$

Thus, for fixed target experiments, ν is the energy of the exchanged boson. Another expression for ν is:

$$\nu = \frac{p \cdot (p_h - p)}{m_p} = \frac{m_p(E_h - m_p)}{m_p} = E_h - m_p \tag{3.14}$$

which is the energy transfer at the hadronic vertex.

The second scaling variable defined by Bjorken is y. It has the following meaning in the case of a fixed target:

$$y \equiv \frac{p \cdot q}{p \cdot k} = \frac{m_p \nu}{p \cdot k} = \frac{\nu}{E} \tag{3.15}$$

which is the fraction of the incoming lepton energy carried by the exchanged boson, also called inelasticity. It can be calculated either at the lepton vertex or at the hadron vertex:

$$y = \begin{cases} \frac{E - E'}{E} & \text{leptons} \\ \frac{E_h - m_p}{E} & \text{hadrons} \end{cases} \tag{3.16}$$

Clearly one sees that the value of y is limited to:

$$0 \leq y \leq 1 \tag{3.17}$$

What are the limits on the value of the Bjorken–x? The Bjorken variable x can be written as

$$x \equiv \frac{Q^2}{2p \cdot q} = \frac{Q^2}{2m_p \nu} \tag{3.18}$$

On the other hand we can express W^2 as follows:

$$W^2 = (p + q)^2 = p^2 - Q^2 + 2p \cdot q = m_p^2 - 2p \cdot qx + 2p \cdot q = m_p^2 + 2p \cdot q(1 - x) \tag{3.19}$$

Since the invariant mass squared of the hadronic system has to be equal or bigger than the proton mass squared, $W^2 \geq m_p^2$, one gets:

$$0 \leq x \leq 1 \tag{3.20}$$

which is consistent with the physical interpretation of x being the fraction of the proton's momentum carried by the struck parton.

The following relations are useful if one wants to calculate the kinematic limits which one can achieve on Q^2 and x in the fixed target experiments.

$$s = (p + k)^2 = p^2 + k^2 + 2p \cdot k = m_p^2 + \frac{2p \cdot q}{y} = m_p^2 + \frac{Q^2}{xy} \tag{3.21}$$

which leads to:

$$Q^2 = (s - m^2)xy \tag{3.22}$$

Thus the maximum value of Q^2, given a lepton beam of energy E, is:

$$Q_{max}^2 = s - m_p^2 \approx 2m_p E \tag{3.23}$$

and the minimum value obtainable for x is:

$$x_{min} = \frac{Q^2}{s - m_p^2} = \frac{Q^2}{2m_p E} \tag{3.24}$$

The fixed target experiments used typically muon beams with energies of a few hundred GeV. Thus, for example, for $E = 200\,\text{GeV}$, and $Q^2 = 4\,\text{GeV}^2$, the minimum value of x is $x_{min} \approx 10^{-2}$.

3.1.3 HERA kinematics

At HERA, an electron (we will use electron to mean both electron or positron) beam of energy E collides with a proton beam of energy E_p. At present $E = 27.5\,\mathrm{GeV}$ and $E_p = 820\,\mathrm{GeV}$. The $+z$ axis is chosen in the proton beam direction and the scattering angle of the outgoing electron is measured with respect to the proton beam. The four vectors of the incoming electron (k), outgoing electron (k'), incoming proton (p) and outgoing hadrons (p_h) are defined as follows:

$$k = \begin{pmatrix} E \\ 0 \\ 0 \\ -E \end{pmatrix} \qquad k' = \begin{pmatrix} E' \\ E'\sin\theta \\ 0 \\ E'\cos\theta \end{pmatrix} \qquad p = \begin{pmatrix} E_p \\ 0 \\ 0 \\ E_p \end{pmatrix} \qquad p_h = \begin{pmatrix} E_h \\ p_{xh} \\ p_{yh} \\ p_{zh} \end{pmatrix} \tag{3.25}$$

Since the detectors at HERA have an almost complete 4π coverage, one can determine the x and Q^2 DIS variables by more than one method [42]. One can use the outgoing electron, the outgoing hadrons or a combination of both. This allows therefore a consistency check on the determination by comparing the results from the different methods. Each method has its kinematical range in which it can determine the variables with a better precision than the others. In the following we will discuss the three different methods.

Electron variables

In this case, as used to be done in the fixed target experiments, only the four vector of the scattered electron is used:

$$Q^2 = -(k - k')^2 = 2EE'(1 + \cos\theta) \tag{3.26}$$

$$\begin{aligned} y \;\equiv\; \frac{p\cdot q}{p\cdot k} &= 1 - \frac{pk'}{pk} = 1 - \frac{pk'}{2EE_p} \\ &= 1 - \frac{E_pE' - E_pE'\cos\theta}{2EE_p} = 1 - \frac{E'}{2E}(1 - \cos\theta) \end{aligned} \tag{3.27}$$

Using Q^2 and y one can get x:

$$x = \frac{Q^2}{4EE_p y} \tag{3.28}$$

Some further useful relations in this case can be obtained in the following way:

$$\begin{aligned} \frac{Q^2}{2EE'} &= 1 + \cos\theta \\ \frac{2E(1-y)}{E'} &= 1 - \cos\theta \\ \frac{Q^2 2E(1-y)}{2EE'^2} &= \sin^2\theta \end{aligned} \tag{3.29}$$

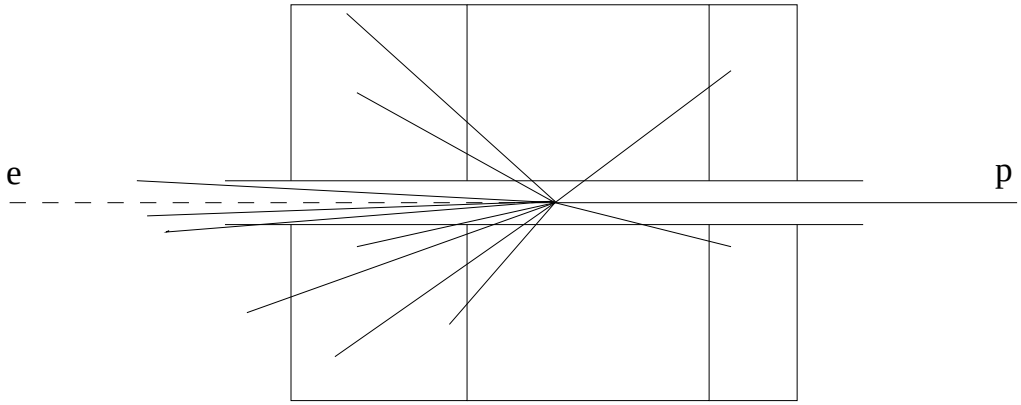

Figure 3.3: A sketch for understanding the Jacquet–Blondel method.

Therefore one gets:

$$Q^2 = \frac{E'^2\sin^2\theta}{1-y} = \frac{p_{Te}^2}{1-y} \tag{3.30}$$

Since in the NC case the p_T of the electron balances that of the hadronic final state, the last relation means also that $Q^2 = p_{Th}^2/(1-y)$, a relation to be used in the description of the hadronic method.

Hadronic variables

One can clearly determine the y, Q^2 and x variables if one measures all the outgoing hadrons. However, some of the hadrons escape through the uncovered region in the beam pipe, as shown in the sketch in figure 3.3. Nevertheless, as was shown by Jacquet and Blondel [43], one can still determine to a good approximation the above variables.

The variable y can be calculated in the following way:

$$y = \frac{p\cdot(p_h - p)}{p\cdot k} = \frac{p\cdot p_h}{2EE_p} = \frac{E_pE_h - E_pp_{zh}}{2EE_p} = \frac{E_h - p_{zh}}{2E} \tag{3.31}$$

Since most of the missing hadrons which do not make it into the detector have a small p_T, their contribution to $E_h - p_{zh}$ is negligible and thus one gets a good estimate of y using this formula. When determined this way, it is usually denoted y_{JB}, namely y Jacquet–Blondel.

The other two variables can be now calculated in the following way:

$$Q^2 = \frac{p_{xh}^2 + p_{yh}^2}{1 - y_{JB}} \tag{3.32}$$

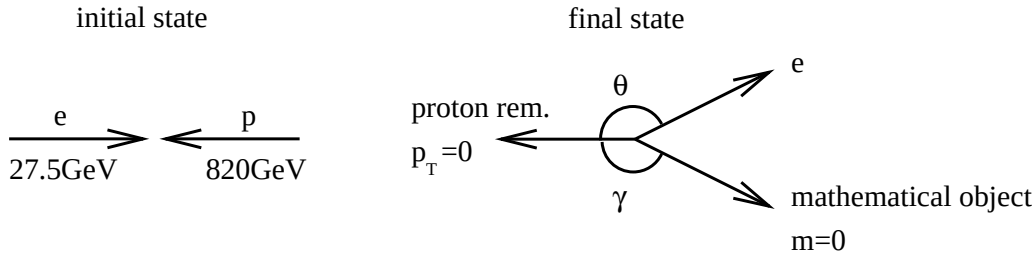

Figure 3.4: The two angles used in the double angle method.

and

$$x = \frac{Q^2}{4EE_p y_{JB}} \tag{3.33}$$

The double angle method

When using a method based on a mixture of the electron and the hadron variables, one can choose different combinations. The one described here is called the double angle (DA) method and uses measurements of two angles. One is the scattering angle θ of the outgoing electron (see figure 3.4). The other angle is that of an object which has a simple meaning in the naive parton model: assuming that the struck parton is massless, it would scatter by an angle γ. In this interpretation the p_T of the proton remnant is zero. Note that these assumption are necessary only for the physical interpretation of the angle γ. The calculation is however exact.

Defining the four vector of the scattered electron k' and that of the mathematical massless object Γ as follows:

$$k' = \begin{pmatrix} E' \\ E'\sin\theta \\ 0 \\ E'\cos\theta \end{pmatrix} \qquad \Gamma = \begin{pmatrix} \Gamma \\ \Gamma\sin\gamma \\ 0 \\ \Gamma\cos\gamma \end{pmatrix} \tag{3.34}$$

one gets from the scattered electron measurements:

$$Q^2 = \frac{E'\sin^2\theta}{1-y} \tag{3.35}$$

and

$$y = 1 - \frac{E'}{2E}(1-\cos\theta) \tag{3.36}$$

Using the measurements coming from the hadrons one obtains:

$$Q^2 = \frac{p_{Th}^2}{1-y} = \frac{\Gamma^2\sin^2\gamma}{1-y} \tag{3.37}$$

and

$$y = \frac{E_h - p_{zH}}{2E} = \frac{\Gamma(1-\cos\gamma)}{2E} \tag{3.38}$$

which leads to the calculation of the angle γ:

$$\cos\gamma = \frac{p_{Th}^2 - (E_h - p_{zh})^2}{p_{Th}^2 + (E_h - p_{zh})^2} \tag{3.39}$$

We are now ready to define Q^2 and x using only the two angles (in addition to the given incoming energies of the beams). The variables calculated this way usually have the subscript DA to denote that they were obtained through the double angle method:

$$Q^2_{\rm DA} = 4E^2\left[\frac{\sin\gamma(1+\cos\theta)}{\sin\gamma+\sin\theta-\sin(\theta+\gamma)}\right] \tag{3.40}$$

and

$$x_{\rm DA} = \left(\frac{E}{E_p}\right)\left[\frac{\sin\gamma+\sin\theta+\sin(\theta+\gamma)}{\sin\gamma+\sin\theta-\sin(\theta+\gamma)}\right] \tag{3.41}$$

The advantage of the DA method is that one is less sensitive to a scale uncertainty in the energy measurement of the final state particles since the angle γ is obtained by ratios of energies.

Kinematical limits at HERA

What are the kinematical limits on x and Q^2 that one can reach at HERA? Since $s = 9\times 10^4\,\mathrm{GeV}^2$, this is also the value of Q^2_{max}. With the present luminosities, the two experiments have enough data for measurements up to about $10^4\,\mathrm{GeV}^2$, as shown in figure 1.1 of the first chapter. Amazingly enough, the HERA experiments made big efforts to obtain data at very low Q^2, down to about $0.2\,\mathrm{GeV}^2$, for reasons to be mentioned later. Thus they also reached very low x values, close to 10^{-6}.

One of the aims of these measurements is to obtain the structure function of the proton, which is the subject of the next section.

3.2 Inelastic structure function

In analogy to the Rosenbluth formula [44] in the elastic case the deep inelastic cross–section can be written as [45]:

$$\frac{\mathrm{d}^2\sigma}{\mathrm{d}\Omega dE'} = \frac{4\alpha^2E'^2}{Q^4}\left[2W_1\sin^2\frac{\theta}{2} + W_2\cos^2\frac{\theta}{2}\right] \tag{3.42}$$

where $W_{1,2}(\nu, Q^2)$ are two structure functions which can be related to the absorption cross section of the virtual photon γ^*. In order to see the relation, note that the DIS cross section is obtained from a product of two tensors, a leptonic one and a hadronic tensor. The hadronic tensor $W_{\alpha\beta}$ can be related through the optical theorem to the $\gamma^* p$ cross section, as shown in the following diagram:

$$W_{\alpha\beta} \quad \propto \quad \sum_x$$

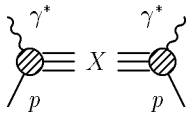

(3.43)

The cross section for a real photon is defined as

$$\sigma_\lambda^{\rm tot}(\gamma p \to {\rm X}) = \frac{4\pi^2\alpha}{K}\epsilon_\lambda^{\alpha^*}\epsilon_\lambda^{\beta}W_{\alpha\beta} \tag{3.44}$$

where K is the flux factor, ϵ_λ is the polarisation vector and λ is the helicity of the photon. The flux of real photons is $K = \nu$ and the allowed helicities are $\lambda = \pm 1$.

In order to extend the discussion to virtual photons, we need to know the polarization vectors and the flux of a virtual photon beam. To this end we will use the expressions of the polarization vectors derived for a massive vector meson:

$$\epsilon_{\pm 1}^{\alpha} = \pm\frac{1}{\sqrt{2}}(0; 1, \pm i, 0) \tag{3.45}$$

$$\epsilon_0^{\alpha} = \pm\frac{1}{\sqrt{Q^2}}(\sqrt{\nu^2 + Q^2}; 0, 0, \nu) \tag{3.46}$$

From parity conservation one can write (for the case where the incoming lepton is e or μ and the target proton is unpolarized) $\sigma_{+1} = \sigma_{-1}$. The two independent cross sections are defined as:

$$\sigma_T = \frac{1}{2}(\sigma_{+1} + \sigma_{-1}) \qquad \sigma_L = \sigma_0 \tag{3.47}$$

where σ_T and σ_L are the transverse and longitudinal $\gamma^* p$ cross section.

3.2.1 Flux of virtual photons

The definition of the flux is a matter of convention, but the principle is that in the limit of approaching the real photon case ($Q^2 \to 0$), the flux K should be equal that of a real photon beam ($K \to \nu$). We shall mention two flux conventions, that of Gilman [46] and that of Hand [47]. Gilman adds the Q^2 of the virtual photon to the flux definition:

$$K^{\rm Gil} = \sqrt{\nu^2 + Q^2} \tag{3.48}$$

Hand defines the flux K as that energy which a real photon would need in order to create the same final state. Thus $K^{\rm Hand}$ can be calculated using the following argument. The invariant mass squared of the hadronic final state for a $\gamma^* p$ interaction is given by:

$$W^2 = (p+q)^2 = m_p^2 + 2m_p\nu - Q^2 \tag{3.49}$$

The same quantity for a real photon of energy $K^{\rm Hand}$ is given by:

$$W^2 = m_p^2 + 2m_p K^{\rm Hand} \tag{3.50}$$

Therefore

$$K^{\rm Hand} = \nu - \frac{Q^2}{2m_p} \tag{3.51}$$

Clearly both definitions fulfil the requirement that when $Q^2 \to 0$ then $K \to \nu$.

The two structure functions $W_{1,2}(\nu, Q^2)$ are related to the total $\gamma^* p$ transverse and longitudinal absorption cross sections in the following way:

$$W_1(\nu, Q^2) = \frac{K}{4\pi^2\alpha}\sigma_T^{\gamma^* p} \tag{3.52}$$

$$W_2(\nu, Q^2) = \frac{K}{4\pi^2\alpha}\frac{Q^2}{Q^2+\nu^2}(\sigma_T^{\gamma^* p} + \sigma_L^{\gamma^* p}) \tag{3.53}$$

3.2.2 The ratio $R = \sigma_L/\sigma_T$

The ratio of the longitudinal to transverse $\gamma^* p$ cross section carries information about the spin of the quarks in the quark–parton model. In order to see that we can use equation 3.53 to write:

$$R \equiv \frac{\sigma_L}{\sigma_T} = \frac{W_2}{W_1}(1 + \frac{\nu^2}{Q^2}) - 1 \tag{3.54}$$

One can use QED to calculate the exact expressions for the two structure functions W_1 and W_2 for the case of the scattering of two point–like spin–1/2 fermions $e\mu \to e\mu$:

$$W_2^{e\mu} = \frac{1}{\nu}\delta(1 - \frac{Q^2}{2m_\mu\nu}) \tag{3.55}$$

$$W_1^{e\mu} = \frac{Q^2}{4m_\mu^2\nu}\delta(1 - \frac{Q^2}{2m_\mu\nu}) \tag{3.56}$$

By substituting this result into equation 3.54 and using the δ–function condition, one gets:

$$R^\mu = \frac{4m_\mu^2}{Q^2} \stackrel{Q^2\to\infty}{\longrightarrow} 0 \tag{3.57}$$

Adopting this results for quarks, one expects R to approach 0 if quarks have spin 1/2. In other words:

$$\sigma_L \to 0 \qquad \text{for spin } \frac{1}{2} \tag{3.58}$$

How can one measure R experimentally? One can rewrite the cross section given by equation 3.42 in the form:

$$\frac{\mathrm{d}^2\sigma}{\mathrm{d}\Omega \mathrm{d}E'} = \Gamma(\sigma_T + \epsilon\sigma_L) \tag{3.59}$$

where the photon polarization ϵ is expressed as:

$$\epsilon = [1 + 2\frac{Q^2+\nu^2}{Q^2}\tan^2\frac{\theta}{2}]^{-1} \tag{3.60}$$

and the photon flux Γ is written in the form:

$$\Gamma = \frac{K\alpha}{2\pi^2 Q^2}\frac{E'}{E}\frac{1}{1-\epsilon} \tag{3.61}$$

Thus the cross section can be written as:

$$\frac{\mathrm{d}^2\sigma}{\mathrm{d}\Omega \mathrm{d}E'} = \Gamma\sigma_T\left(1 + \epsilon\frac{\sigma_L}{\sigma_T}\right) = \Gamma\sigma_T(1+\epsilon R) \tag{3.62}$$

The polarization ϵ is a function of ν, Q^2 and θ. By keeping ν and Q^2 fixed and by changing θ and E one expects a straight line when plotting the differential cross section as function of ϵ, as shown in figure 3.5. Thus one can fit directly the intercept ($= \Gamma\sigma_T$) and the slope ($= R$) and once R is known, $\frac{\mathrm{d}^2\sigma}{\mathrm{d}\Omega \mathrm{d}E'}$ depends only on one structure function.

We see therefore that measuring R not only gives information about the spin structure of the proton constituents but is also necessary if one wants to obtain the structure functions from the measured cross sections. Before describing how one determines the structure functions, one needs to take into account an additional important effect, namely radiative corrections, which are described in the next section.

3.3 Radiative corrections

In order to determine the structure functions, one needs to know the Born cross section. However, the measured cross section includes in addition to the Born one contributions from a whole set of electroweak radiative processes. The radiation can come from the electron (either from the incoming or from the outgoing one), it can come from the hadron side, by having a quark radiate a photon and there are interference terms. On top of that there are loop and vertex corrections. In the following we present some of the diagrams included in the calculations of radiative corrections.

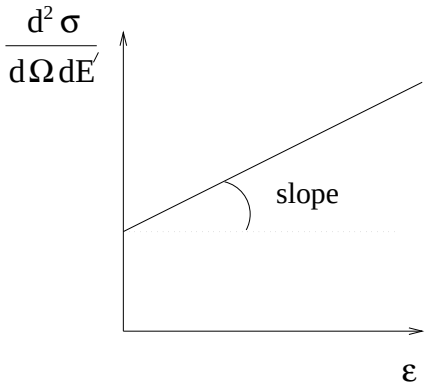

Figure 3.5: The differential cross section as function of the photon polarization ϵ for fixed ν and Q^2.

First, the radiation from the electron line. These contributions are the source of the largest corrections. In the diagrams (a) and (b) the simplest $\mathcal{O}(\alpha^3)$ graphs for real photon emission at the leptonic vertex and in (c) and (d) the $\mathcal{O}(\alpha^3)$ contributions from virtual photons associated with the leptonic vertex are shown.

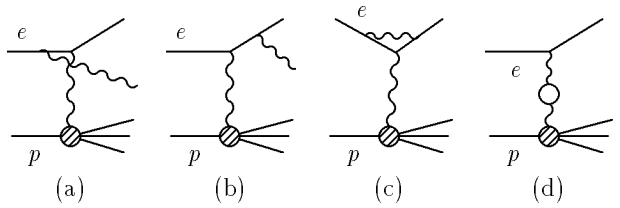

(3.63)

The radiative corrections coming from the hadron line are less important than the contributions of photons radiated off the electron. The following three diagrams have to be corrected for the radiation of a photon from quarks:

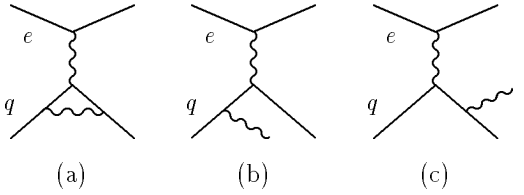

(3.64)

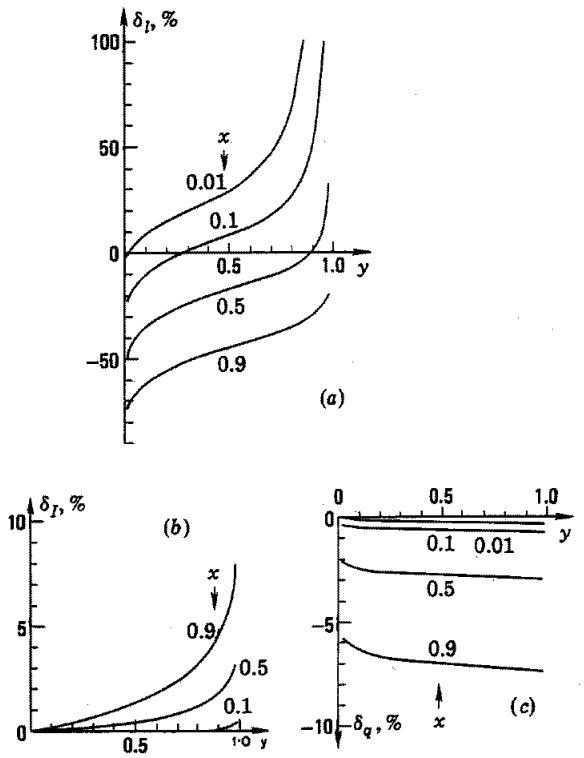

Figure 3.6: QED radiative corrections: (a) from the lepton line, (c) from the quark lines, and (b) from their interference.

Finally there are the interference term corrections described diagramatically as:

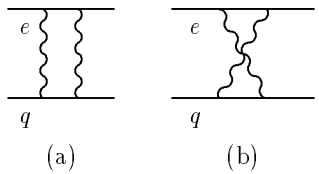

(3.65)

One can get a feeling for the magnitude of these corrections [48] at HERA from the plots shown in figure 3.6. As one sees, the corrections depend strongly on the kinematical region and for small x and high y can be very large.

3.4 Experimental determination of the structure functions

The expression of the Born cross section contains two structure functions, W_1 and W_2. One can use instead the structure function F_1 and F_2 which are related to the former ones as follows:

$$F_1 = W_1 \tag{3.66}$$

$$F_2 = \frac{\nu W_2}{m_p} \tag{3.67}$$

Thus one can write the Born cross section in the form:

$$\frac{\mathrm{d}^2\sigma^{\mathrm{Born}}}{\mathrm{d}x\mathrm{d}Q^2} = \frac{4\pi\alpha^2}{xQ^4}[\frac{y^2}{2}2xF_1 + (1-y)F_2] \tag{3.68}$$

The first measurements of the structure functions showed that the data were compatible with the Callan–Gross [49] relation

$$2xF_1(x) = F_2(x). \tag{3.69}$$

With more precise DIS data covering a larger range of x and Q^2 a clear scale breaking was observed and thus one needs information about the difference between the two structure functions, defined as $F_L \equiv F_2 - 2xF_1$. By defining the ratio of the structure functions R_L as follows:

$$R_L \equiv \frac{F_L}{F_2} \tag{3.70}$$

one can express the Born cross section as:

$$\frac{\mathrm{d}^2\sigma^{\mathrm{Born}}}{\mathrm{d}x\mathrm{d}Q^2} = \frac{4\pi\alpha^2}{xQ^4}F_2Y_+(1-\frac{y^2}{Y_+}R_L); \qquad Y_+ = 1+(1-y)^2 \tag{3.71}$$

However, in addition to the Born cross sections there are radiative processes. So the cross section which includes these radiative processes is expressed in the form:

$$\frac{\mathrm{d}^2\sigma^{\mathrm{rad}}}{\mathrm{d}x\mathrm{d}Q^2} = \frac{4\pi\alpha^2}{xQ^4}F_2Y_+(1-\frac{y^2}{Y_+}R_L)[1+\delta_r(x,Q^2)] \tag{3.72}$$

where $\delta_r(x,Q^2)$ are the contributions coming from the radiative processes.

If one had an ideal detector which measures every outgoing particle from the reaction with a 100 % precision and with a background–free identification of the processes, this would be the cross section from which the structure function would be determined. In

reality one measures something which is somewhat different than the above expression. The measured cross section is connected to the one in equation 3.72 in the following way:

$$\frac{\mathrm{d}^2\sigma^{\mathrm{meas}}}{\mathrm{d}x\mathrm{d}Q^2} = \int \mathrm{d}x' \int \mathrm{d}Q'^2 \frac{\mathrm{d}^2\sigma^{\mathrm{rad}}}{\mathrm{d}x'\mathrm{d}Q'^2} A_{cc}(x', Q'^2) S(x, Q^2; x', Q'^2) + \text{background} \qquad (3.73)$$

Here A_{cc} is the probability that an event which is produced at x', Q'^2 will be seen in the detector, which is thus a function of the geometry and efficiency of the detector, and S is a smearing function which gives the probability that an event which is produced at x', Q'^2 was measured at x, Q^2.

The experimental procedure to measure the structure functions includes thus the following steps:

- One selects a sample of events likely to be NC DIS events. This means that one needs to have a good electron finder [50] which has both high efficience and high purity for electron identification. This requirement usually results in the fact that only electrons having energies above a certain values can be identified.
- The values of x and Q^2 are determined by one of the methods described in the kinematic section.
- The background coming from non–DIS events has to be subtracted. An example of such a background could be a photoproduction events, where the scattered electron remained undetected in the beam pipe, in which a π^0 was produced which decayed into two photons, one of which produced an electromagnetic shower and was mistakenly identified as an electron. This background can be measured in certain kinematic regions and has to be estimated in others.
- Using the luminosity measurements one gets the measured cross section, from which one has to unfold the one given by equation 3.72.
- One needs to apply the radiative corrections to get the Born cross section. In order to be able and do the calculations, one needs good parameterizations of structure functions at lower Q^2 down to the photoproduction region.
- Finally, in order to get the structure function F_2, one needs information on F_L, or equivalently on R_L. This ratio was measured [51, 52] in some of the fixed target experiments but is limited to relatively high x values. There is no measurements on R in the HERA x range and so far one needs to rely on its estimates calculated from QCD. This is one of the sources of the systematic errors of F_2.

We have already shown the latest results of F_2 as measured in the whole kinematic region, as function of x, for fixed values of Q^2 (figure 1.8), and which show the dramatic rise of the structure function as x decreases. Here we show the values of F_2 as function of Q^2,

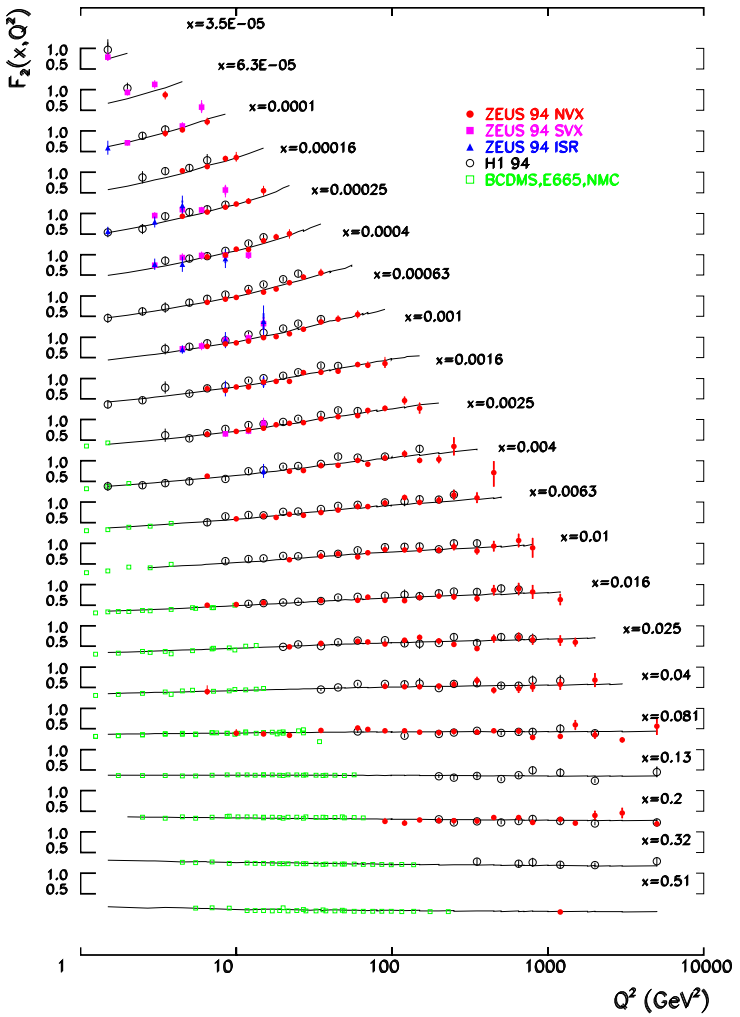

Figure 3.7: The structure function $F_2(x, Q^2)$ as function of Q^2, for fixed x values.

for fixed values of x (figure 3.7). In addition to the HERA measurement, the figure includes data from some fixed target experiments. A clear scale breaking with Q^2 is observed. The curves are the results of a QCD fit to the data.

3.5 Summary

In this chapter we discussed the following issues:

- The different kinematical variables which are used in the study of DIS have been defined. In particular, we saw that the scaling variable x, defined by Bjorken, can be interpreted as the fraction of the proton momentum carried by the struck parton, under the assumption of an infinite momentum frame with massless partons. The variable y is the inelasticity of the exchanged photon in a system where the target proton is at rest. In that system ν is the energy of the exchanged photon and y is the fraction of the incoming lepton taken by the exchanged photon.

- We described three different methods for the determination of x and Q^2 at HERA: the electron method, the hadron method (Jacquet–Blondel) and a mixed method using two angles (double–angle). We calculated the kinematic limits at HERA obtaining $Q^2_{max} = 9 \times 10^4$ and $x_{min} \approx 10^{-6}$. At present HERA has measurements at Q^2 values as high as about $10000\,\mathrm{GeV}^2$ and as low as $0.2\,\mathrm{GeV}^2$.

- The proton structure functions have been defined and their relation to $\sigma(\gamma^* p)$ has been given. Two definitions of the fluxes for this relation, the Gilman and the Hand one have been given. The ratio of the longitudinal to transverse cross section of the $\gamma^* p$ system was defined and we showed that it can be determined by measuring the DIS cross section as function of the photon polarization, for fixed ν and Q^2.

- The radiative processes have been described briefly and their importance in the structure function determination has been discussed. The size of the corrections depend on the kinematical regions in x and y and can be very large in the high y region.

- The different steps necessary for the experimental determination of the proton structure function have been described. One of the missing measurements in order to reduce the systematic error on F_2 in the HERA kinematic region is that of R, the ratio of the longitudinal structure function F_L to F_2.

Chapter 4

Parton Distributions in the Proton

In the last chapter we have seen how to obtain the proton structure function from the measured DIS cross section. What does it teach us about the structure of the proton? How can one use it to learn about the behaviour of the proton's constituents?

In order to do so, one needs a theory which connects the parton distributions within the proton to its measured structure function [53]. For short distance forces one can use perturbative calculations in QCD to get such a relation. However, there are also long distance dependencies where non–perturbative effects are present. One of the most important results of Field theory is the proof that the structure function can be factorized into short distant dependences, calculable in perturbative QCD (pQCD), and non–perturbative long distance dependences. This QCD factorization theorem will be the subject of the first section.

We will proceed with the DGLAP evolution equations of partons and discuss the structure function in the low–x region. This will lead to the BFKL evolution equation and to a short discussion about saturation. The last two sections will be devoted to parameterizations of parton distributions in the proton and to experimental determination of the gluon density in the proton.

4.1 The QCD factorization theorem

The QCD factorization theorem [54] discusses the situation where one measures an inclusive reaction, like the NC DIS one: $ep \to eX$. In this case one can prove that the structure functions can be factorized into short-distance dependences calculable in pQCD and into long-distance dependences which need to be taken from outside the theory. If we denote by F_a^{Vh} the structure function for a hadron h which is probed by a vector V, where a can be 1, 2 or 3 (in case of Z^0 exchange) the QCD factorization theorem allows to write the

following equations:

$$F_{1,3}^{Vh}(x,Q^2) = \sum_{f,\bar{f},g} \int_x^1 \frac{\mathrm{d}z}{z} C_{1,3}^{Vi}\left(\frac{x}{z}, \frac{Q^2}{\mu^2}, \frac{\mu_{\mathrm{F}}^2}{\mu^2}, \alpha_S(\mu^2)\right) f_{\mathrm{i/h}}(z,\mu_F,\mu^2) \tag{4.1}$$

$$F_2^{Vh}(x,Q^2) = \sum_{f,\bar{f},g} \int_x^1 \mathrm{d}z\, C_2^{Vi}\left(\frac{x}{z}, \frac{Q^2}{\mu^2}, \frac{\mu_{\mathrm{F}}^2}{\mu^2}, \alpha_S(\mu^2)\right) f_{i/h}(z,\mu_F,\mu^2) \tag{4.2}$$

The coefficient functions C_a^{Vi} are independent of long distance effects and are computable in pQCD. The functions $f_{i/h}$ are the parton distribution functions which are specific to the hadron h but are universal as far as a and V are concerned. They are not calculable in pQCD but have to be measured experimentally.

There are two mass scales in the problem. One is the renormalization scale μ. The other one is the factorization scale μ_F. If we denote by k^2 the off–shellness, then for $k^2 > \mu_{\mathrm{F}}^2$ one has the coefficient functions while for $k^2 < \mu_{\mathrm{F}}^2$ one has the parton distribution functions. This can be pictured for the DIS case in the following diagram:

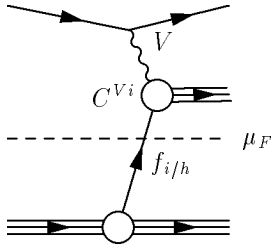

(4.3)

In the absence of any interaction (γ^* is absorbed by the quark i which continues) these functions are, in leading order, the following:

$$C_a^{\gamma i(0)}(x) = e_i^2 \delta(1-x) \tag{4.4}$$

$$f_{i/i}^{(0)}(z) = \delta(1-z) \tag{4.5}$$

Beyond the leading order, there is considerable ambiguity and one has to specify in which scheme one works. There are usually two different schemes: the DIS and the $\overline{\mathrm{MS}}$ schemes. In the DIS scheme, order by order in perturbative theory all corrections to F_2^{Vh} are absorbed into the distribution functions of q and $\bar{q}$ (for $\mu = \mu_F = Q$):

$$C_2^{Vq}(x) = e_q^2 \delta(1-x) \tag{4.6}$$

$$C_2^{V\bar{q}}(x) = e_{\bar{q}}^2 \delta(1-x) \tag{4.7}$$

$$C_2^{Vg}(x) = 0 \tag{4.8}$$

The $\overline{\mathrm{MS}}$ scheme (modified minimal subtraction) follows from the idea of dimensional regularization by 'tHooft and Veltman [55].

4.2 The QCD evolution equation for partons

Though, as we noted above, the parton distribution functions can not be calculated by pQCD, the theory provides a way to predict how these distributions should evolve with the scale Q^2, once they are given at an initial scale. Before we proceed to describe these evolution equations, we would like to note that the QCD factorization theorem was proven only in leading twist and thus the expression for the structure function includes also higher twist terms (note that we have somewhat simplified the notation):

$$F(x,Q^2) = \sum_i \int_x^1 \mathrm{d}z\, C_i\left(\frac{x}{z}, \alpha_S(\mu_\mathrm{F}^2), \frac{Q^2}{\mu_\mathrm{F}^2}\right) f_i(z,\mu_\mathrm{F}^2) + \mathcal{O}\left(\frac{\Lambda^2}{Q^2}\right) \tag{4.9}$$

where Λ is the QCD scale.

F is a measurable quantity and therefore can not depend on μ_F:

$$\mu_\mathrm{F}^2 \frac{\mathrm{d}F(x,Q^2)}{\mathrm{d}\mu_\mathrm{F}^2} = 0 \tag{4.10}$$

The splitting functions $P_{ij}(z,\alpha_S(\mu^2))$ are defined to represent the process in which a quark with a momentum fraction x radiates a parton of a momentum fraction $(1-z)x$ and continues with a fraction momentum zx:

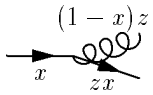

(4.11)

Then one can write the following equation for the parton distribution function f_i:

$$\frac{\mathrm{d}f_i(x,\mu^2)}{\mathrm{d}\ln\mu^2} = \sum_j \int_x^1 \frac{\mathrm{d}z}{z} P_{ij}(z,\alpha_S(\mu^2)) f_i(\frac{x}{z},\mu^2) \tag{4.12}$$

This set of integro–differential equations is named DGLAP [56, 57, 58] after Dokshitzer, Gribov, Lipatov, Altarelli and Parisi.

The splitting functions P_{ij} give the probability of finding parton i in parton j. They can be expanded in orders of $(\alpha_S/2\pi)$:

$$P_{ij}(z,\alpha_S) = \sum_{n=1}^{\infty} \left(\frac{\alpha_S}{2\pi}\right)^n P_{ij}^{(n-1)}(z) = \frac{\alpha_S}{2\pi} P_{ij}^{(0)}(z) + \left(\frac{\alpha_S}{2\pi}\right)^2 P_{ij}^{(1)}(z) + \ldots \tag{4.13}$$

A similar expansion can be written for the coefficient functions C_i:

$$C_i(z,\alpha_S) = \alpha_S^p \left[C_i^{(0)} + \frac{\alpha_S}{2\pi} C_i^{(1)}(z) + \left(\frac{\alpha_S}{2\pi}\right)^2 C_i^{(2)}(z) + \ldots\right] \tag{4.14}$$

where the value of p depends on the initial process.

The partonic picture of the pQCD evolution for F_2 can be represented diagramatically by the following picture:

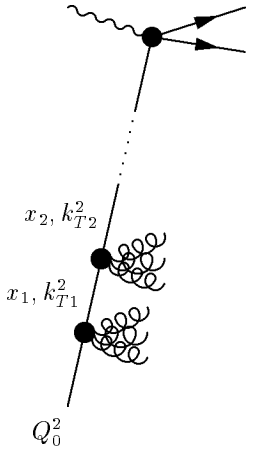

(4.15)

Each blob in the chain has a structure like this:

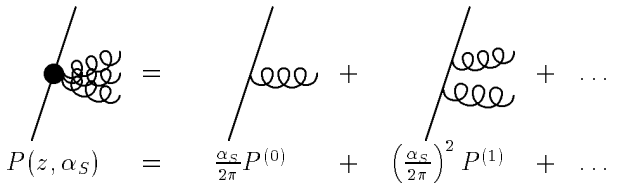

(4.16)

There is strong ordering in the transverse momenta k_T of each leg. If there are m steps

in the chain, each having a transverse momentum square of k_{Ti}^2, then:

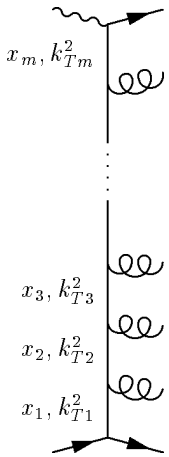

DGLAP

$$x_1 > x_2 > x_3 \ldots > x_m = x \qquad (4.17)$$

$$k_{T1}^2 \ll k_{T2}^2 \ll \ldots \ll k_{Tm}^2 = Q^2$$

If we take only the terms $C^{(0)}$ and $P^{(0)}$, we do leading order perturbation calculation. The terms $C^{(1)}$ and $P^{(1)}$ give next to leading order calculations. However by solving the DGLAP equations, we sum up the terms $(\alpha_S \ln \frac{Q^2}{\Lambda^2})^m$ to all orders. In this case one is performing a leading log approximation in $\ln Q^2$, usually shortened as LLA($\ln Q^2$) or just LLA. One should note that the splitting functions $P_{ij}^{(n)}(x) \sim (1/x) \ln x^{n-1}$, which gets logarithmically enhanced at low x. Thus, if one takes only the first two terms, $n = 1, 2$, one is restricted to moderate x only.

4.2.1 DGLAP equations in leading order

One can write the DGLAP equations in leading order in the following form:

$$\frac{\mathrm{d}q_i(x,Q^2)}{\mathrm{d}\ln Q^2} = \frac{\alpha_S(Q^2)}{2\pi} \int_x^1 \frac{\mathrm{d}z}{z} \left[\sum_j q_j(z,Q^2) P_{ij}^{(0)}(\frac{x}{z}) + g(z,Q^2) P_{ig}^{(0)}(\frac{x}{z}) \right] \qquad (4.18)$$

$$\frac{\mathrm{d}g(x,Q^2)}{\mathrm{d}\ln Q^2} = \frac{\alpha_S(Q^2)}{2\pi} \int_x^1 \frac{\mathrm{d}z}{z} \left[\sum_j q_j(z,Q^2) P_{gj}^{(0)}(\frac{x}{z}) + g(z,Q^2) P_{gg}^{(0)}(\frac{x}{z}) \right] \qquad (4.19)$$

The parton which is probed at the scale of Q^2 by the virtual vector meson, has a fractional momentum x which is the result of a chain of splitting which started from the parent parton. Since the longitudinal momentum of the daughter parton is always smaller or equal to that of the parent one, the integration is restricted to $x \leq z \leq 1$. Also if one neglects the masses of the quarks, the change in the distribution function depends only on

the ratios of longitudinal momenta x/z. The sum j is over the quark flavours, and one assumes that the splitting functions are flavour independent. Thus:

$$P_{ij}^{(0)} = \delta_{ij} P_{ii} = \delta_{ij} P_{gg} \qquad (4.20)$$

$$P_{gj} = P_{gq} \qquad P_{ig} = P_{qg} \qquad (4.21)$$

Conservation of momentum for a parent quark and a gluon gives:

$$\int_0^1 \mathrm{d}z\, z\, [P_{qq}(z) + P_{gq}(z)] = 0 \qquad (4.22)$$

$$\int_0^1 \mathrm{d}z\, z\, [2n_f P_{qg}(z) + P_{gq}(z)] = 0 \qquad (4.23)$$

where n_f is the number of flavours, and

$$P_{qq}(z) = P_{gq}(1-z) \qquad (4.24)$$

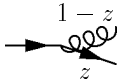

$$P_{qg}(z) = P_{qg}(1-z) \qquad (4.25)$$

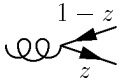

$$P_{gg}(z) = P_{gg}(1-z) \qquad (4.26)$$

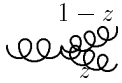

In leading order the quark–parton model (QPM) relations between structure functions and parton distributions hold. So it is easy to derive the evolution equations for the structure functions. One usually defines the colour singlet combination, which evolves with gluons:

$$x\Sigma(x) = \sum_{i=1} n_f\, [x q_i(x) + x\bar{q}_i(x)] \qquad (4.27)$$

The colour non–singlet combination, which evolves with quarks, is:

$$xV(x) = \sum_{i=1} n_f\, [x q_i(x) - x\bar{q}_i(x)] \qquad (4.28)$$

Leading order splitting function

For completeness we give her the explicit form of the leading order splitting functions:

$$P_{qq}^{(0)}(x) = \frac{4}{3}\left[\frac{1+x^2}{(1-x)_+} + \frac{3}{2}\delta(1-x)\right] \quad (4.29)$$

$$P_{qg}^{(0)}(x) = (1-x)^2 + x^2 \quad (4.30)$$

$$P_{gq}^{(0)}(x) = \frac{4}{3}\frac{(1-x)^2+1}{x} \quad (4.31)$$

$$P_{gg}^{(0)}(x) = 6\left[\frac{x}{(1-x)_+} + \frac{1-x}{x} + x(1-x)\right] + \left[\frac{11}{2} - \frac{n_f}{3}\right]\delta(1-x) \quad (4.32)$$

where we used the following definition:

$$\int_0^1 \mathrm{d}z\, \frac{f(z)}{(1-z)_+} \equiv \int_0^1 \mathrm{d}z\, \frac{f(z)-f(1)}{(1-z)} \quad (4.33)$$

4.3 The behaviour of F_2 at low x

What do the DGLAP equations tell us about the behaviour of the structure function at low x? We have already seen earlier that the structure function F_2^{ep} is connected to the $\gamma^* p$ cross section via the relation:

$$F_2^{ep}(x,Q^2) = \frac{K}{4\pi\alpha}\frac{Q^2\nu}{Q^2+\nu^2}\left(\sigma_T^{\gamma^* p} + \sigma_L^{\gamma^* p}\right) \quad (4.34)$$

The variable x can be expressed as:

$$x = \frac{Q^2}{Q^2 + W^2 - m_p^2} \quad (4.35)$$

and since we are discussing the region of low x, this means high W.

We have seen in the last part of the chapter 2 on Regge theory that the total photoproduction cross section behaves at high energies like $\sigma_{\mathrm{tot}}(\gamma p) \sim (W^2)^{0.08}$. Does this behaviour hold also for $\sigma_{\mathrm{tot}}(\gamma^* p)$? If it were so, this would mean that at low x we expect $F_2 \sim x^{-0.08}$. However, a look at the experimental data shown in figure 1.8 shows [59, 16] that $F_2 \sim x^{-0.3 \div 0.4}$. Can such a behaviour be expected from the evolution equations which we presented in the last section?

Let us write again the DGLAP equations in a shorter notation:

$$\frac{\mathrm{d}q_i}{\mathrm{d}\ln Q^2} = \frac{\alpha_S}{2\pi}\left[P_{qq}\otimes q_i + P_{qg}\otimes g\right] \quad (4.36)$$

$$\frac{\mathrm{d}g}{\mathrm{d}\ln Q^2} = \frac{\alpha_S}{2\pi}\left[P_{gq}\otimes q_i + P_{gg}\otimes g\right] \quad (4.37)$$

but since

$$P_{gg}^{(0)}(x) = 6\left[\frac{x}{(1-x)_+} + \frac{1-x}{x} + x(1-x)\right] \quad (4.38)$$

$$P_{gq}^{(0)}(x) = \frac{4}{3}\frac{(1-x)^2+1}{x} \quad (4.39)$$

we see that gluons are produced most copiously at low x. Since the q_i are small at low x, the gluon evolution equation can be approximated by:

$$\frac{\mathrm{d}g(x,Q^2)}{\mathrm{d}\ln Q^2} \simeq \frac{\alpha_S(Q^2)}{2\pi}\int_x^1 \frac{\mathrm{d}z}{z}\, P_{gg}(\frac{x}{z})\, g(z,Q^2). \quad (4.40)$$

Using $P_{gg}^{(0)} z \simeq 6/z$ one get the so–called double leading log approximation, where only terms proportional to $\ln\frac{1}{x}\ln Q^2$ are taken:

$$xg(x,Q^2) \sim \exp\left[\frac{48}{11-\frac{2}{3}n_f}\ln\frac{\ln\frac{Q^2}{\Lambda^2}}{\ln\frac{Q_0^2}{\Lambda^2}}\ln\frac{1}{x}\right]^{1/2} \quad (4.41)$$

where Q_0^2 is the starting scale for the Q^2 evolution. Numerically this expression has the same value as $\approx x^{-0.4}$.

This result however has a few problems: (1) it violates unitarity and (2) since in general the functions $P_{ab}^{(n)} \sim \frac{1}{x}\left(\ln^{n-1} x + \mathcal{O}(\ln^{n-2} x)\right)$ the series does not converge and thus higher orders are needed.

4.4 The BFKL evolution equation

The DGLAP equations give us a way to see how a parton distribution which is given at an initial scale Q_0^2 evolves to higher Q^2. Since Q^2 increases one has to resume the leading $\alpha_S \ln Q^2$ terms. When the ep center of mass energy is large, like at HERA, there is a second variable which becomes large, namely $1/x \sim s/Q^2$. In this case one has to resum the leading $\alpha_S \ln(1/x)$ contributions. The BFKL [60, 61, 62] equations do such a resummation. As one evolves to smaller x, there is no more strong ordering in k_T^2. The strong ordering is rather in x and therefore one considers here the unintegrated (over the gluon transverse

momentum) gluon density distribution.

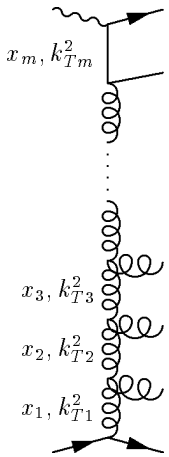

BFKL (only gluon–gluon ladder)

$x_1 \gg x_2 \gg x_3 \ldots \gg x_m = x$

no ordering in k^2_{Ti} (4.42)

(assume no evolution in Q^2)

$k^2_{T1} \simeq Q^2$

At a given Q^2, gluons have a distribution in x and k_T, $f_g(x, k_T)$, which is related to $xg(x, Q^2)$ through:

$$xg(x, Q^2) = \int_0^{Q^2} \frac{\mathrm{d}k_T^2}{k_T^2} f_g(x, k_T^2) \tag{4.43}$$

Summing up all ladder diagrams in $\ln(1/x)$ gives the BFKL equation:

$$-x\frac{\partial f_g(x,k_T^2)}{\partial x} = 3\frac{\alpha_S}{\pi}k_T^2 \int_0^{\infty} \frac{\mathrm{d}k_T'^2}{k_T'^2} \left[\frac{f_g(x,k_T'^2) - f_g(x,k_T^2)}{|k_T'^2 - k_T^2|} + \frac{f_g(x,k_T^2)}{\sqrt{4k_T'^4 + k_T^4}} \right] \equiv K \otimes f_g \tag{4.44}$$

where K is the BFKL kernel. Note that this equation relates only to gluon distributions, as also seen from the diagram. It does not discuss the Q^2 evolution. It is an equation which describes what happens to the gluon distribution when one starts from a distribution at x_0 (of the order of ≈ 0.01) and evolves to smaller x values.

The solution of the BFKL equation, after integrating over the gluon k_T, has an x dependence like:

$$xg(x, Q^2) \sim x^{-\lambda} \tag{4.45}$$

where, for fixed α_S, can be expressed as $\lambda = (3\alpha_S/\pi)4\ln 2$. Since $x^{-\lambda} \sim s^{\lambda}$, one obtains an energy dependence of the gluon density which is expected from the Regge theory at high energies. Thus BFKL succeeded to 'reggeize' the gluon and provide a connection between QCD and Regge theory. The exponent λ is usually said to be 0.5, though this requires $\alpha_S = 0.18$, which happens only at high Q^2.

If we assume that k_T is large, one gets a Q^2 dependence of the form:

$$xg(x, Q^2) \sim \sqrt{\frac{Q^2}{Q_0^2}} x^{-\lambda}, \tag{4.46}$$

which gives a stronger scaling violation than the one from the DGLAP equations ($\sim \ln Q^2$). Note that this solution is obtained in the leading log approximation (LLA) in $\ln(1/x)$.

These equations also have some problems: (1) the LLA solution violates unitarity, (2) higher order corrections are not yet available, (3) the integration on k_T starts from 0, thus one enters also the non-perturbative region, and (4) the equation doesn't have implicitly energy–momentum conservation.

4.4.1 Some consequences from the BFKL equation

BFKL Pomeron

We have seen in the Regge theory chapter 2 that at high energies the total cross section behaves like:

$$\sigma \sim s^{\alpha_{I\!P}(0)-1} \tag{4.47}$$

Since the cross section at high energies (low x) is driven by the gluons, and since the x dependence of the gluons is $\sim x^{-\lambda} \sim s^{\lambda}$, the Pomeron intercept comes out to be in this case:

$$\alpha_{I\!P}(0) = 1 + \lambda \approx 1.5 \tag{4.48}$$

in contrast to the result of $\alpha_{I\!P}(0) = 1.08$ as obtained by the analysis of Donnachie and Landshoff. Therefore one talks about the BFKL Pomeron which has an intercept of 1.5 and a DL Pomeron of intercept 1.08. Other names used in the literature are 'hard', 'perturbative', 'Lipatov' Pomeron (1.5) and the 'soft' Pomeron (1.08). We will discuss at a later stage the question of one or two Pomerons.

Hot spots

As we said above, the BFKL equations treat only the evolution in x. Since there is no evolution in Q^2, this means that the transverse area is fixed. Let us look at the schematic presentation of the proton with some partons inside, as shown in figure 4.1. When we evolve to lower x, the number of partons increases in a fixed area, leading to an increase in the local density. This phenomena is named 'hot spots' [63]. It still has to be seen at which value of x this should happen.

Jet in the proton region

In the DGLAP picture, with the strong k_T ordering, one expects that the large k_T jet would be near the γ^*, while near the proton direction there will be just the low k_T remnant jet.

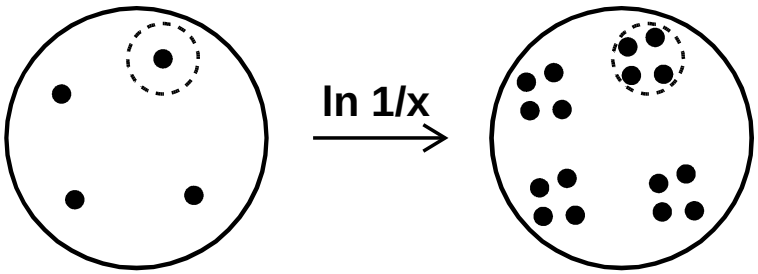

Figure 4.1: Diagram showing the increase in local density in an evolution in x.

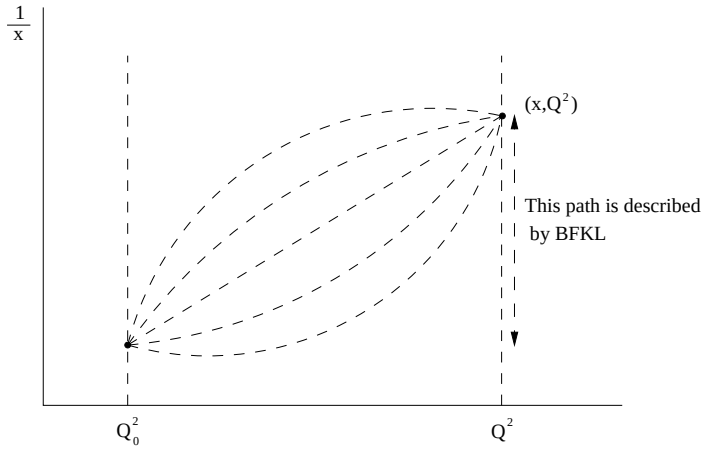

Figure 4.2: Diagram showing the evolution from point (x_0, Q_0^2) to (x, Q^2).

Since there is no strong k_T ordering in the BFKL dynamics, one can have a situation where the large k_T jet would be near the proton, in the proton direction, which will be balanced by a jet in the γ^* direction.

4.4.2 Signs for the BFKL dynamics

The behaviour of the structure function F_2 is not sensitive enough to tell the difference between the DGLAP dynamics and the BFKL one, at least not in the HERA kinematic region. Also both are compatible with a gluon density behaviour of $xg(x, Q^2) \sim x^{-\lambda}$ at low x. How then do we tell a BFKL type dynamics form a DGLAP one?

Let us look at the schematic presentation in figure 4.2. We start from a point with the coordinates (x_0, Q_0^2) and evolve to a point (x, Q^2). We can get from the one to the other in several ways. While the DGLAP equations describe the motion in the whole plain, if we give the initial conditions, the BFKL equation describes only the path along the $1/x$ axis, at a constant Q^2.

Clearly, the best way to see BFKL dynamics is to restrict the Q^2 evolution. Mueller and Navallet [64] pointed out that at low x one should look for a large transverse momentum jet near the proton direction. The large transverse momentum, compared to Q^2, guarantees a large k_T at the start of the evolution, thus forcing the rest to be an evolution only in x. Referring to figure 4.2 this would mean that we got in one step from (x_0, Q_0^2) to (x_0, Q^2). The rest would be the evolution from x_0 to x. Studying the energy behaviour of the cross section for such events and finding it rises steeply, like say $s^{0.5}$, should be a sign for the BFKL dynamics.

4.5 The CCFM equation

For sake of completeness, we should mention the existence of a unified equation developed by Catani, Ciafaloni, Fiorani and Marchesini (CCFM) [65, 66, 67]. The CCFM equation, give the BFKL solution at low x and the DGLAP one at large x. It is based on the coherent radiation of gluons which leads to a strong angular ordering of gluon emissions.

4.6 Saturation

When the density of the partons becomes very large, the partons start overlapping and coherent effects are important. The partons interact with each other. When do these effects become important? In order to answer this, let us first explain what one means by the density of partons.

The quantity $xg(x, Q^2)$ is the gluon density per unit of rapidity. In order to see that lets start from the definition of rapidity. The rapidity y is :

$$y = \frac{1}{2}\ln\frac{E+p_z}{E-p_z} = \frac{1}{2}\ln\frac{(E+p_z)^2}{E^2-p_z^2} = \frac{1}{2}\ln\frac{(E+p_z)^2}{m_T^2} = \ln\frac{(E+p_z)}{m_T} \simeq \ln\frac{2p_z}{m_T} \qquad (4.49)$$

The rapidity Δy of a parton with momentum $p_{zi} = xp$ relative to the proton is then

$$\Delta y = y_{\text{proton}} - y_{\text{parton}} = \ln\frac{2p}{m_T} - \ln\frac{2xp}{m_T} \simeq \ln\frac{2p}{2xp} = \ln\frac{1}{x} \qquad (4.50)$$

and thus $\mathrm{d}y = \mathrm{d}x/x$. The number of gluons $\mathrm{d}N_g$ is given by

$$\mathrm{d}N_g = g(x,Q^2)\mathrm{d}x = xg(x,Q^2)\frac{\mathrm{d}x}{x} = xg(x,Q^2)\mathrm{d}y \tag{4.51}$$

Therefore:

$$xg(x,Q^2) = \frac{\mathrm{d}N_g}{\mathrm{d}y} \tag{4.52}$$

meaning the number of gluons per unit of rapidity.

Let us estimate now the sizes of the gluon and of the proton. The proton size is usually taken to be $r_p \sim 1\,\mathrm{fm} \sim 5\,\mathrm{GeV}^{-1}$. The gluon radius is $r_g \sim 2/Q$, when the proton is probed at a scale of Q^2. The screening effects become important when the gluon density is of the order of the ratio of the square radiuses of the proton and the gluon:

$$xg(x,Q^2) \sim \frac{r_p^2}{r_g^2} = \frac{25\,\mathrm{GeV}}{\frac{4}{Q^2}} \simeq 6Q^2\ [\mathrm{GeV}^2] \tag{4.53}$$

In the section discussing the experimentally obtained gluon distributions we will show that for instance at $Q^2 = 20\,\mathrm{GeV}^2$, the gluon density reaches about 30 gluons per unit of rapidity at $x = 10^{-4}$. Since at this Q^2, according to equation 4.53 screening effects [68, 69] would be important at a density of about 120 gluons per unit of rapidity, one probably needs to go to much lower x values to observe screening.

4.7 Parton parameterizations

In order to describe the hadronic processes at high energies it is necessary to know the individual parton distributions as function of x and Q^2. The basic formula for a generic high energy inclusive hadronic process $A + B \to C + X$ has the form:

$$\sigma(AB \to CX) = f_A^a \otimes \hat{\sigma}_{ab\to cX} \otimes f_B^b \tag{4.54}$$

where $\hat{\sigma}$ is the calculable hard cross section for the partonic subprocess, and $f_A^a(f_B^b)$ is the distribution function of parton $a(b)$ in hadron $A(B)$. In this notation, the gluon density distribution in the proton $xg(x,Q^2)$, would be f_p^g.

Since theory does not give absolute predictions for parton distributions, they have to be obtained from some experimental input and then the DGLAP equations allow to determine those parton distributions at any Q^2, even not accessible experimentally. However parton distributions are not directly measured in the experiment. It is the structure functions or hadronic cross sections that are measured.

One way of extracting the parton distributions from the measured data is based on the approach to introduce the parton distribution at the level of the global fit. It means that the structure functions are parameterized at some reference value Q_0^2 and then evolved

numerically in Q^2 through the DGLAP equations in the kinematic regions where they are measured. A global fit is then performed to determine the best values for the starting parameters. A by–product of these fits performed on the singlet structure function F_2 is a parameterization of the gluon distribution at the reference scale Q_0^2. Because deep inelastic scattering does not constrain significantly the gluon distribution, a large variety of gluon behaviour is proposed in the literature. We will discuss the gluon density in a separate section.

It is conventional to use the following parameterization of $f_p^a(x,Q_0^2)$:

$$f_p^a(x,Q_0^2) = A_0^a x^{A_1^a}(1-x)^{A_2^a}P^a(x;A_3^a,\ldots) \tag{4.55}$$

where $P^a(x)$ is a smooth function of x. Provided the functions are sufficiently flexible to accommodate the true distributions, the particular form of the parameterization is, in principle, immaterial. The most frequent parameterizations used lately are those of Martin, Roberts and Stirling (MRS) [70, 71] and the CTEQ [72] collaboration, both of which use as a starting scale $Q_0^2 \simeq 4\,\mathrm{GeV}^2$. One example of a parameterization is the following:

$$xq_{\mathrm{NS}}(x,Q_0^2) = A_{\mathrm{NS}}x^{\delta_{\mathrm{NS}}}(1-x)^{\eta_{\mathrm{NS}}} \tag{4.56}$$

$$xq_{\mathrm{SI}}(x,Q_0^2) = A_{\mathrm{SI}}x^{\delta_{\mathrm{SI}}}(1-x)^{\eta_{\mathrm{SI}}}(1+\epsilon_{\mathrm{SI}}\sqrt{x}+\gamma_{\mathrm{SI}}x) \tag{4.57}$$

$$xg(x,Q_0^2) = A_g x^{\delta_g}(1-x)^{\eta_g} \tag{4.58}$$

where NS and SI stand for the non–singlet and the singlet functions.

Another approaches which is based on a dynamical model is that taken by Gück, Reya, and Vogt (GRV) [73]. Their assumption is that at a very low scale (chosen to be $Q_0^2 \simeq 0.34\,\mathrm{GeV}^2$), there are only valence partons which evolve to higher Q^2 to produce the sea of partons.

In figure 4.3 the F_2 structure function data measured at HERA in the low Q^2 region of $1.5 < Q^2 < 15$ GeV^2 are compared to some of the parton parameterization. Also included for $Q^2 < 4$ GeV^2 are predictions from a Regge model inspired parameterization by Donnachie and Landshoff (DL) [74]. It is evident that the QCD motivated parameterizations give a good description of the data down to quite low Q^2 values, while the DL one underestimates the data.

The GRV parameterization is compared in figure 4.4 to the total $\gamma^* p$ cross section data. As one sees, it can describe quite well the data at high energies down to low values of Q^2.

In figure 4.5 the recent measurements of the structure function down to $Q^2 = 0.16\,\mathrm{GeV}^2$ are compared to the GRV (QCD) and the DL(Regge) parameterizations. One sees a good agreement between the DL predictions and the data up to $Q^2 = 0.57\,\mathrm{GeV}^2$. The GRV predictions are completely off at the starting scale of their evolution, $Q^2 = 0.34\,\mathrm{GeV}^2$, but gives a good description of the data starting at $Q^2 = 1.5\,\mathrm{GeV}^2$.

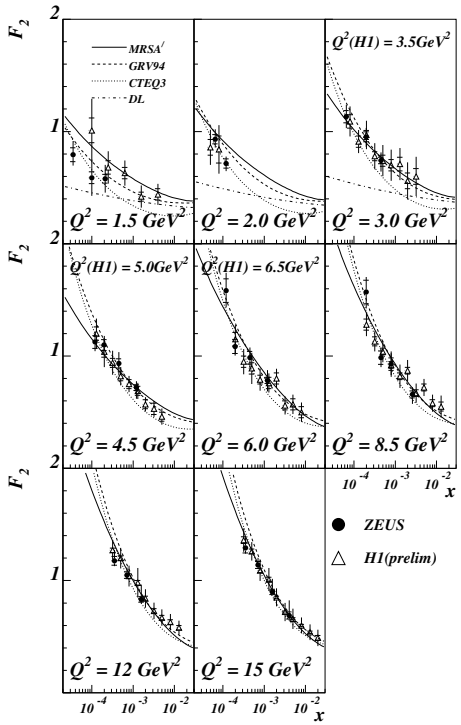

Figure 4.3: Parameterizations of parton distributions compared to ZEUS and H1 data.

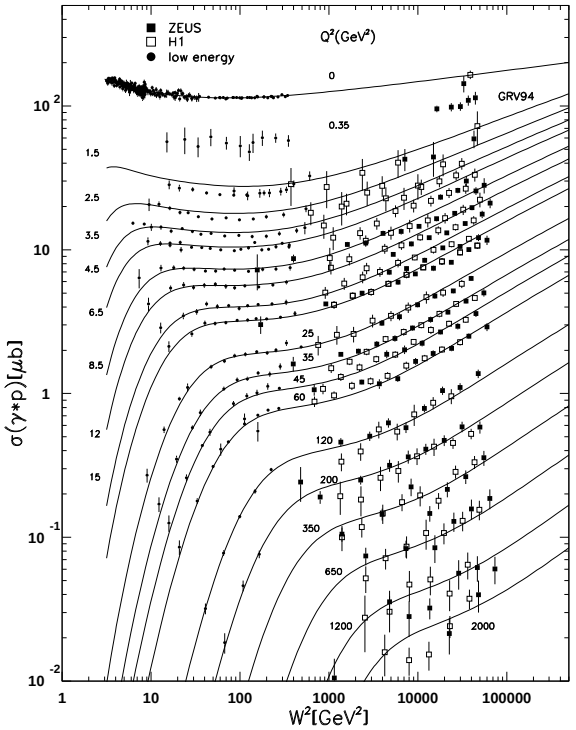

Figure 4.4: $\sigma_{tot}(\gamma^* p)$ vs W^2 compared to the GRV parameterization.

4.8 Gluon distribution in the proton at low x

The gluon density distribution is of special interest at low x since it is believed to be the source of the rise seen in the structure function as x decreases. How can one extract the gluon distribution in the proton? In principle there are two methods to do so. One is through the global QCD fits, as described above, using the inclusive DIS cross section measurements. The other is a 'direct' method, in which one uses an exclusive process, the cross section of which is proportional to the gluon density. We will describe below both methods and show results obtained so far at HERA.

4.8.1 The gluon density from global QCD fits

One can use a full global fit, using forms like in equation 4.58 to parameterize all the parton distributions, including the gluon one, and thus extract the gluon density distribution. At low x however, one can use the fact that the quark densities are much smaller than the gluon ones, to obtain the gluon density through approximate methods. One such method was provided both in leading order (LO) and in next to leading order (NLO) by Prytz [75, 76]:

$$\text{LO:} \quad xg(x,Q^2) \simeq \frac{\mathrm{d}F_2(\frac{x}{2},Q^2)}{\mathrm{d}\ln Q^2}\frac{1}{(40/27)\alpha_S/4\pi} \tag{4.59}$$

$$\text{NLO:} \quad xg(x,Q^2) \simeq \frac{\mathrm{d}F_2(\frac{x}{2},Q^2)}{\mathrm{d}\ln Q^2}\frac{1}{(40/27+7.96\alpha_S/4\pi)\alpha_S/4\pi} \tag{4.60}$$

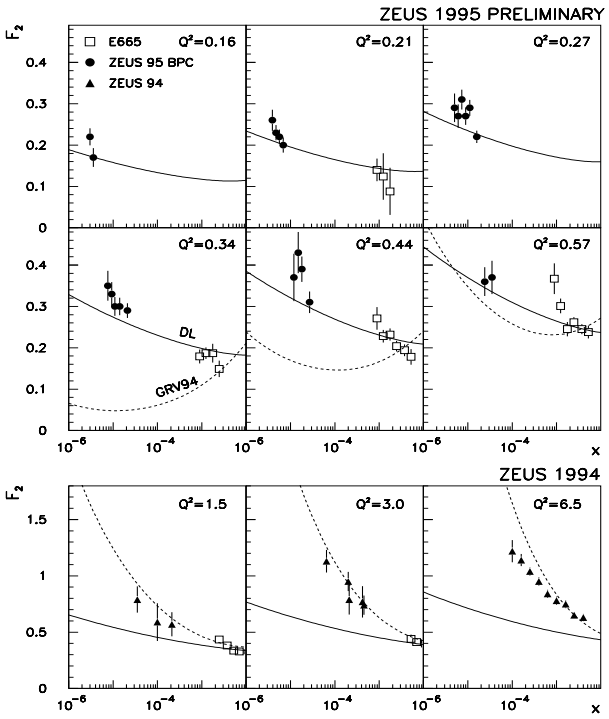

Figure 4.5: Low Q^2 measurements of the F_2 structure function at HERA, compared to the GRV and DL parameterizations.

$$-\frac{(20/9)(\alpha_S/4\pi)N(\frac{x}{2},Q^2)}{(40/27+7.96\alpha_S/4\pi)}$$

where $N(\frac{x}{2},Q^2)$ is a correction function which depends on the gluon density at large x ($x > 10^{-2}$), which is constrained by existing data. The resulting gluon distribution extracted this way can be seen ZEUS-glue(93)-95 in figure 4.6. In the same figure, results from another method (Ellis, Kunszt, Levin (EKL) [77]) and from a global QCD fit are shown for comparison. All methods give consistent results with each other.

A more recent extraction of both HERA experiments [16, 14], using a global QCD fit, are displayed in figure 4.7. The figure also shows how the higher statistics data yielded a narrower error band on the result.

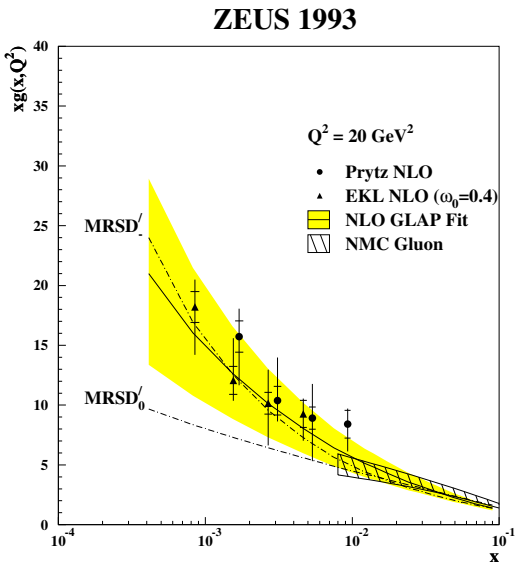

Figure 4.6: The gluon density distribution, $xg(x)$, as function of x at a fixed Q^2 of 20 GeV^2, obtained from LO and NLO approximate methods (Prytz and EKL). The result of a global fit is shown for comparison.

4.8.2 Extracting the gluon density from exclusive processes

This method is based on the fact that the cross section of some processes are proportional directly to the gluon density or to the square of the gluon density.

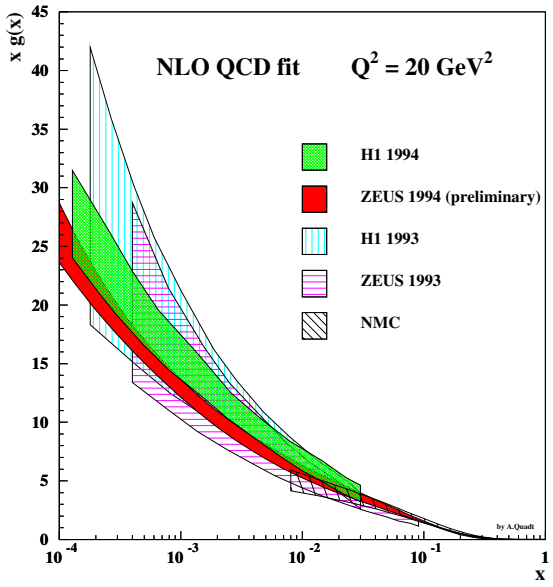

Figure 4.7: The gluon density distribution, $xg(x)$, as function of x at a fixed Q^2 of 20 GeV^2, obtained from a NLO QCD analysis of F_2.

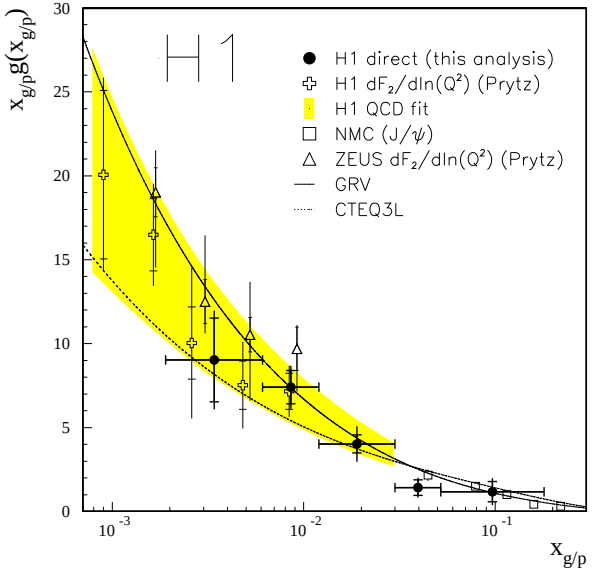

Figure 4.8: The gluon density distribution as function of x at $Q^2 = 30\,\mathrm{GeV}^2$ as determined from a leading order analysis of 2–jet events. The results are compared with those from a global QCD fit and from an approximate method.

Two–jets production in DIS

In leading order, two jet events in DIS are produced either by photon gluon fusion or by QCD–Compton scattering, the diagrams of which are:

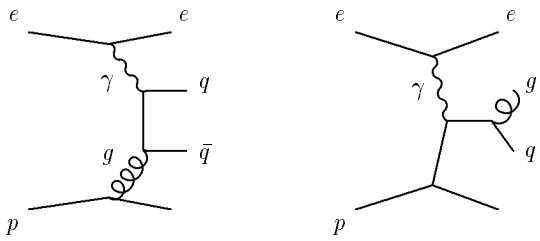

(4.61)

At small x the cross section is expected to be dominated by the photon–gluon fusion process. With this assumption one can extract [78] the gluon density, as shown in figure 4.8. This leading order extraction of the gluon density distribution is compared in the same

figure to the results from the global QCD fits and the approximate methods, described above. Note the good agreement between the different gluon determinations, which provides a check on the universality of the gluon density.

Inelastic J/Ψ production

Inelastic J/Ψ production is the process $\gamma p \to J/\Psi X$ which is described diagramatically as follows:

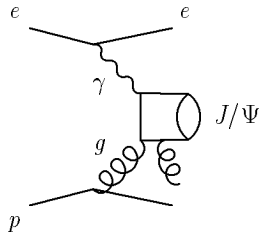

(4.62)

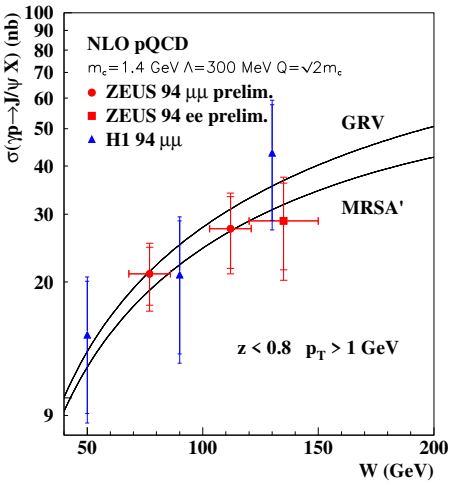

Figure 4.9: Inelastic J/Ψ cross section data as function of W compared with different choices of gluon distribution in the proton.

In this case a gluon from the proton interacts with the exchanged photon to produce a closed charm pair which radiate off a gluon and produce the colour singlet J/Ψ state. The cross section for this process is thus sensitive to the gluon density distribution in the proton. The present measurements [79, 80] are presented in figure 4.9. Though the results are well described by NLO pQCD calculations, they are not yet precise enough to be able to distinguish between different gluon density shapes.

Open charm production

The open charm process, described in the diagram below, differs from that of the inelastic J/Ψ in that there is no combinations of the produced $c\bar{c}$ pair into a colour singlet object.

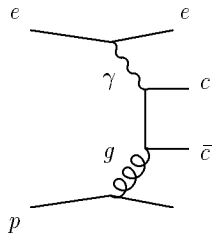

(4.63)

Instead, each charm quark hadronizes to produced a charm meson in the final state.

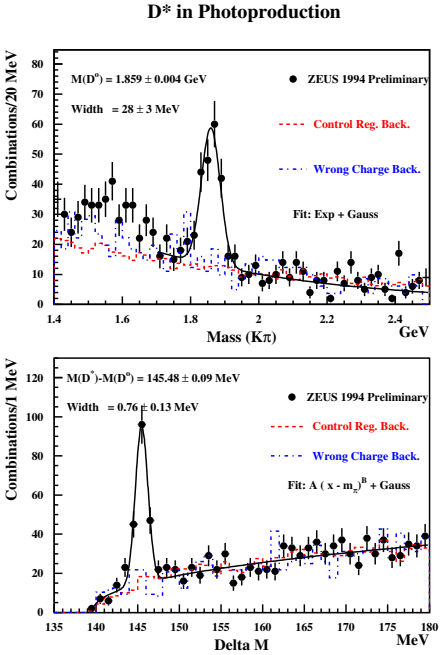

Figure 4.10: $M(K\pi)$ (top) and ΔM (bottom) distributions for events with $143 < \Delta M < 148$ MeV and $1.80 < M(K\pi) < 1.92$ GeV.

By measuring for instance the inclusive D^* production one can obtain the cross section for the process $\gamma p \to c\bar{c}X$, which is sensitive to the gluon density. Figure 4.10 shows the D^0 signal seen [81, 82, 83, 84] directly from the $(K\pi)$ mass spectrum and the signal observed in the mass difference between the D^* and the D. The cross section for inclusive open charm production is shown in figure 4.11 with lines showing predictions of different gluon density distributions. Here too data of higher accuracy, to come soon, are needed.

Elastic J/Ψ production

We will discuss this process in more detail in the last two chapters. The process of elastic vector meson production in DIS is of special interest since in can be fully calculated in QCD. As for the extraction of the gluon density, the diagram describing the process $\gamma p \to J/\Psi p$ is a two gluon exchange diagram and the cross section is proportional to the square of the gluon density distribution. The cross section for the photoproduction reaction is shown [85, 79] in figure 4.12. The curves [86] are calculations using different gluon density distributions and show the sensitivity of the cross section to the different shapes.

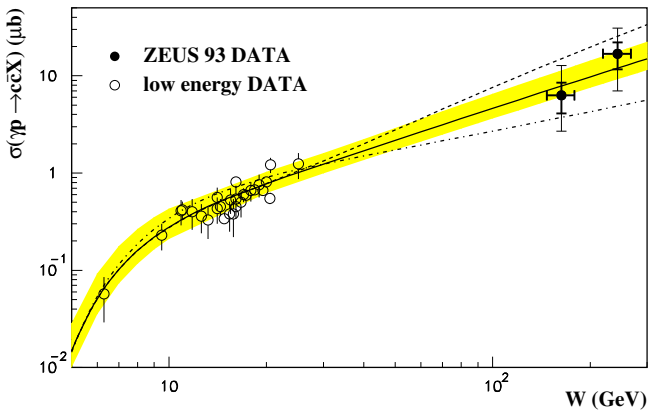

Figure 4.11: The cross section measurements for the process $\gamma p \to c\bar{c}X$ as function of the γp center of mass energy W. The solid and dashed lines represent predictions on NLO calculations using different gluon density shapes.

4.9 Summary

In this chapter we have discussed the following issues:

- We have discussed the factorization theorem which holds for an inclusive process and which allows to factorize the structure function calculation into a part which is fully calculable in pQCD, the coefficient functions, and a part which involves long distance effects and has to be obtained from the experiment, the parton distribution functions.

- Once we obtain the parton distribution functions at a given Q^2 scale, there are evolution equations which can predict the parton distribution functions at a higher scale. When the evolution is done in Q^2 one gets the DGLAP equations. These equations can describe the behaviour of the structure function F_2 at low x down to Q^2 values of $\approx 1.5\,\mathrm{GeV}^2$.

- The BFKL equation studies the evolution in x only. It predicts for the gluon density a behaviour of $x^{-\lambda}$, providing by this 'reggeization' a link between QCD and Regge theory. For a fixed α_S value, λ is of the order of 0.5. This introduces the 'BFKL Pomeron' as a trajectory with an intercept of 1.5.

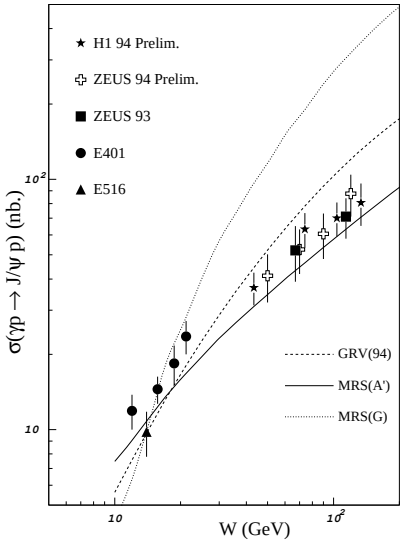

Figure 4.12: Elastic J/Ψ cross section data as function of W compared with different choices of gluon distribution in the proton.

- Presently it is not easy to find experimental signals for the BFKL mechanism. The behaviour of the structure function in the low x range provided by HERA is consistent with both the DGLAP and the BFKL approach. Signs of the BFKL mechanism can be obtained by studying the energy dependence of jets produced near the proton direction.

- We reviewed the extraction of parton distributions and discussed some of the parton parameterizations like the MRS, CTEQ and GRV. The GRV one is more than just a parameterization since it is based on a dynamical picture in which there are only valence partons at a very low scale and the sea is then built by the evolution.

- The recent HERA data at low Q^2 shows that the Regge picture works well up to about $Q^2 \approx 1\,\mathrm{GeV}^2$, while the QCD parameterizations work well down to about the same scale.

- Finally we discussed methods for the extraction of the gluon density distribution from global QCD fits and from exclusive processes. The distributions from all methods give consistent results with each other, providing a check on the universality of the gluon density.

Chapter 5

Parton Distribution in the Photon

This chapter describes the concept of the photon structure function. We will define the photon structure function after developing the formalism for that, and write the evolution equations for the photon, pointing out the differences to those of the proton. We will discuss the theoretical importance of the photon structure function and the experimental methods of extracting it from the data. Finally we will introduce some parameterizations of the photon structure function, both of real and of virtual photons.

5.1 Introduction

In the classification of elementary particles, the photon plays the role of a gauge and point–like particle, mediating electromagnetic interactions through its coupling to the charge of matter. Yet, it is well known from soft, low energy γp interactions that its behaviour can be similar to that of strongly interacting hadrons. The properties of those interactions are well described by the vector dominance model (VDM) [32], in which the photon turns first into a hadronic system with quantum numbers of a vector meson and then interacts with the target proton.

A nice justification for this model can be seen from the argument of Ioffe [87, 88]. We know from QED that a photon can fluctuate into a pair of virtual charged lepton like e^+e^-, which annihilate back to a photon. It can however also fluctuate in a quark–antiquark pair $q\bar{q}$. If the time of the fluctuation t_f is large compared to the time of the interaction $t_{\rm int}$ the interaction will occur between the $q\bar{q}$ pair and the proton, resulting in a hadronic interaction. We can estimate the fluctuation time by using the uncertainty principle. Assume a real photon ($Q^2 = 0$) with energy k interacts with a proton which is at rest. The energy difference ΔE at the vertex where the photon fluctuates into a $q\bar{q}$ pair having the same momentum as that of the photon and a mass of $m_{q\bar{q}}$ is:

$$\Delta E = (k^2 + m_{q\bar{q}}^2)^{\frac{1}{2}} - k \tag{5.1}$$

The Vector Dominance Model assumes that the fluctuation of the photon is into vector mesons, $m_{q\bar{q}} \simeq m_V$, where m_V is the vector mesom mass. For high energy photons, $k \gg m_V$ and one can approximate t_f by:

$$t_f \sim \frac{1}{\Delta E} \approx \frac{1}{k}\frac{1}{1+\frac{m_V^2}{2k^2}-1} = \frac{2k}{m_V^2} \tag{5.2}$$

The interaction time is of the order of the proton radius r_p, namely:

$$t_{\rm int} \approx r_p \tag{5.3}$$

For example, taking a $k = 10\,\text{GeV}$ photon, and $m_V = m_\rho$, one gets $t_f \approx 7\,\text{fm}$, while $t_{\rm int} \approx 0.8\,\text{fm}$ and thus the condition $t_f \gg t_{\rm int}$ holds.

When instead of a real photon one has a virtual photon ($Q^2 \neq 0$), the fluctuation time is given by

$$t_f = \frac{2k}{Q^2 + m_V^2} \tag{5.4}$$

and thus as Q^2 increases, the fluctuation time becomes smaller and the photon behaves like a point–like object. However, as we shall see later, there are conditions for which even at high Q^2 the fluctuation time will be large (see next chapter).

We thus have [89] a picture of a two–component photon:

$$|\gamma> = |\gamma>_{bare} + \text{coeff.} \times |\gamma>_h \tag{5.5}$$

in which the hadronic part is represented in VDM by

$$|\gamma>_h = a|\rho> + b|\omega> + c|\varphi> \tag{5.6}$$

This picture was verified in γp reactions by observing that for instance the reaction $\gamma p \to \pi^+\pi^- p$ is completely dominated by $\gamma p \to \rho^0 p$:

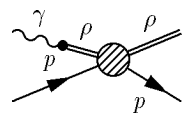

(5.7)

and also in e^+e^- experiments, by studying the reactions: $e^+e^- \to \pi^+\pi^-, \pi^+\pi^-\pi^0, K\overline{K}$, which showed the ρ^0, ω, φ:

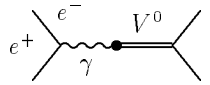

(5.8)

These reactions also provided a determination of the direct photon–vector meson coupling strength, $(4\pi/\gamma_V^2)$:

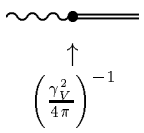

$$\uparrow \quad \left(\frac{\gamma_V^2}{4\pi}\right)^{-1} \tag{5.9}$$

and allowed to test the VDM prediction of their ratios:

$$\left(\frac{\gamma_\rho^2}{4\pi}\right)^{-1} : \left(\frac{\gamma_\omega^2}{4\pi}\right)^{-1} : \left(\frac{\gamma_\varphi^2}{4\pi}\right)^{-1} = 9 : 1 : 2 \tag{5.10}$$

The VDM predicted [89] many more relations, most of which were borne out by the data. However VDM is a model. It did not evolve from 'looking' at the photon with a probe. It related photoproduction reactions to hadron reactions by modelling the photon as a superposition of vector mesons, with direct photon–vector meson couplings which could be determined by experiment. This model worked very well at low p_T reactions.

How can one 'look' at the photon in a way similar to what has been done to the proton? The most natural way is to perform a deep inelastic scattering experiment on the photon [90] by studying $e\gamma$ reactions. First one produces a high energy photon beam by using a backscattered laser beam in a linear collider. A laser beam of about 1 eV colliding with a 0.25 TeV electron beam can produce a photon beam of about 0.2 TeV of energy:

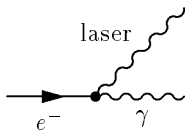

(5.11)

The resolution of such a beam can be of the order of $\Delta E_\gamma/E_\gamma \sim 10\,\%$. The high energy photon beam can then collide with another electron beam of energy 0.25 TeV giving a luminosity of the order of $\mathcal{L} \sim 10^{33}\,\mathrm{cm}^{-2}\,\mathrm{sec}^{-1}$:

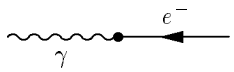

(5.12)

It is also possible to collide two real photon beams this way when such a linear collider becomes available.

For the time being one has to use e^+e^- interactions leading to two–photon exchange, as depicted in the diagram in figure 5.1. When one of the photons with very small virtuality

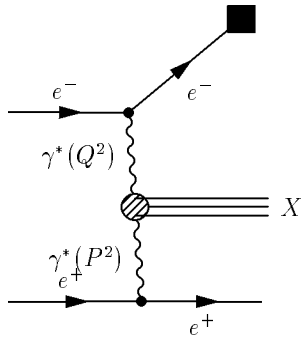

Figure 5.1: Two–photon exchange in e^+e^- scattering.

($P^2 \approx 0$) interacts with the other one with high virtuality (Q^2) ('single–tag' configuration), the interaction can be thought of as a DIS of one photon on the other, in which case the situation is similar to the probing of a proton by a highly virtual photon. It is therefore natural to introduce the notion of the photon structure function in analogy to the well–known proton one. We will introduce the formalism in the next section.

5.2 Formalism

The DIS for $e\gamma$ interaction [91] is depicted in the following diagram:

$$e\gamma \to eX \qquad \mathrm{d}\sigma \sim \sum \left| \right|^2 \tag{5.13}$$

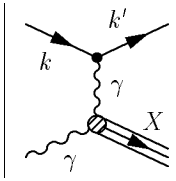

To stress the analogy with the proton case, we also show the DIS of the ep case:

$$ep \to eX \qquad \mathrm{d}\sigma \sim \sum \left| \right|^2 \tag{5.14}$$

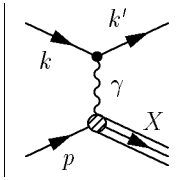

We will start with the e^+e^- reaction, with the notations as defined in the diagram below, and develop the cross section formalism for the reaction $e^+e^- \to e^+e^-X$, from which we will get that of the DIS reaction $e\gamma \to eX$.

$ee \to eeX$

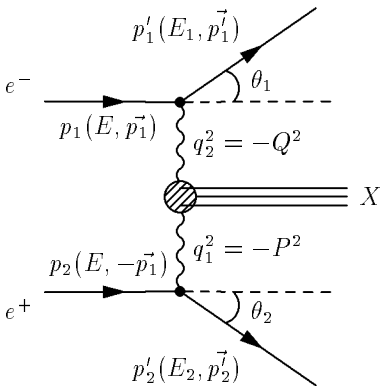

(5.15)

The matrix element for the reaction $e^+e^- \to e^+e^-X$ has 256 components. These can be reduced to 81 using gauge invariance and by further applying the optical theorem and P, T invariance one is left with the following 6 independent components: $\sigma_{tt}, \sigma_{tl}, \sigma_{lt}, \sigma_{ll}, \tau_{tt}, \tau_{tl}$. Here t stand for transversely and l for longitudinally polarized photon states, while τ denote their interference. Integrating over the scattering plane of the leptons and using the fact that the target photon is almost real and thus only transversally polarized, one has only the two independent components σ_{tt} and σ_{lt}.

The reaction $ee \to eeX$ can be viewed as a two–step process. In the first step the target photons are radiated by one of the electrons and are then probed in a DIS by highly virtual photons γ^* emitted by the second electron. In order to take into account the momentum spread of the target photons and their slight off–shellness, one uses the equivalent photon approximation (EPA). In this approach, described by the Weizsäcker–Williams formula [92, 93], the photons are assumed to be emitted real and their momentum spread is modified appropriately.

One can use the equivalent photon approximation (EPA) to write:

$$\mathrm{d}\sigma_{ee\to eeX} = \mathrm{d}\sigma_{e\gamma\to eX} f_{\gamma/e} \tag{5.16}$$

where

$$\mathrm{d}\sigma_{e\gamma\to eX} = \frac{\alpha E_1' \left(y^2 - 2y - 2\right) \mathrm{d}E_1' \mathrm{d}\Omega_1'}{2\pi^2 Q^2 y} \left(\sigma_{tt} + \epsilon\sigma_{lt}\right) \tag{5.17}$$

with

$$\epsilon = \frac{2(1-y)}{1+(1-y)^2} \tag{5.18}$$

where we have used the Hand definition of the flux. The factor $f_{\gamma/e}$ is the flux of the target photons, which is given by the Weizsäcker–Williams formula:

$$f_{\gamma/e} = \frac{\alpha}{\pi z}\left[\left(z^2 - 2z + 2\right)\ln\frac{E(1-z)\theta_{1max}'}{m_e z} - (1+z)\right] \tag{5.19}$$

where $z = E_\gamma/E$, m_e is the electron mass and θ_{1max}' is the limiting scattering angle of the tagged electron on the probing photon side.

5.3 Definition of photon structure functions

We can now introduce [94] the notation:

$$F_1^\gamma \equiv \frac{Q^2}{4\pi^2\alpha}\frac{1}{2x}\sigma_{tt} \tag{5.20}$$

$$F_2^\gamma \equiv \frac{Q^2}{4\pi^2\alpha}(\sigma_{tt} + \sigma_{lt}) \tag{5.21}$$

where x is the Bjorken variable as defined earlier, and, because of the massless target, has the relation:

$$x = \frac{Q^2}{Q^2 + W^2} \tag{5.22}$$

and W is the $\gamma^*\gamma$ center of mass energy. With these definitions we can write the cross section for the $e\gamma$ DIS process as:

$$\frac{\mathrm{d}\sigma(e\gamma \to eX)}{\mathrm{d}x\mathrm{d}y} = \frac{4\pi\alpha^2 s}{Q^4}[(1-y)F_2^\gamma + xy^2 F_1^\gamma] \tag{5.23}$$

which is to be compared to the proton case, where

$$\frac{\mathrm{d}\sigma(ep \to eX)}{\mathrm{d}x\mathrm{d}y} = \frac{4\pi\alpha^2 s}{Q^4}[(1-y)F_2^p + xy^2 F_1^p] \tag{5.24}$$

As one can see, the similarity is complete. Therefore, F_i^γ can be treated as the structure functions of the target photon. The experimental conditions in the single–tag e^+e^- experiments are such that the accepted values of y are small. Typically the average value of the product xy^2 are of the order $< xy^2 > \simeq 0.01 \ldots 0.02$ and therefore the F_1^γ term is usually neglected in the expression 5.23.

5.3.1 Definition of parton distributions in the photon

We will again use the analogy to the proton case to define the parton distribution in the photon [95]. Let us look again at the proton case. The deep inelastic interaction of a probe

with the proton is described by an incoherent sum of elastic scattering of the probe on free spin 1/2 quarks. This approach leads to the identification of the F_2^p structure function as a sum of the contribution of all quarks and antiquarks that build up the proton:

$$F_2^p(x) = \sum_{i=1}^{2f} x e_i^2 q_i(x) \tag{5.25}$$

where $q_i(x)$ gives, by definition, the probability of finding a particular type of quarks (antiquarks) in the proton, and xe_i^2 is the elementary 'cross section' for the elastic scattering.

In contrast to the proton, for a photon target one can predict the structure function of the photon directly from the quark parton model (QPM). One can perform a full calculation of the cross section $\gamma^*\gamma \to X$ to the lowest order in α for the process

$$\gamma^* + \gamma \to q + \bar{q} \tag{5.26}$$

which is electromagnetic with known couplings. Note however that such an approach disregards possible contributions from the hadronic component of the photon, a point to be discussed later.

In QPM one can calculate F_2^γ through the 'box' diagram

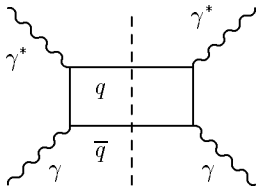

(5.27)

to get the expression [91] (for massive quarks):

$$F_2^\gamma\left(x,Q^2\right) = \frac{N_c\alpha}{\pi}\sum_{i=1}^{f} x e_{q_i}^4 \left\{\left[x^2+(1-x)^2\right]\ln\frac{Q^2(1-x)}{m_{q_i}^2 x} + 8x(1-x) - 1\right\} \tag{5.28}$$

where N_c is the number of quark colours.

By analogy to the proton case, one can think of F_2^γ as the sum of momentum–weighted densities of quarks 'inside' the photon:

$$F_2^\gamma\left(x,Q^2\right) = \sum_{i=1}^{2f} x e_i^2 q_i^\gamma\left(x,Q^2\right) \tag{5.29}$$

with:

$$q_i^\gamma\left(x,Q^2\right) = \frac{N_c\alpha}{2\pi} e_{q_i}^2 \left\{\left[x^2+(1-x)^2\right]\ln\frac{Q^2(1-x)}{m_{q_i}^2 x} + 8x(1-x) - 1\right\} \tag{5.30}$$

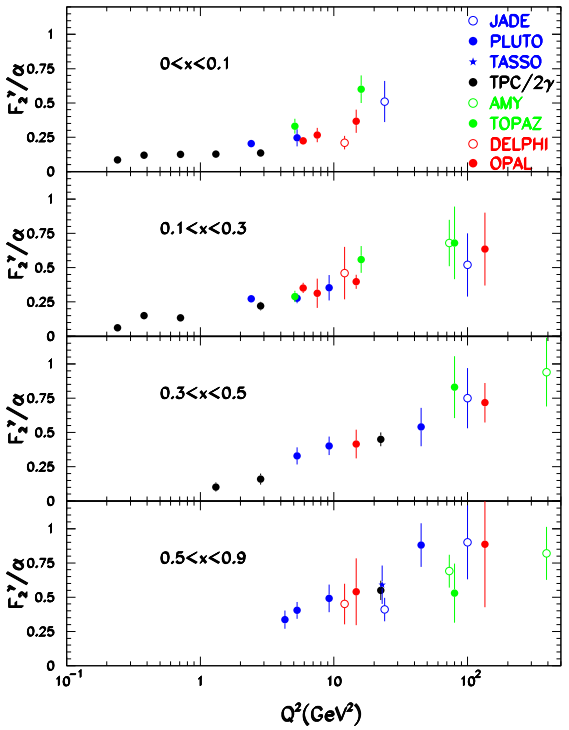

Figure 5.2: The photon structure function as function of Q^2 for different x intervals.

In spite of the complete analogy between the photon and the proton structure functions, there are important differences in their behaviour. In the QPM the proton structure function F_2^p is expected to fulfil Bjorken scaling, while F_2^γ manifests strong scaling violation even without the presence of gluon radiation. Thus, contrary to the character of scaling violation in the proton case, which yields a negative contribution at large x and a positive one at low x, the scaling violation for the photon is positive in the whole x region (already at the Born level). This can be seen in figure 5.2 where the photon structure function data are presented [14] as function of Q^2 for different x regions. The data show positive logarithmic scaling violation in all regions of x.

Another difference between the proton and photon case is the x dependence. Simple counting rules predict that F_2^p should drop at large x, while F_2^γ is large in the high x region (see below).

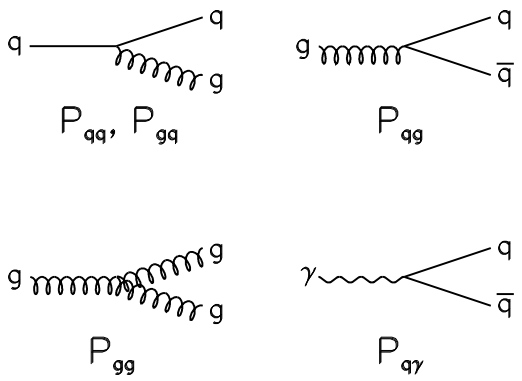

Figure 5.3: The splitting functions utilized in the DGLAP equations for the photon.

5.4 Evolution equations for the photon

The DGLAP evolution equations for the photon [96, 97, 98] can be developed in a similar way to that of the proton. However, there is one basic difference: in the photon case there is an additional contribution coming from the splitting of the photon into a $q\bar{q}$ pair, as can be seen in figure 5.3.

The splitting function of the photon is denoted by

$$h^{\text{box}} = N_c e_q^2 \frac{\alpha}{2\pi} \left[x^2 + (1-x)^2\right] \tag{5.31}$$

Defining the variable t as follows:

$$t \equiv \ln \frac{Q^2}{\Lambda^2} \tag{5.32}$$

we can write the DGLAP evolution equations for the photon:

$$\frac{\mathrm{d}q_i^\gamma(x,t)}{\mathrm{d}t} = h^{\text{box}} + \frac{\alpha_S(t)}{2\pi} \int_x^1 \frac{\mathrm{d}x'}{x'} \left\{ P_{qq}\left(\frac{x}{x'}\right) q^\gamma(x',t) + P_{gq}\left(\frac{x}{x'}\right) g^\gamma(x',t) \right\} \tag{5.33}$$

$$\frac{\mathrm{d}g^\gamma(x,t)}{\mathrm{d}t} = \frac{\alpha_S(t)}{2\pi} \int_x^1 \frac{\mathrm{d}x'}{x'} \left\{ \sum_{q_i} P_{q_i g}\left(\frac{x}{x'}\right) q_i^\gamma(x',t) + P_{gg}\left(\frac{x}{x'}\right) g^\gamma(x',t) \right\} \tag{5.34}$$

In the case of the QCD evolution equation for the photon structure function, the h_{box} term introduces an inhomogeneity into all parton densities in the photon. This is different

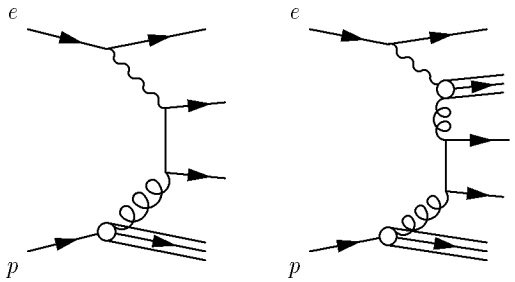

Figure 5.4: Diagrams representing direct and resolved photon interactions.

from the proton case, where all equations are homogeneous. The solution to the set of equations 5.33 and 5.34 is given by a superposition of the general solution to the corresponding set of homogeneous equations and a particular solution of the inhomogeneous one.

The inhomogeneous solution is determined by h^{box} and thus depends only on the known point–like (pl) coupling of the photon to the quarks and quarks to gluons. This is why it is identified with the point–like contribution to the photon structure function. Since the homogeneous solution fulfils the hadron–like (had) evolution of the DGLAP equations, it is assigned to the hadron–like contribution to the photon structure function. One writes therefore:

$$F_2^\gamma = F_2^{\gamma,\text{pl}} + F_2^{\gamma,\text{had}} \tag{5.35}$$

5.4.1 The resolved and direct photon interactions

This is perhaps the place to caution [99] the reader not to confuse between the point–like photon and the direct photon reactions. Whenever the interaction of a photon can be described as a two–step process in which the photon first resolves into partons and then one of the parton participates in the hard interaction, such a photon is called a resolved photon. The resolved photon includes both the point–like and the hadron–like part. In the other cases, when the photon interacts directly, all its energy participates in the hard interaction and we say that this is a direct photon interaction. Examples of diagrams describing the direct and resolved photon interactions are shown in figure 5.4.

This picture of resolved and direct photon was tested experimentally [100, 101] at HERA. One can define the quantity x_γ as the fraction of the photon momentum participating in the hard interaction. One expects then that for the direct photon processes $x_\gamma \sim 1$ while for the resolved ones $x_\gamma < 1$. A good way of estimating x_γ is to study two jet events. In this case one can calculate x_γ^{obs}, the experimentally observed quantity which is close to x_γ:

$$x_\gamma^{\text{obs}} = \frac{E_T^{j1} e^{-\eta^{j1}} + E_T^{j2} e^{-\eta^{j2}}}{2E_\gamma} \tag{5.36}$$

where E_T is the transverse energy of the jet, η its pseudorapidity and E_γ is the energy of

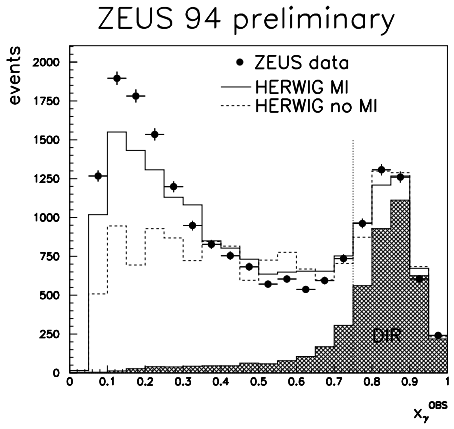

Figure 5.5: The x_γ distribution as obtained from two jet events, compared to direct and resolved photon interactions as simulated by Monte Carlo generators,

the photon. The variable $x_\gamma^{\rm obs}$ is plotted in figure 5.5. The data [102] show an enhancement at high x and a distribution reaching down to low x values, as one expects from a sample of events produced by direct and resolved photon interactions. The data are compared to the distributions obtained from the sum of Monte Carlo generated events simulating direct and resolved photon processes. The agreement is quite good in most of the regions, except for the very low x region, which needs to be further studied.

5.5 The theoretical importance of F_2^γ

As is known from the proton case, the hadron–like contribution varies very slowly with Q^2. Thus in the high Q^2 limit:

$$F_2^\gamma \to F_2^{\gamma,\rm pl} = a(x) \ln \frac{Q^2}{\Lambda^2} \tag{5.37}$$

In this equation $a(x)$ is calculable in pQCD and therefore one can predict [103] both the shape and the magnitude of F_2^γ, resulting in the ability to determine the QCD scale Λ. Unfortunately, owing to many theoretical difficulties encountered in the calculation of F_2^γ, one of which is discussed below, the actual attempts to measure Λ through the study of F_2^γ have attained only a very limited success.

5.5.1 Higher order corrections

We know from the proton case that in order to get reliable results, one needs to do at least a next to leading order calculation. What happens when one attempts to do it for the photon case? Can one continue this two component picture of a point–like and a hadron–like part of the photon structure function?

It would be too technical to develop here the next to leading log approximation. This is usually done by introducing the moments of the structure functions appearing in the evolution equation and by introducing the anomalous dimensions. We will just bring here the essence of such a calculation. The result is that when one continues to separate the structure function in a point–like and hadron–like part one gets:

$$F_2^{\gamma,\rm pl} < 0 \qquad \text{for } x \leq 0.1 \tag{5.38}$$

The situation gets worse with each order of calculation [104].

Since a structure function can not be negative, this means that the separation into a point–like and a hadron–like part gives unphysical results for the point–like part and thus the hadron–like part is needed in order to cancel the singularity. Since there is no way to calculate the hadron–like part in pQCD and it can not be neglected even at high Q^2, the absolute predictive power is lost.

5.6 The experimental extraction of F_2^γ

In principle, in order to measure F_2^γ one needs to measure the cross section as a function of Q^2 and x. Q^2 can be determined by measuring the tagged electron. This can be with an accuracy of $\Delta Q^2/Q^2 \sim 7-10\,\%$, depending on the energy and angular resolution of the detector.

In order to obtain x, one needs a good measurement of the total hadronic energy W, which together with Q^2 yield x according to 5.22. However, owing to finite resolution and limited acceptance of the detector, one measures $W_{\rm vis}$, the visible hadronic energy, which is usual smaller than W, as can be seen in figure 5.6.

One needs thus to unfold the true result from the visible measurement. This procedure needs a Monte Carlo program having a good simulation of the detector and a good description of the structure of the event. One can see [105] for instance in figure 5.6(b) the improvement of the correlation between $W_{\rm vis}$ and the true W when using a better generator. However the simulation depends also on the fragmentation model used to generate the final state particles, which usually has problems with the description of the energy flow in the forward direction. Thus even the generator which gives a better correlation as far as the true W is concerned, fails to describe the energy flow in the forward direction, as seen in figure 5.7. Clearly more work is needed in this direction.

In spite of the problems described above, the photon structure function has been measured in a wide range of Q^2 values. However, at present, the statistics is limited and also

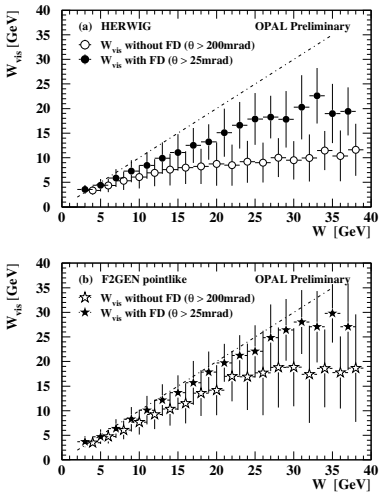

Figure 5.6: Comparison between the visible and the true W.

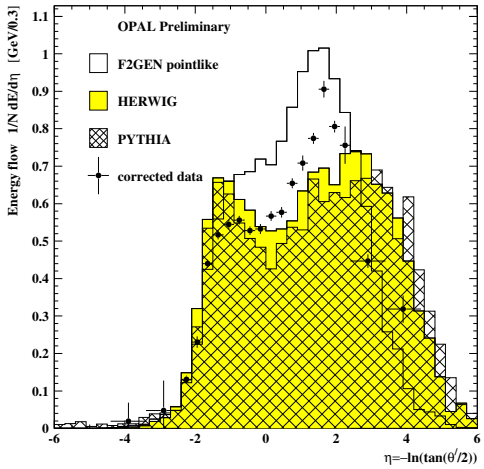

Figure 5.7: Comparison of the data on energy flow as function of the pseudorapidity with predictions of different Monte Carlo generators. The Q^2 values are in units of GeV^2.

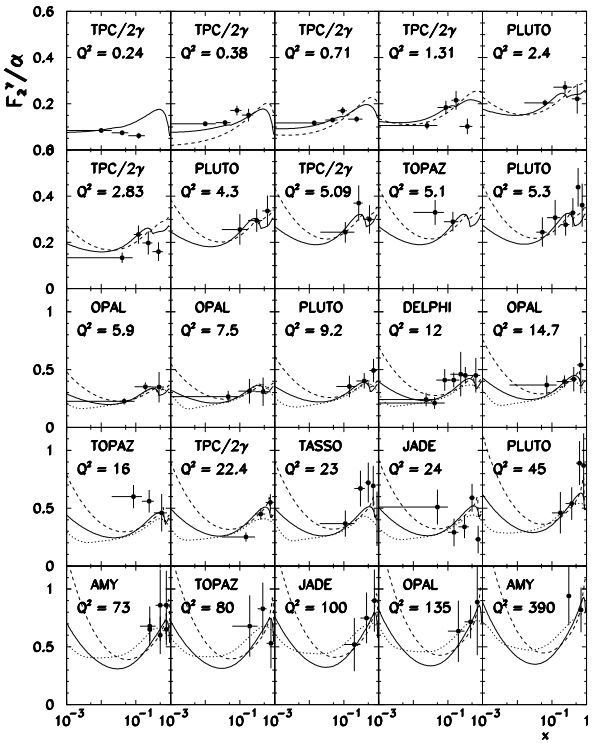

Figure 5.8: Compilation of all existing data on F_2^γ, compared to predictions of some parton parameterizations.

the systematic errors are quite large. This can be see in figure 5.8 where a compilation [14] of all existing measurements of F_2^γ is presented as a function of x, for different Q^2 values.

The curves are the predictions of some of the parameterizations [106, 107, 108] of the parton distributions in the photon, to be discussed below. Note that there are very few measurements in the low x region, due to the experimental difficulties to isolate the photon–photon reactions from the e^+e^- annihilation final state at high W.

5.7 Parton distribution in the photon

The parameterizations of the parton distributions in the photon are of two types. The one [109] uses the separation of the photon structure function into the point–like and

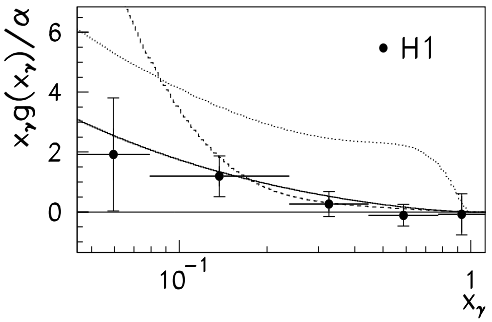

Figure 5.9: The estimated gluon density distribution in the photon, $x_\gamma g(x_\gamma)/\alpha$, compared to predictions of some parameterizations.

hadron–like parts to separate also the parton distribution functions the same way. They use for the point–like part either the ones calculated from QPM or from pQCD. The parameterizations of the hadron–like contribution are based mostly on the VDM approach, in which $F_2^{\gamma,\mathrm{had}}(x,Q^2)$ is related to the vector meson structure functions F_2^V. Through isospin invariance the different F_2^V are expressed in terms of the only experimental available mesonic structure function, that of the π^-, $F_2^{\pi^-}$, which is measured in Drell–Yan reactions.

In the second approach, no distinction is made between the point–like and hadron–like contributions to the structure function, and a parameterization, fixed at a given Q_0^2, is evolved to a different Q^2 through the DGLAP equations. The first to undertake this approach were Drees and Grassie (DG) [110]. They used the LLA modified DGLAP equations to evolve an input parameterization of parton distributions at $Q_0^2 = 1\,\mathrm{GeV}^2$ so that it fits the PLUTO data at $5.9\,\mathrm{GeV}^2$. This approach was extended later, using data in the range $1.3 < Q^2 < 100\,\mathrm{GeV}^2$ by Abramowicz, Charchula and Levy (LAC) [111], where the gluon parameters were also left free in the global fit. These LLA parameterizations have been extended to next to leading order, some of which are shown in figure 5.8. The different parameterizations obviously agree with each other where data exist, and differ in the low x region, where data are eagerly awaited.

One source of measurements of the photon parton distributions at low x is HERA. We have already seen in figure 5.5 the x_γ distribution obtained from two jet events. One can use the distributions obtained from the Monte Carlo generators to subtract the direct photon reactions from the x_γ distribution, being left with the resolved photon processes. Since the quark distribution in the photon is quite well constrained by the photon structure function measurements, one can use a parameterization prediction like that of GRV to subtract the quark distributions from the resolved x_γ distribution. The remaining events are attributed

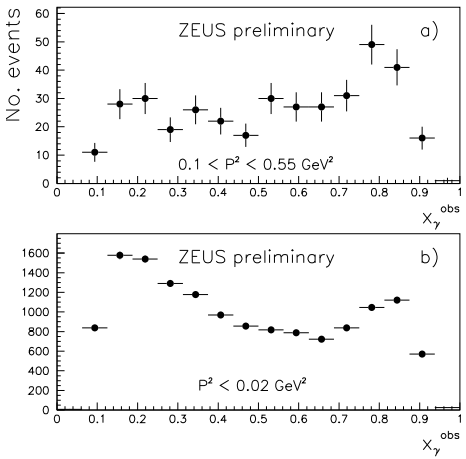

Figure 5.10: The x_γ^{obs} distribution (a) for photons of virtuality $0.1 < P^2 < 0.6\,\mathrm{GeV}^2$ and (b) for quasi–real photons.

to come from the gluons and thus obtain the gluon density distribution in the photon. The result [112] of such a procedure is shown in figure 5.9. The gluon density distribution obtained in this way does not seem to show a strong rise as x decreases, but one needs more precise data and procedures to conclude something more definite.

5.8 Parton distribution of a virtual photon

So far, we discussed the structure of real or quasi–real photons. The natural question that one is faced with is what happens to a virtual photon and whether it is legitimate to think that in DIS of charged leptons on protons it is indeed the structure of the proton that is probed and not some kind of convolution of both the structure of the target and of the probe [113]. The same question could be asked in the case of the deep inelastic $e\gamma$ scattering. We will return to this question in the last chapter.

There exists one result by PLUTO [114] from 1984 which measured the structure function of a target photon with virtuality of $P^2 \approx 0.4\,\mathrm{GeV}^2$, at $Q^2 \approx 5\,\mathrm{GeV}^2$. There is also an attempt [115] at HERA to measure the structure of a virtual photon. The electron calorimeter of the luminosity system taggs photons with a median virtuality of $P^2 \approx 10^{-5}\,\mathrm{GeV}^2$. There is another calorimeter, the beam–pipe calorimeter, which taggs photons in the range $0.1 < P^2 < 0.6\,\mathrm{GeV}^2$. By using these two taggers, one can isolate two jet events from

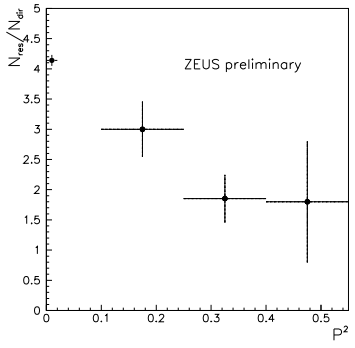

Figure 5.11: The ratio of resolved to direct photon reactions as a function of the photon virtuality P^2.

quasi–real photons, and a similar sample from the virtual photon reactions. One can then reconstruct the $x_\gamma^{\rm obs}$ of the photon by using relation 5.36. The distribution of the two samples are shown [115] in figure 5.10. For real photons one sees the concentration of direct events at high $x_\gamma^{\rm obs}$, and the low x enhancement coming from the resolved photon processes. For the higher P^2 region, one sees again the peak at high x from direct events, but also a contribution from the resolved photons at lower x. This shows that photons with virtualities in the range $0.1 < P^2 < 0.6\,{\rm GeV}^2$ also have structure.

One can use an operational definition of direct photon reactions by the cut $x_\gamma^{\rm obs} > 0.75$ and study the ratio of resolved photon to direct photon as function of the photon virtuality P^2. This is shown in figure 5.11, which seems to show a decrease of this ratio with increasing P^2, as expected. These data are preliminary and not yet corrected for acceptance effects, which are believed to cancel in the ratio. Further study of this interesting question with more data and to higher P^2 values is in process.

5.9 Summary

In this chapter we studied the following subjects about the photon:

- We have introduced the concept of a photon with structure, where the structure is attained by the long fluctuation time of the photon into a $q\bar{q}$ pair before it interacts with the proton. Clearly the whole notion of the structure of the photon makes only sense when we view its interaction with another object.

- We developed the formalism of two photon reactions in e^+e^- collisions and related the process $e\gamma \to eX$ with that of $ee \to eeX$.

- We defined the photon structure function through its analogy to the proton structure function, defined the parton distribution functions in the photon and discussed the DGLAP evolution equation of the photon. These equations are inhomogeneous because of the splitting of a photon to a $q\bar{q}$ pair in addition to the splitting functions in the proton case.

- The point–like and the hadron–like parts of the photon structure functions have been described. Both parts are what is contained in the so–called resolved photon. In the direct photon processes the photon interacts directly with parton from the other projectile, while the resolved photon reactions are a two–step process in which the photon first resolves into its partons, one of which takes part in the hard interaction.

- The theoretical importance of F_2^γ was described as a potential source of determining the QCD scale parameter Λ. However due to problems in the low x region when one uses next to leading order corrections, this is not possible.

- We discussed the experimental procedure of obtaining F_2^γ from the data and the difficulties involved. At present both the statistical errors and the systematic ones are quite large. There is also very little data in the low x region. That is the reason why the different parameterizations of the parton distributions in the photon differ quite widely in the low x region.

- Finally, we discussed the question whether virtual photons also have structure. Preliminary data indicate that at least up to a virtuality of about $P^2 \approx 0.6\,{\rm GeV}^2$, the photon seems to have structure.

Chapter 6

Diffraction in DIS

The notion of diffraction in high energy physics is not easy to define. The dictionary defines it as 'the breaking up of a light beam into light and dark or coloured bands by passing it through a small opening'. We will describe what are the expected behaviour of a diffractive reaction in the introductory section after which we will make the connection to Regge theory and to the Pomeron which is the dominant trajectory exchanged in diffractive processes. Next we will discuss the different diffractive reactions in photoproduction ($Q^2 = 0$) and the discovery of the large rapidity gap events in DIS. The interpretation of these inclusive reactions as DIS on the Pomeron is presented and the partonic structure of the Pomeron is discussed.

6.1 General introduction

The best example of a diffractive reaction is the process of elastic scattering $A+B \to A+B$ in which no quantum numbers are exchanged in the t channel. In the Regge language one the exchanged trajectory which has the quantum numbers of the vacuum the Pomeron trajectory. Thus one usually calls a process diffractive if its t channel amplitudes at high energies are determined by Pomeron exchanges. A diffractive process [28] has a total cross section practically independent of energy, a small real part of the forward scattering amplitude, and a forward peak in the differential cross section. Among other characteristics is the predominant conservation of s channel helicities of the scattered particles (to be discussed later). A non–diffractive process corresponds to exchanges with non–vacuum quantum numbers in the t channel and has a cross section decreasing with energy.

In addition to the elastic scattering, one can have inelastic diffractive processes. These include the single diffraction (SD) and the double diffraction (DD) reactions in which the beam and/or the target particles get excited into states with the same internal quantum

numbers as those of the incoming particles.

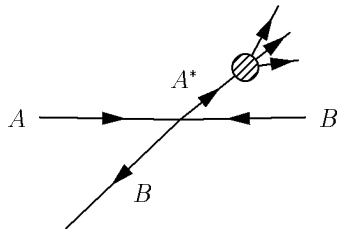

single diffraction (SD) (6.1)

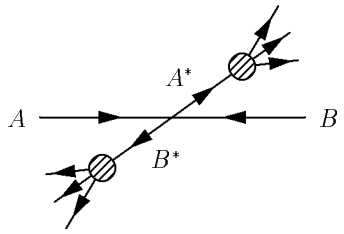

double diffraction (DD)

Some examples of inelastic diffractive processes are: $\pi^- p \to \pi^- N^*$ (SD), $\pi^- p \to a_1^- p$ (SD), $\pi^- p \to a_1^- N^*$ (DD).

In general, a diffractive reaction of the type $A + B \to X + B$ has in addition to all the above mentioned characteristic behaviours, a cross section which falls with the mass of X like:

$$\frac{\mathrm{d}\sigma}{\mathrm{d}t\mathrm{d}M_X^2} \sim \frac{1}{M_X^2} \tag{6.2}$$

In such a diffraction reaction, B is a leading energetic particle such that $E_B \approx p_L$. In this case one has:

$$M_X^2 = (P - p_B)^2 = s + m_B^2 - 2E_B\sqrt{s} \approx s - 2p_L\sqrt{s} = (1 - \frac{s - 2p_L}{\sqrt{s}})s = (1 - x_F)s \tag{6.3}$$

where x_F is the Feynman x. Usually for diffractive reaction $x_F \geq 0.9$ which means $\frac{M_X^2}{s} \leq 0.1$. One can get this limit using a geometrical argument. The coherence is important for building up the forward peak and thus:

$$\frac{M_X^2}{s} \leq \frac{1}{2m_A R} \tag{6.4}$$

Since the radius R is of the order of $\sim 1\,\mathrm{fm} = 5\,\mathrm{GeV}^{-1}$, one gets the condition $\frac{M_X^2}{s} \leq 0.1$.

6.2 Diffraction and regge formalism

The Regge domain is defined as that where t is small and $\frac{s}{M_X^2} \to \infty$. In this case one can write the total, elastic and inelastic diffraction cross sections in the form:

$$\sigma_T^{ij} = \sum_k \beta_{ik}(0)\beta_{jk}(0) s^{[\alpha_k(0)-1]} \tag{6.5}$$

$$\frac{\mathrm{d}\sigma_{el}^{ij}}{\mathrm{d}t} = \sum_k \frac{\beta_{ik}^2(t)\beta_{jk}^2(t)}{16\pi} s^{2[\alpha_k(0)-1]} \tag{6.6}$$

$$\frac{\mathrm{d}^2\sigma^{ij}}{\mathrm{d}t\mathrm{d}M_X^2} = \sum_{k,l} \frac{\beta_{ik}(0)\beta_{jl}^2(t)\, g_{kll}(t)}{16\pi s} \left(\frac{s}{M_X^2}\right)^{2\alpha_l(t)} \left(M_X^2\right)^{\alpha_k(0)} \tag{6.7}$$

where the functions β and g are vertex functions and α is the Regge trajectory.

This can be illustrated with the following diagrams:

$\sigma_T^{ij} =$ 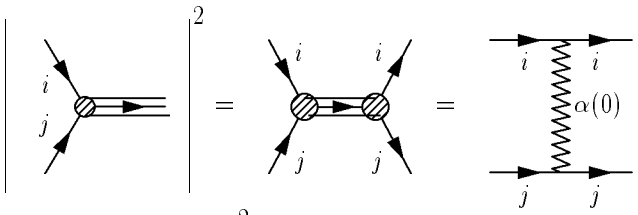

(6.8)

$\frac{\mathrm{d}\sigma_{el}^{ij}}{\mathrm{d}t} =$ 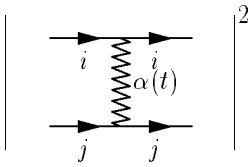

(6.9)

$\frac{\mathrm{d}^2\sigma^{ij}}{\mathrm{d}t\mathrm{d}M_X^2} =$ 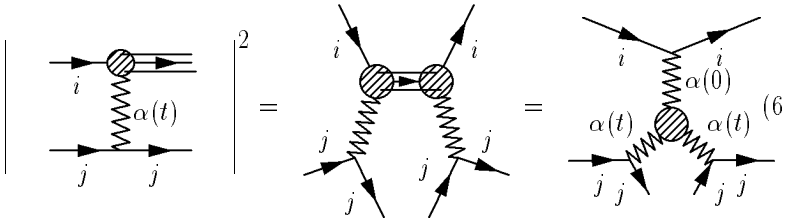

(6.10)

The Pomeron trajectory is the one dominating the diffraction processes. In order to describe the properties of diffraction, its trajectory has the form:

$$\alpha_{I\!P}(t) = \alpha_{I\!P}(0) + \alpha'_{I\!P}(t)t \approx 1 + \alpha' t \tag{6.11}$$

where for the present discussion we have assumed the Pomeron intercept to be 1 (taking $\epsilon = 0$).

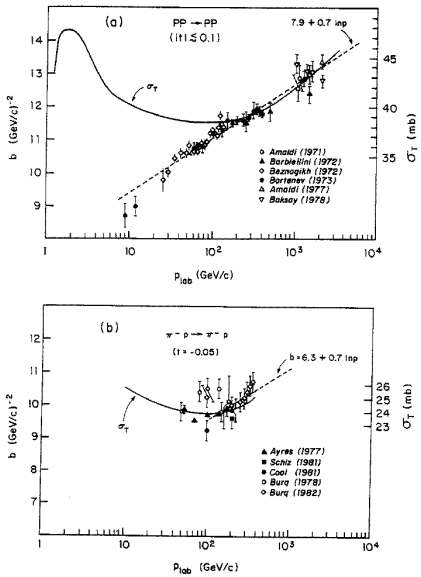

Figure 6.1: The dependence of the slope b on the laboratory momentum of the incoming projectile for (a) pp elastic scattering and for (b) $\pi^- p$ elastic scattering. On the right–hand side of the vertical axis the scale is the total cross section σ_T for (a) pp and (b) $\pi^- p$ reaction. The corresponding data are approximated by the solid line.

- The total cross section can be expressed as:

$$\sigma_T^{ij} = \beta_{i\,I\!P}(0)\beta_{j\,I\!P}(0) = \text{const} \tag{6.12}$$

  If one uses an intercept of $1+\epsilon$, one gets a slowly rising cross section like s^ϵ.

- The elastic differential cross section is:

$$\frac{\mathrm{d}\sigma_{el}^{ij}}{\mathrm{d}t} = \frac{\beta_{i\,I\!P}^2(t)\beta_{j\,I\!P}^2(t)}{16\pi M_X^2} s^{\alpha' t} \tag{6.13}$$

  If one has a Pomeron intercept somewhat larger than 1, one has an additional factor of $s^{2\epsilon}$.

  For small t one gets for the differential cross section of elastic scattering the sharp diffractive peak:

$$\frac{\mathrm{d}\sigma_{el}^{ij}}{\mathrm{d}t} \approx \frac{\sigma_T^2}{16\pi} e^{b(s,t)t} \tag{6.14}$$

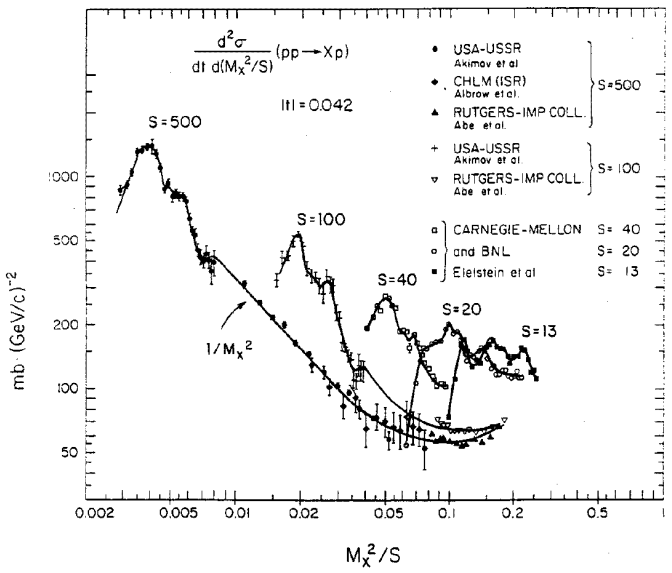

Figure 6.2: The differential cross section for the inelastic diffractive reaction $pp \to Xp$ as function of the scaled diffractive mass M_X^2/s.

where the slope of the exponential behaviour increases with energy like:

$$b(s,t) = b_0(t) + 2\alpha' \ln s \tag{6.15}$$

We have assumed that the scale in the logarithmic expression is $s_0 = 1\,\mathrm{GeV}^2$. The slope [30] of the Pomeron trajectory is $\alpha' \approx 0.25\,\mathrm{GeV}^{-2}$. The phenomena of the increase of the slope with energy is called shrinkage. The shrinkage can be seen in figure 6.1 for (a) pp elastic scattering and for (b) $\pi^- p$ elastic scattering. One observes in both cases a rise of the slope with energy, as expected from expression 6.15. The same figure also shows the behaviour of the total pp and $\pi^- p$ cross sections, showing the slow increase with energy discussed in the former item.

- The differential cross section of inelastic single diffraction is given by [116, 117]:

$$\frac{\mathrm{d}^2\sigma^{ij}(s, M_X^2, t)}{\mathrm{d}t\mathrm{d}M_X^2} = \frac{\beta_{i\mathbb{P}}(0)\beta_{j\mathbb{P}}^2(t) g_{\mathbb{P}\mathbb{P}\mathbb{P}}(t)}{16\pi M_X^2} \left(\frac{s}{M_X^2}\right)^{2\alpha' t} \tag{6.16}$$

For small t we can make the same approximation as in the elastic case to obtain:

$$\frac{\mathrm{d}^2\sigma^{ij}(s, M_X^2, t)}{\mathrm{d}t\mathrm{d}M_X^2} \approx \frac{A}{M_X^2} e^{b_D(s,t)t} \tag{6.17}$$

This behaviour can be seen for the differential cross section of the inelastic diffractive reaction $pp \to Xp$ shown in figure 6.2 for different s values. As s increases and one reaches the Regge domain, one sees a clear $1/M_X^2$ behaviour of the cross section. Here too the slope increases with energy like:

$$b_D(s,t) = b_{D,0}(t) + 2\alpha' \ln \frac{s}{M_X^2} \tag{6.18}$$

All hadronic reactions show an appreciable contribution of diffractive processes to the total cross section ($\sim$ 25–40 %), including double dissociation. Is this true also for photoproduction? Can one check it at HERA?

6.3 Diffraction in photoproduction at HERA

What does one understand by diffractive processes in photoproduction? First one has the elastic scattering. In case of photoproduction the true elastic scattering process is $\gamma p \to \gamma p$. However this is an electromagnetic process. The hadronic elastic scattering in photoproduction is referred to the reaction $\gamma p \to V^0 p$, where V^0 are the neutral vector mesons. In the VDM picture this process is a two stage one. The photon first fluctuates into a virtual vector meson, which then scatters elastically from the target proton. With this in mind, the following processes contribute to diffractive photoproduction reactions:

"elastic"	:	$\gamma p \to Vp$	$(V = \rho^0, \omega, \phi)$ (not $\gamma p \to \gamma p$)
photon diffraction	:	$\gamma p \to Xp$	$(X \neq \rho^0, \omega, \phi)$
proton diffraction	:	$\gamma p \to VY$	$(Y \equiv$ 'excited' proton)
double dissociation	:	$\gamma p \to XY$	

This can also be illustrated in a VDM picture:

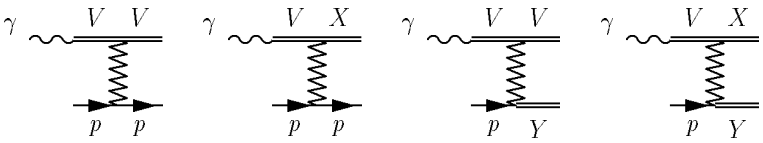

(6.19)

We have already seen how one measures photoproduction reactions at HERA in chapter 2. Is it possible to distinguish [118] diffractive from non–diffractive precesses in these reactions? In order to be able to do so, one needs a large rapidity phase space. How large is it at HERA?

Let us consider the reaction:

$$\gamma p \to Xp \tag{6.20}$$

In the γp center of mass system:

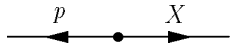

(6.21)

In this system the maximum center of mass momentum is:

$$p_{\max}^{\mathrm{cms}} \simeq \frac{\sqrt{s}}{2} = \frac{W}{2} = p^* \tag{6.22}$$

The maximum rapidity of X is $y_{\max}^{\mathrm{cms}}$ where the positive direction is taken as that of the proton:

$$y_{\max}^{\mathrm{cms}} = \frac{1}{2}\ln\frac{E+p^*}{E-p^*} = -\frac{1}{2}\ln\frac{(E+p^*)^2}{E^2-p^{*2}} \simeq -\frac{1}{2}\ln\frac{W^2}{M_X^2} \tag{6.23}$$

Therefore the rapidity of the diffractive system X and the diffractive proton can be given by:

$$y_X = -\frac{1}{2}\ln\frac{W^2}{M_X^2} + \text{boost to any system} \tag{6.24}$$

$$y_p = \frac{1}{2}\ln\frac{W^2}{M_p^2} + \text{boost to any system} \tag{6.25}$$

The rapidity span Δy is therefore:

$$\Delta y = \frac{1}{2}\ln\frac{W^2}{M_X^2} + \frac{1}{2}\ln\frac{W^2}{M_p^2} = \frac{1}{2}\left[\ln\frac{W^4}{M_X^2 m_p^2}\right] = \ln\frac{W^2}{M_X m_p} \tag{6.26}$$

For $M_X \simeq 10\,\mathrm{GeV}$ and $W = 200\,\mathrm{GeV}$ the rapidity range is $\Delta y = 8.4$. In the experimental analysis one uses the pseudorapidity which is defined as:

$$\eta = -\ln\tan\frac{\Theta}{2} \tag{6.27}$$

In fig. 6.3 the rapidity distribution of the different photoproduction processes at HERA are shown [119, 120] together with the regions covered by the ZEUS detector. As one can see, much of the phase space is lost in the beam pipe. The detector covers only the rapidity range between -3.4 and $+3.8$.

Thus, in order to measure the total cross section one needs to correct for these losses. This requires the knowledge of the relative contribution of the different processes contributing to the total cross section. Since one can not measure them directly, one has to find variables whose distribution is sensitive to the different processes and fit the distributions

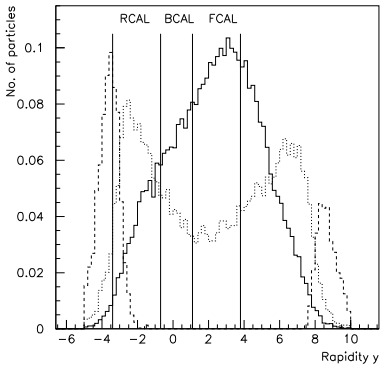

Figure 6.3: The rapidity distribution of the different photoproduction processes at HERA. The regions covered by the ZEUS detector are indicated.

to the combinations of cross sections which best describe the data. The H1 collaboration [121] used the variables $\eta_{\max}$ and $\eta_{\min}$ to determine the cross section of the different processes. The variable $\eta_{\max}$ ($\eta_{\min}$) is defined as the maximum (minimum) pseudo rapidity of all reconstructed charged tracks and all clusters in the calorimeter with energy larger than 400 MeV. The results of the H1 measurement, assuming that the DD cross section is in the range $0 < \sigma_{DD} < 40\,\mu$b, are shown in table 6.1

The total cross section is in good agreement with earlier measurements and with predictions of Regge motivated models [31, 18], as can be seen from figure 6.4.

Table 6.1: Cross–section for the different diffractive contributions at $W = 200$ GeV.

process	cross section (μb)
$\sigma(\gamma p \to Vp)$	17.1 ± 4.3
$\sigma(\gamma p \to Xp)$	23.4 ± 11.3
$\sigma(\gamma p \to VY)$	8.7 ± 3.6
$\sigma(\gamma p \to XY)$	20 ± 20
diffractive (el + SD + DD)	69.2 ± 13.3
non–diffractive	96.1 ± 17.9
total	165.3 ± 11.2

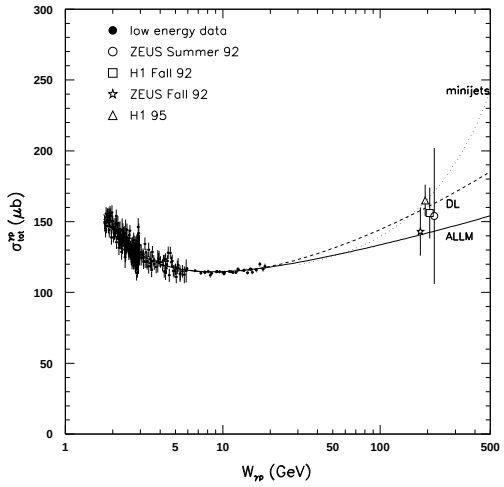

Figure 6.4: The total photoproduction cross section measurements at HERA and at lower energies, compared to different models.

6.3.1 Ratios of cross sections

It is of interest to compare [59] the relative abundance of processes in γp with those in other hadronic reactions. To this end we present in figure 6.5(a) the ratio of the elastic to total cross section for $\bar{p}p$, πp, Kp and γp reactions. As expected, the ratio for $\bar{p}p$ is larger than for the πp and the Kp case. The γp ratio, though having large errors, is closer to the meson initiated reactions, in accordance with VDM expectations. It is however a bit on the low side, since at the HERA energies one would expect this ratio to be somewhat larger than the measured ones.

In figure 6.5(b) the ratio of single diffraction to total cross section is presented for $\bar{p}p$ and γp. The ratios for γp are somewhat larger than what one would naively expect from VDM. The slight deficiency of the elastic ratio and the access in the single diffraction case may be correlated and might be due to the way the processes are defined in photoproduction. The traditional definition of the elastic photoproduction reaction includes only the first three lightest vector mesons ρ^0, ω and ϕ. Higher vector mesons are included in the single diffraction channel. In view of the slight deviations of the photoproduction results from the expectations, one might have to redefine the exact meaning of elastic and single diffraction in photoproduction.

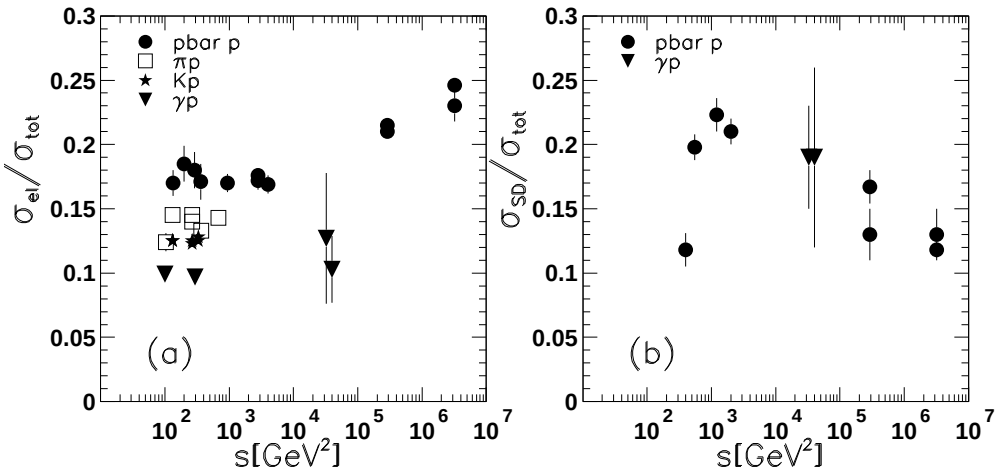

Figure 6.5: The contribution of the (a) elastic and (b) single diffraction processes relative to the total cross section for hadron–proton and γ–proton interactions.

6.4 Large rapidity gap events in DIS

The diffraction of the real photon can be clearly understood following the discussion presented in chapter 5, where a real photon can fluctuate into a $\bar{q}q$ pair and acquire a hadronic structure before interacting with the proton and thus producing in some of the time a diffractive process. Due to the shorter fluctuation time expected for the virtual photon case, it should behave like a point–like structureless object which does not diffract.

It thus came as a big surprise when events of the kind presented in figure 6.6 were discovered [20, 21] in DIS NC processes. These events had a large rapidity gap between the proton direction and the first observable particle produced in the collision. None of the Monte Carlo generators written for the HERA region could predict the frequency of these events, as was shown earlier in figure 1.10.

Are these large rapidity gap indeed diffractive? Why did one not expect earlier to see large rapidity gaps near the proton direction? In a DIS reaction the virtual photon hits one parton of the proton and produces what one calls the current jet. However due to the large colour forces the region between the current jet and the proton remnant is filled with radiated gluon and thus if one looks for instance at the energy flow [122, 123] as function of the pseudo rapidity, the forward region, which is the proton direction, is also filled with energy deposition in a regular DIS event. This can be seen in figure 6.7 where the energy

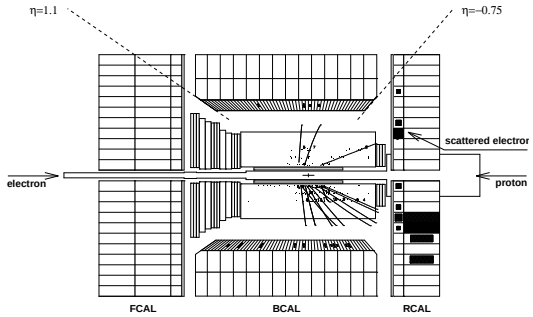

Figure 6.6: A DIS NC event in the ZEUS detector which has a large rapidity gap between the outgoing proton and the other produced particles in the ep collision.

flow is presented [122] for different x, Q^2 regions. The open data points are DIS events.

When however the virtual photon interacts with a colour singlet object, as would be the case in a diffractive process, the gluon radiation in the region between the current jet and the proton remnant is strongly suppressed and thus there should be no energy flow in the forward region. This is seen from the distribution of the full data points in figure 6.7, which have been selected as those events having $\eta_{\max} < 1.8$, meaning large rapidity gap events.

How can one be sure that these large rapidity gap events are due to a colour singlet object which is exchanged in diffractive reactions and not for instance due to the exchange of a pion, which is also a colour singlet object? One of the expected features of diffractive processes is a very slow energy dependence. Indeed the large rapidity gap events show this feature. In figure 6.8 one sees [124] on the right hand side the ratio of the large rapidity gap events to the inclusive DIS events as a function of Bjorken–x for constant Q^2 regions, which is equivalent of plotting the ratio as function of the $\gamma^* p$ cms energy squared W^2. Indeed the ratio is very slowly changing with energy and seems to have roughly the same value in all the four Q^2 regions.

Another feature of the large rapidity gap events was that their M_X dependence was consistent with that expected from a diffractive process.

One could actually have anticipated the presence of diffraction in DIS, using the following argument. At high energies or equivalently in the low x region studied at HERA, the fluctuation time of the virtual photon into a state of mass $m_{\bar{q}q} \approx Q^2$ is [125]:

$$t_f \approx \frac{1}{2m_p x} \tag{6.28}$$

where m_p is the proton mass. Thus in the HERA regime, a photon of virtuality as high as $Q^2 \sim 2 - 3 \times 10^3\,\mathrm{GeV}^2$ can fluctuate into a $\bar{q}q$ pair, which will survive till arrival on

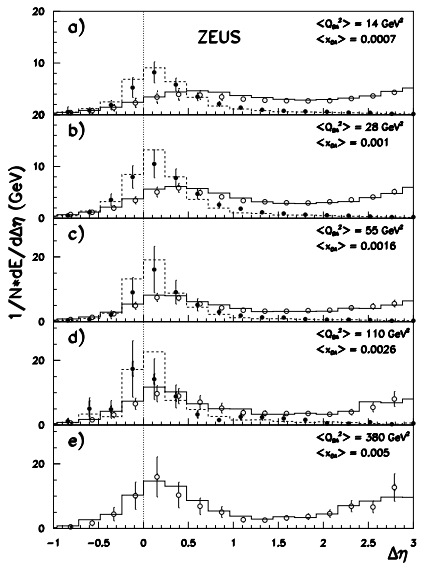

Figure 6.7: The energy flow of DIS events without a large rapidity gap (open dots) and those with a large rapidity gap ($\eta_{\max} < 1.8$, full dots), for different x, Q^2 bins.

the proton target. Therefore even highly virtual photons can produce diffractive processes which will look very similar to those in the real photon case.

Thus the large rapidity gap events have all the features expected from events produced in a diffractive process and one can interpret the interaction as that of a virtual photon interacting with a Pomeron, as described in the following diagram:

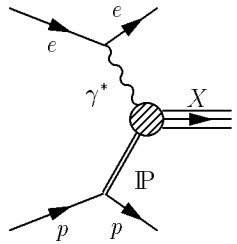

(6.29)

This diagram resembles that of the $\gamma^*\gamma$ case, discussed in the earlier chapter and which

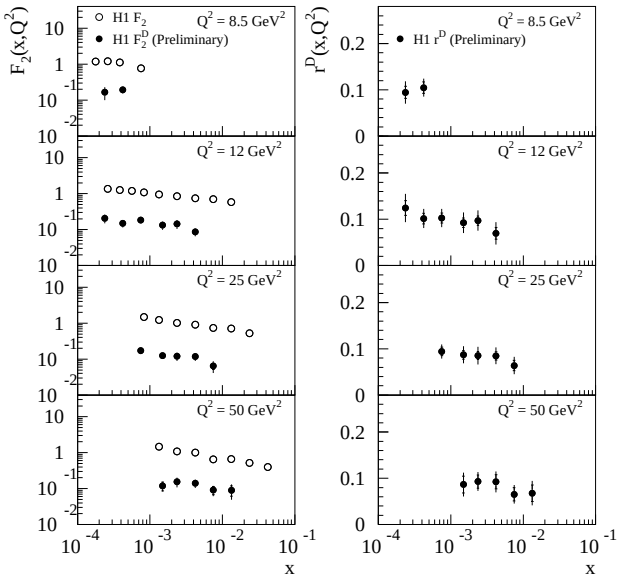

Figure 6.8: The F_2 structure function for the inclusive DIS sample (open circles) and for the large rapidity gap events (full dots) as function of Bjorken–x, for fixed Q^2 intervals. On the right hand side of the figure, their ratio is plotted as function of x for the same Q^2 intervals.

allowed to study the structure of the photon. Can we use this picture to learn about the structure of the Pomeron? Does the Pomeron have substructure?

6.5 DIS on the Pomeron

The first indication that the Pomeron might have a partonic substructure was reported by the UA8 experiment [126, 127]. Figure 6.9 presents the x of two–jet events in diffractive proton dissociation and shows that an unexpected large fraction of the Pomeron's momentum participates in the hard scattering.

At HERA [128, 129] one can also see events with jets. In figure 6.10(a) one can see an example of a DIS NC one–jet event which has a large rapidity gap. An example of a two–jet event with large rapidity gap is seen in figure 6.10(b).

In order to see whether these jets come from a hard scattering, one looks at the distribution of the transverse energy, which is shown in figure 6.11.

The observation of high E_T jets in the $\gamma^* p$ system for the large rapidity gap events

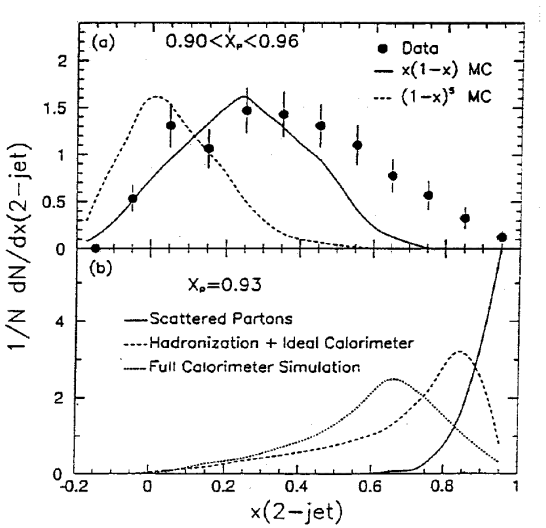

Figure 6.9: The x of two–jet events in diffractive proton dissociation in the UA8 experiment.

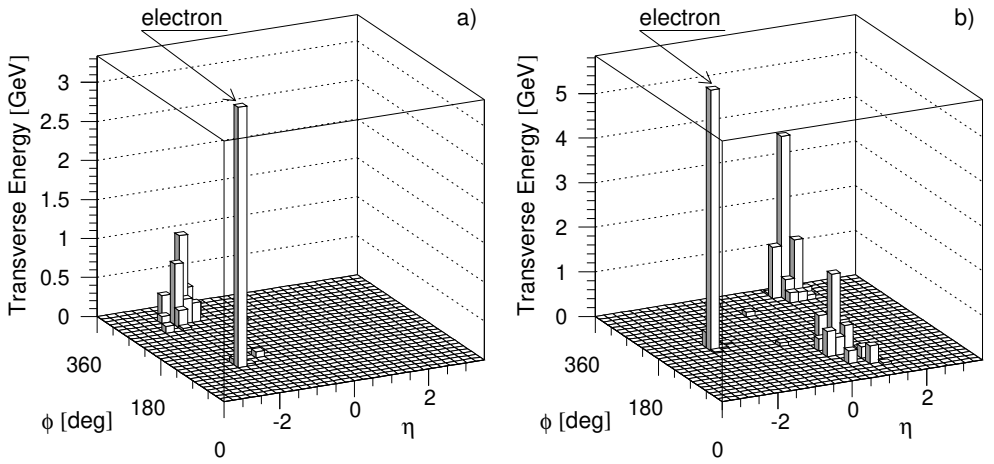

Figure 6.10: (a) Transverse energy deposition in η–ϕ space for a large rapidity gap event with one hadronic jet balancing the electron's transverse momentum. (b) A similar display for a large rapidity gap two–jet event.

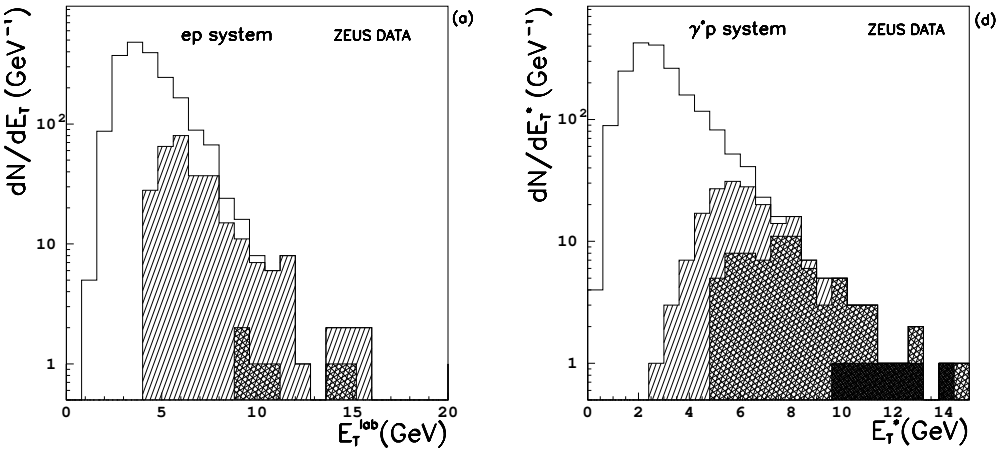

Figure 6.11: The distribution of the total hadronic transverse energy seen in the calorimeter E_T, for DIS events with a large rapidity gap and those with, in addition, ≥ 1 (hashed) and ≥ 2 jets (cross-hashed). On the left hand side, the quantity in the ep frame is presented while on the right hand side, in the $\gamma^* p$ frame.

where there is a noted absence of colour flow, indicate that a natural interpretation is the interaction of the virtual photon with partons in a colourless object inside the proton, believed to be the Pomeron.

6.5.1 Kinematical variables

When describing the inclusive cross section of a DIS event one usually uses the two variables x and Q^2. In the diffractive process shown in figure 6.12 one uses additional variables. One has the four momentum transfer squared at the proton vertex t defined as:

$$t = (P - P')^2 \tag{6.30}$$

The fraction of the proton momentum carried by the Pomeron is defined as:

$$x_{I\!P} = \frac{(P - P')q}{pq} \simeq \frac{M_X^2 + Q^2}{W^2 + Q^2} \tag{6.31}$$

Another variable is β, which is the momentum fraction of the struck quark within the Pomeron:

$$\beta = \frac{x}{x_{I\!P}} = \frac{Q^2}{M_X^2 + Q^2} \tag{6.32}$$

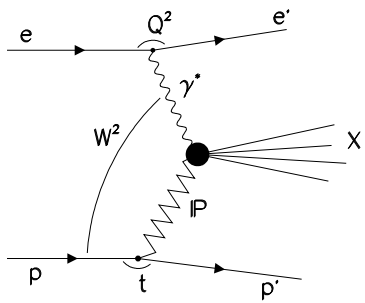

Figure 6.12: Diagram of a diffractive event.

6.5.2 The diffractive structure function

With these kinematical variables one can define the diffractive structure function in a similar way to that of the inclusive DIS structure function, through the differential cross section. In order to do so we shall use the following four variables: β, Q^2, $x_{I\!P}$ and t.

$$\frac{\mathrm{d}^4\sigma_{\mathrm{diff}}}{\mathrm{d}\beta \mathrm{d}Q^2 \mathrm{d}x_{I\!P}\,\mathrm{d}t} = \frac{2\pi\alpha^2}{\beta Q^4}\left[\left(1 + (1-y)^2\right) F_2^{D(4)} - y^2 F_L^{D(4)}\right](1+\delta_Z)(1+\delta_r) \tag{6.33}$$

where α is the electromagnetic coupling constant and the δ_i denote corrections due to Z^0 exchange and due to radiative corrections which are small in the measured range. The contribution of F_L to the diffractive cross section is not known but by restricting the measured y range to small values it can be neglected.

When t is not measured, an integration over t is performed and one determines $F_2^{D(3)}$ through the relation:

$$\frac{\mathrm{d}^3\sigma}{\mathrm{d}\beta \mathrm{d}Q^2 \mathrm{d}x_{I\!P}} \simeq \frac{2\pi\alpha^2}{\beta Q^4}[1 + (1-y)^2] F_2^{D(3)}(\beta, Q^2, x_{I\!P}) \tag{6.34}$$

where one neglects the effect of F_L and the additional contributions noted above.

6.5.3 Factorization and the Pomeron structure function

The diffractive structure function defined above is describing the inclusive ep diffractive process. We can now go one step further and interpret the diffractive structure function as consisting of two parts. One in which a flux of Pomerons are emitted from the proton and another part due to the Pomeron structure function. This is reminiscent of the procedure taken when discussing the photon structure function. In order to do so, one has to assume

that the Pomeron can be treated like a particle and abides to the factorization hypothesis. If so, we can define the Pomeron structure function in the following way:

$$F_2^{D(3)}(\beta, Q^2, x_{\mathbb{P}}) = f(x_{\mathbb{P}}) F_2^{\mathbb{P}}(\beta, Q^2) \tag{6.35}$$

where $f(x_{\mathbb{P}})$ is the function describing the flux of the Pomerons emitted from the proton. According to the Regge model the flux $f(x_{\mathbb{P}})$ should have an $x_{\mathbb{P}}$ dependence like:

$$f(x_{\mathbb{P}}) \sim \frac{1}{x_{\mathbb{P}}^n} \tag{6.36}$$

The exponent n is connected to the Pomeron trajectory through the relation:

$$n = 2\alpha_{\mathbb{P}}(t) - 1 \tag{6.37}$$

Since at present t is not measured, the exponent n gives a t–averaged slope of the Pomeron through relation 6.37. One can get the Pomeron intercept by assuming a diffractive slope and the slope of the Pomeron trajectory.

In order to check the factorization hypothesis, the diffractive structure function $F_2^{D(3)}$ is measured as function of $x_{\mathbb{P}}$ for fixed β and Q^2 intervals. If factorization holds, there should be one universal curve describing all data, up to a normalization factor. This is shown [124] in figure 6.13, where indeed one sees that in the range of variables presented in this figure the factorization hypothesis seems to be borne out by the data. The slope of the $x_{\mathbb{P}}$ dependence obtained by the H1 collaboration [124] is $n = 1.19 \pm 0.06(\text{stat}) \pm 0.07(\text{syst})$. The ZEUS collaboration [130] finds a slope of $n = 1.30 \pm 0.08(\text{stat}) \,^{+0.08}_{-0.14}(\text{syst})$. We will return to these results later.

6.5.4 The partonic structure of the Pomeron

In an Ingelman–Schlein [131] type of model the Pomeron consists of partons like a regular particle. How can one get information about the quark and gluon contents of the Pomeron? We will discuss three methods to probe the partonic content of the Pomeron.

Assuming the momentum sum rule

If the Pomeron behaves like a regular particle which fulfills the momentum sum rule, one can use the flux normalization, either that of Donnachie and Landshoff [132, 133] or that of Ingelman and Schlein [131], and assume that the Pomeron consists only of quarks. In that case the quarks saturate all the momentum of the Pomeron. The predictions of this assumption can be seen [130] as the lines in figure 6.14, while the data are presented as dots.

Note that non–diffractive background, as well as a 15 % estimate of double dissociation has been subtracted from the data. As one sees, the data lies below the predictions indicating that the quarks carry only part of the momentum of the Pomeron. The amount depends on the expression used for the normalization of the flux.

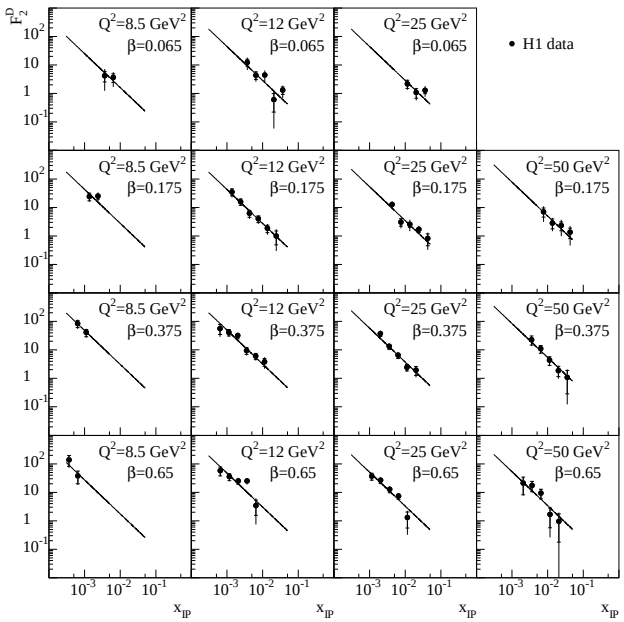

Figure 6.13: The diffractive structure function $F_2^{D(3)}$ as a function of $x_{\mathbb{P}}$ for fixed β and Q^2 intervals.

Diffractive hard photoproduction

One can get information about the partonic content of the Pomeron by studying [134] inclusive jet cross sections for events with large rapidity gaps with respect to the proton direction from the reaction $ep \to \text{jet} + X$ with no detected electron in the final state, thus classified as photoproduction.

When one compares the measured cross sections with pQCD calculations of diffractive hard processes, as done in figure 6.15, one may conclude that the Pomeron consists of a large fraction of hard gluons. This conclusion is model dependent. However, if one combines the photoproduction measurement with the results on the diffractive structure function in deep inelastic scattering, discussed above, one finds experimental evidence for the gluon content of the Pomeron. One fits the photoproduction cross section to the expression:

$$\frac{\mathrm{d}\sigma}{\mathrm{d}\eta^{\text{jet}}} = \text{BG} + \Sigma_{\mathbb{P}} \left\{ c_g * (\text{hard gluons}) + (1 - c_g) * (\text{hard quarks}) \right\} \tag{6.38}$$

where BG is the non–diffractive background, c_g is the fraction of hard gluons and $\sum_{\mathbb{P}}$ is the momentum sum of the Pomeron. The results of the fits are combined with those of the

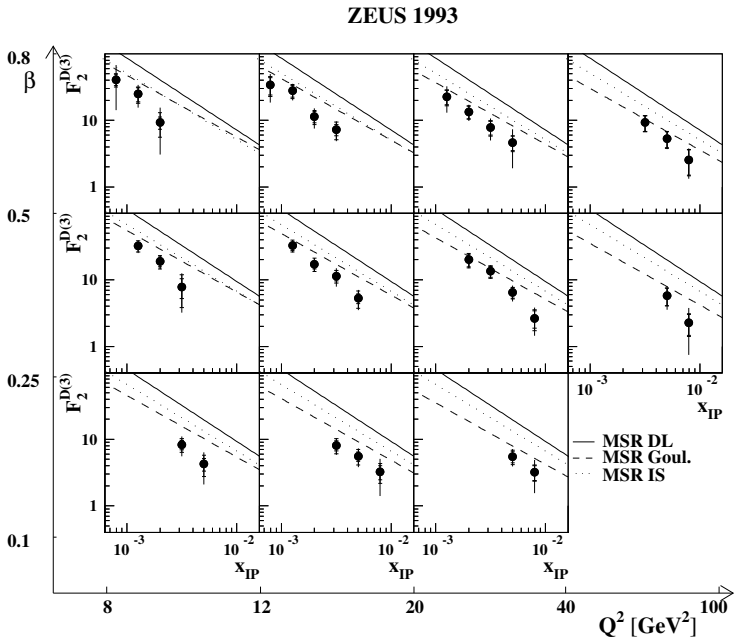

Figure 6.14: The results of $F_2^{D(3)}$ compared to an Ingelman–Schlein type model for which the momentum sum rule (MSR) for quarks within the Pomeron is assumed.

DIS diffractive structure function. This is shown [134] in figure 6.16 from which one may conclude that between 30 % and 80 % of the momentum of the Pomeron carried by partons is due to hard gluons.

Note that this is independent of the normalization of the flux of Pomerons from the proton and does not rely on assumptions on the momentum sum of the Pomeron.

Evolution equation for the Pomeron structure function

The third method of getting information about the partonic composition of the Pomeron is to assume that one can apply the DGLAP equations also for the Pomeron structure function and perform a global QCD analysis like in the proton case, using the equations 4.36 and 4.37.

Assuming factorization it is possible to integrate $F_2^{D(3)}(\beta, Q^2, x_{I\!P})$ over the measured region of $x_{I\!P}$ to get a modified Pomeron structure function $\tilde{F}_2^{I\!P}(\beta, Q^2)$, where the tilde sign

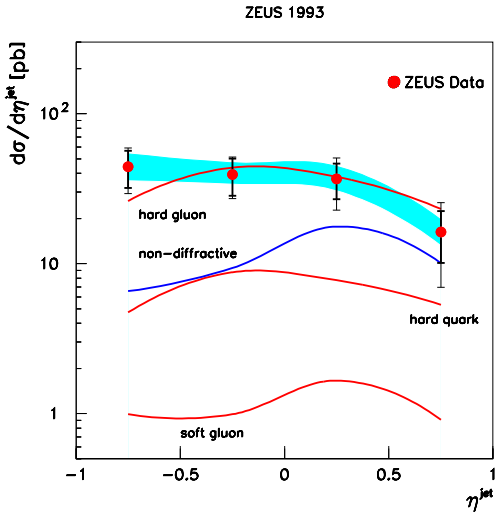

Figure 6.15: Measured differential cross section for inclusive jet production for $E_T^{\rm jet} > 8\,\mathrm{GeV}$ in the kinematic region $Q^2 < 4\,\mathrm{GeV}^2$. The shaded band displays the uncertainty due to the energy scale of the jets. The lines are predictions using the POMPYT generator for various parameterizations of the Pomeron parton densities.

indicates that the Pomeron structure function is only for a limited $x_{I\!P}$ range:

$$\tilde{F}_2^{I\!P}(\beta, Q^2) \equiv \int_{x_{I\!P_1}}^{x_{I\!P_2}} F_2^{D(3)}(\beta, Q^2, x_{I\!P})\, \mathrm{d}x_{I\!P} \tag{6.39}$$

At present the measured range [124] is over $x_{I\!P_1} = 3 \times 10^{-4}$ and $x_{I\!P_2} = 0.05$.

The Pomeron structure function $\tilde{F}_2^{I\!P}(\beta, Q^2)$ is shown [135] in the left hand side of figure 6.17 as function of Q^2 for different β regions. At low β it shows the positive scaling violation, just like for the proton case. However at high β, it still shows a positive scaling violation, unlike the proton case and more like the photon case. The only way to get such a behaviour, assuming the homogeneous DGLAP equations to hold also for the Pomeron, is to assume a substantial gluon component in the structure of the diffractive exchange, as shown on the upper right hand side of figure 6.17. As Q^2 increases the fraction of the Pomeron momentum carried by the gluons decreases somewhat but still remains in excess of 80 %, as seen in the bottom right hand side of the figure.

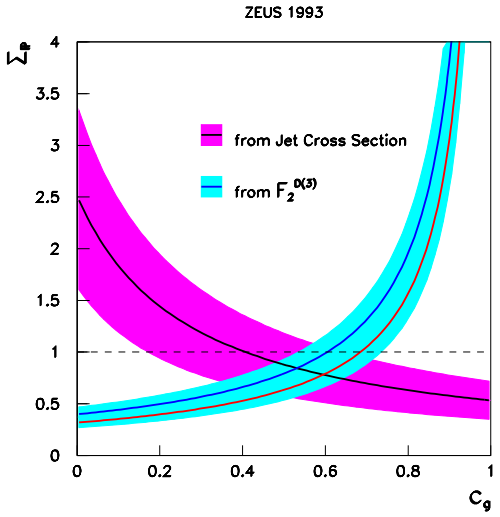

Figure 6.16: The plane of the variables $\Sigma_{\mathbb{P}}$ (momentum sum) and c_g (relative contribution of hard gluons in the Pomeron). The thick solid line displays the minimum for each value of c_g obtained from the χ^2 fit (the shaded area represents the $1\,\sigma$ band around these minima) to the measured $\mathrm{d}\sigma/\mathrm{d}\eta^{\mathrm{jet}}(\eta^{\mathrm{had}}_{\mathrm{max}} < 1.8)$ using the predictions of POMPYT. The constraint imposed in the $\Sigma_{\mathbb{P}} - c_g$ plane by the measurement of the diffractive structure function in DIS ($F_2^{D(3)}$) for two choices of the number of flavours (upper dot-dashed line for $\Sigma_{\mathbb{P}q} = 0.40$ and lower dot-dashed line for $\Sigma_{\mathbb{P}q} = 0.32$) is also shown. The horizontal dashed line displays the relation $\Sigma_{\mathbb{P}} = 1$.

6.5.5 The Pomeron intercept from DIS diffraction

It is of interest to compare the Pomeron intercept as extracted from the DIS diffractive reactions to that obtained from photoproduction and from hadronic diffractive processes. We will present here two methods of obtaining the Pomeron intercept in DIS. One is using the relation 6.37 which connects the exponent n of the Pomeron flux with its trajectory. The other is to look at the W dependence of the differential cross section with respect to the diffractive mass M_X. One can of course also use the W dependence of other reactions, like the total $\gamma^* p$ cross section or that of exclusive vector meson production in DIS, to get information about the Pomeron intercept. This will be discussed in the next chapter.

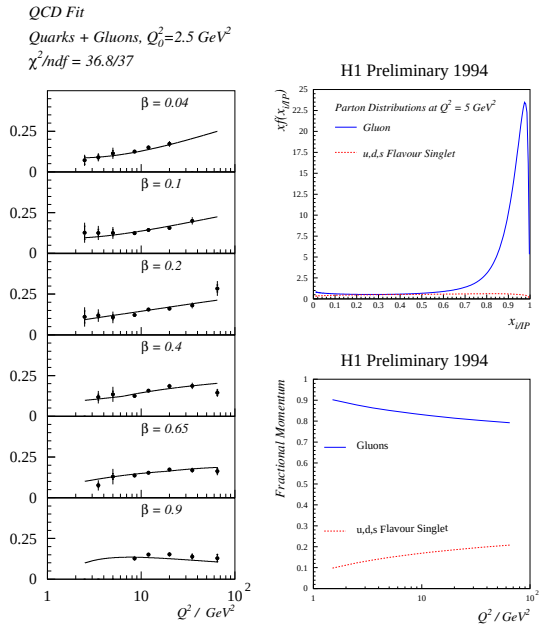

Figure 6.17: The Pomeron structure function $\tilde{F}_2^{\mathbb{P}}(\beta, Q^2)$ as function of Q^2 for fixed β regions (left hand side). The gluon momentum density distribution at a scale of $Q^2 = 5\,\mathrm{GeV}^2$ (upper right hand side). The evolution of the fractional momentum carried by the partons in the Pomeron as function of Q^2 (lower right hand side).

$\alpha_{\mathbb{P}}$ from n

The exponent n of the Pomeron flux is related to the Pomeron trajectory through equation 6.37. In order to obtain the Pomeron intercept from the t–integrated value of n one usually assumes a diffractive slope of about 5–6 GeV^{-2} and a slope of the Pomeron trajectory $\alpha'_{\mathbb{P}} \sim 0.25$–$0.3\,\mathrm{GeV}^{-2}$ [30].

The values presented [124, 130] in section 6.5.3 were based on low statistics data and thus had large errors for carrying out a meaningful comparison. The higher luminosity data allow a more detailed study of the behaviour of n. The value of n is shown [136] in figure 6.18(a) as function of β, integrated over the measured Q^2 range and in (b) as function of Q^2 integrated over the measured β range. The improved precision and enhanced kinematic range clearly reveals deviations from the universal factorization observed in figure 6.13. While there is no obvious dependence on Q^2, one sees that the value of n decreases significantly with β for $\beta \leq 0.3$, corresponding to large M_X values. One possible explanation [135] of this

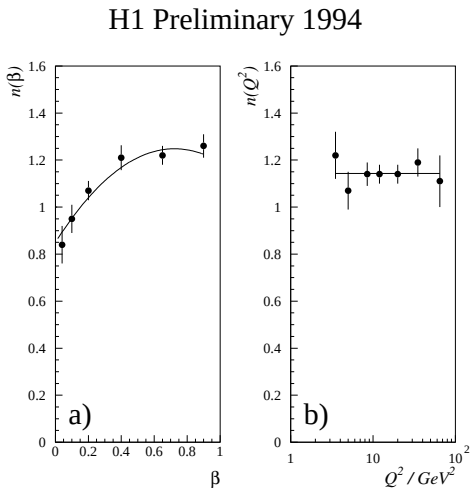

Figure 6.18: The dependence of the exponent of the Pomeron flux n on (a) β and on (b) Q^2.

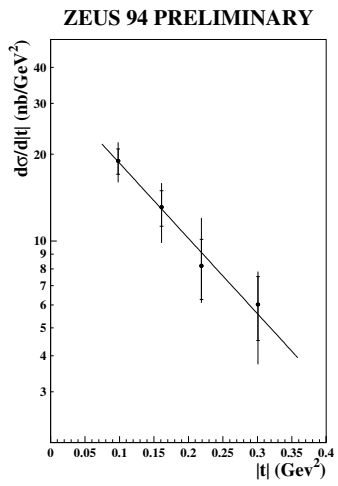

Figure 6.19: Differential cross section $\mathrm{d}\sigma/\mathrm{d}t$ for diffractive DIS events with a leading proton with a longitudinal momentum fraction $x_L > 0.97$, in the range $4 < Q^2 < 30\,\mathrm{GeV}^2$, $70 < W < 210\,\mathrm{GeV}$ and $0.02 < \beta < 0.4$.

decrease, without abandoning the hypothesis of factorization, is to assume that in addition to the Pomeron there is a small contribution from the exchange of meson trajectories such as the $f_2^0(1270)$, for which one would expect $n \sim 0$. With this assumption one can explain the behaviour of n by a superposition of a Pomeron trajectory having $n_{I\!P} = 1.29 \pm 0.03(\mathrm{stat}) \pm 0.07(\mathrm{syst})$ and $n_M = 0.3 \pm 0.3(\mathrm{stat}) \pm 0.6(\mathrm{syst})$. From these values and from using the diffractive slope and Pomeron trajectory slope as mentioned above, one gets [135] a Pomeron intercept:

$$\alpha_{I\!P}(0) = 1.18 \pm 0.02(\mathrm{stat}) \pm 0.04(\mathrm{syst}) \tag{6.40}$$

The intercept for the meson trajectory comes out from the fit to be $\alpha_M(0) = 0.6 \pm 0.1(\mathrm{stat}) \pm 0.3(\mathrm{syst})$, consisted with the value expected for the trajectory associated with the f_2 meson.

With the use of the leading proton spectrometer (LPS) [4] one can actually measure the t distribution of the diffractively produced DIS reactions in a limited β range. This was done [137] for the kinematic range $4 < Q^2 < 30\,\mathrm{GeV}^2$, $70 < W < 210\,\mathrm{GeV}$ and $0.02 < \beta < 0.4$ and is displayed in figure 6.19. The resulting value of the slope is $b = 5.9 \pm 1.3(\mathrm{stat})^{+1.1}_{-0.7}(\mathrm{syst})\,\mathrm{GeV}^{-2}$. The LPS data have been used to extract the diffractive structure function and yielded [137] an exponent value of $n_{I\!P} = 1.28 \pm 0.07(\mathrm{stat}) \pm 0.15(\mathrm{syst})$ which can be converted to a Pomeron slope of

$$\alpha_{I\!P}(0) = 1.17 \pm 0.04(\mathrm{stat}) \pm 0.08(\mathrm{syst}) \tag{6.41}$$

in good agreement with the value in 6.40. Note that in case of the LPS measurement the outgoing proton is detected and thus one has no corrections for background or for double dissociation processes.

$\alpha_{I\!P}$ from the W dependence of the diffractive cross section

One can use the reaction $\gamma^* p \to XN$, where N is a nucleonic system with $M_N < 4\,\mathrm{GeV}$, to measure the diffractive differential cross section $\mathrm{d}\sigma^{\mathrm{diff}}/\mathrm{d}M_X$. This differential cross section has a W dependence which in the Regge model is given by $(W^2)^{(2\alpha_{I\!P}-2)}$. A novel method of extracting the diffractive cross section from the non–diffractive background is the realization that for the latter low $\ln M_X^2$ of the hadronic system observed in the detector are exponentially suppressed. This can be seen [138] in figure 6.20 for the W range of $W = 60 - 245\,\mathrm{GeV}$ at $Q^2 = 31\,\mathrm{GeV}^2$. One sees that the non–diffractive contribution moves to larger $\ln M_X^2$ values proportional to $\ln W^2$.

The differential cross section for the diffractive DIS reaction was determined as function of W for different M_X and Q^2 regions. In each (M_X, Q^2) bin, a fit of the form:

$$\frac{\mathrm{d}\sigma^{\mathrm{diff}}(M_X, W, Q^2)}{\mathrm{d}M_X} \sim (W^2)^{(2\alpha_{I\!P}-2)} \tag{6.42}$$

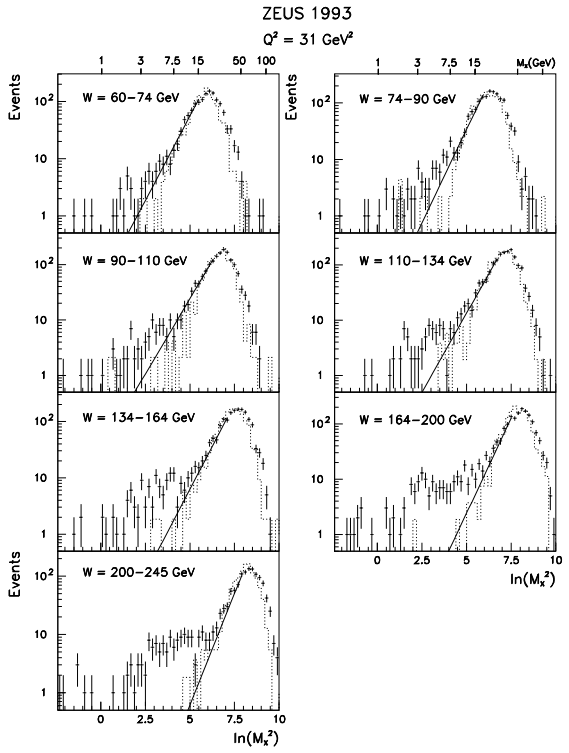

Figure 6.20: Distribution of $\ln M_X^2$ for the W intervals indicated at $Q^2 = 31\,\mathrm{GeV}^2$. The solid lines show the extrapolation of the non–diffractive background.

was performed, yielding a series of values for the Pomeron intercept for each (M_X, Q^2) bin. One gets intercept values consistent with those mentioned in the earlier section.

How can one understand the Pomeron intercept values in DIS? They seem to be significantly higher than the value of 1.08 obtained from photoproduction or hadronic reactions. Is it a different Pomeron? Are there two Pomerons? Does one approach the BFKL Pomeron of an intercept of 1.5 when measuring at higher Q^2 values? We will discuss these questions in the next chapter.

6.6 Summary

In this chapter we discussed the following issues:

- We defined some basic concepts connected with diffractive processes and showed their connection with the Regge formalism. In particular we discussed the trajectory intercept and its relation to the total and diffractive cross section. In addition we discussed the shrinkage of the elastic scattering slope.

- The diffractive phenomena is clearly observed in photoproduction reactions with a rate similar to that in hadronic reactions.

- Diffractive processes are present also in DIS reactions due to the fluctuations of highly virtual photons in the low x region. These processes are observed as a high rate of large rapidity gap events in DIS reactions. This opens up the possibility of studying DIS on the Pomeron.

- Observation of jets in DIS diffractive processes indicate that one could interpret them as the interaction of the virtual photon with partons within the Pomeron.

- We defined the diffractive structure function and checked that experimentally the factorization hypothesis holds in case of the Pomeron, over the measured kinematic region.

- The partonic content of the Pomeron was studied and evidence was shown for a large gluonic component in the Pomeron, carrying a large fraction of the Pomeron momentum.

- The Pomeron intercept as determined in DIS processes seems to be significantly larger than that determined from photoproduction and hadronic total cross section.

Chapter 7

Interplay Between Soft and Hard Interactions

This chapter deals with the interrelations of soft and hard processes. We know how to calculate hard processes by using pQCD. However when we compare the calculation with data we would like to isolate only the hard part. Do we really know how to do it? Are the two processes completely separable? How can one define hard reactions? These questions will be discussed in this chapter. For completeness and easy reading, some of the arguments presented in the earlier chapters will be repeated.

7.1 Introduction

One of the aims of building HERA was to study the deep inelastic scattering (DIS) region with data at low x and high Q^2. Yet, recently efforts are being made to get to lower and lower Q^2 values in the low x region in order to study the transition from photoproduction to the DIS regime. The main motivation for looking at the transition region is the following: at $Q^2 = 0$ the dominant processes are of non–perturbative nature and are well described by the Regge picture. As Q^2 increases, the exchanged photon is expected to shrink, one expects perturbative QCD to take over and therefore to be able to make exact calculations to confront with data. What can one learn from the transition between soft processes (low virtuality) and hard processes (high virtuality)? Where does the change take place? Is it a sudden transition or a smooth one? The transition should shed light on the interplay between soft and hard interactions.

7.2 Operational definition

It is not completely clear what one means by soft and hard interaction. One would have hoped that by going to the region of DIS one has a better way of probing the hard interactions. As a guideline to help distinguish the two, let us define some operational criteria for what we would consider as a soft and as a hard process. We can not do it in the most general terms, but let us concentrate on some selected measurements: total cross sections and elastic cross sections, the first being the most inclusive and the latter the most exclusive measurement we can make. At high energies, both these processes are dominated by a Pomeron exchange.

As discussed earlier, the total $\pi^{\pm}p, K^{\pm}p, pp, \bar{p}p$ and γp cross sections show a slow dependence on the center of mass energy W, consistent with the so–called soft pomeron [31], having a trajectory

$$\alpha_{\mathbb{P}(\text{soft})} = 1.08 + 0.25t \tag{7.1}$$

The hard or the perturbative Pomeron, also called the Lipatov Pomeron or the BFKL [60, 61, 62] Pomeron, is expected to have a trajectory

$$\alpha_{\mathbb{P}(\text{hard})} = 1 + \frac{12 \ln 2}{\pi}\alpha_S \tag{7.2}$$

The definition of the hard $\mathbb{P}$ is quite vague. First, the value of the intercept which is usually taken as 1.5 is a very rough estimate using the expression of the expected power of the reggeized gluon. Using a leading order calculation in $\ln 1/x$, the distribution of the momentum density of the gluon is expected to have the form $xg(x, Q^2) \sim x^{-\lambda}$ where $\lambda = \alpha_S/0.378$. Although usually the value of λ is taken to be 0.5 [139, 140], one should note that this requires a value of $\alpha_S = 0.18$, which happens only at large Q^2, whereas the BFKL calculation is expected to be valid for moderate Q^2 values. The second comment about the assumed hard $\mathbb{P}$ form is the fact that the slope of this trajectory is taken to be zero. The reason for this assumption can be understood intuitively by the fact that the slope is inversely proportional to the average transverse momentum square of hadrons, which is expected to be much larger in hard interactions compared to soft ones.

Following the above definitions of the soft and the hard Pomeron, we have some expectations for the behaviour of the total $\gamma^* p$ cross section, $\sigma_{tot}^{\gamma^* p}$, and the elastic one, which in the HERA case is the reaction $\sigma(\gamma^* p \to Vp)$. These are presented in table 7.1.

Table 7.1: Expected behaviour of soft and hard processes.

quantity	W dep	soft	hard
$\sigma_{tot}^{\gamma^* p}$	$(W^2)^{\alpha_{\mathbb{P}}(0)-1}$	$(W^2)^{0.08}$	$(W^2)^{0.5}$
slope b of $d\sigma/dt$	$\sim 2\alpha' \ln W^2$	shrinkage	no shrinkage
$\sigma(\gamma^* p \to Vp)$	σ_{tot}^2/b	$(W^2)^{0.16}/b$	$(W^2)^1$

Before turning to the actual data, let us review some of the models relevant for the low x and low Q^2 region.

7.3 The models for the low x low Q^2 region

7.3.1 Donnachie and Landshoff (DL)

Donnachie and Landshoff [31] found a simple Regge picture describing all hadron–hadron cross sections with a sum of two terms, that of a Pomeron exchange and that of a reggeon. They showed this picture to describe also real photoproduction cross sections. They extended the picture for virtual photons ($\gamma^*, Q^2 < 10\,\mathrm{GeV}^2$) to see what is the expected contribution of the non–perturbative mechanism to higher Q^2 [141, 74]. The main interest is in the low x region where the Pomeron dominates and thus the question of interest is what is the contribution of the 'soft' pomeron at intermediate Q^2.

7.3.2 Capella, Kaidalov, Merino, Tran–Than–Van (CKMT)

In this picture [142, 143] there is no 'soft' or 'hard' Pomeron, there is just one 'bare' Pomeron. At low Q^2 absorptive corrections (rescattering) give a Pomeron with an effective intercept of $1+\Delta_0(\Delta_0 \sim 0.08)$. If one uses an eikonal approach, the bare intercept becomes $1+\Delta_1(\Delta_1 \sim 0.13)$. A more complete absorptive calculation results in $1+\Delta_2(\Delta_2 \sim 0.24)$. The absorptive corrections decrease rapidly with Q^2. They parametrize the data with this behavior of the Pomeron up to $Q^2 < 5\,\mathrm{GeV}^2$ and use it then as initial conditions to a pQCD evolution.

7.3.3 Badelek and Kwiecinski (BK)

Badelek and Kwiecinski [144, 145] describe the low Q^2 region by using the generalized vector dominance model (GVDM): the proton structure function F_2 is represented by the contribution of a large number of vector mesons which couple to virtual photons. The low mass ones, ρ, ω, ϕ contribute mainly at low Q^2, while the higher mass are determined by the asymptotic structure function F_2^{AS} which is described by pQCD. The total structure function is given by a Q^2 weighted sum of the two components.

7.3.4 Abramowicz, Levin, Levy, Maor (ALLM)

This parameterization [18, 19] is based on a Regge motivated approach extended into the large Q^2 regime in a way compatible with QCD expectations. This approach allows to parametrize the whole x, Q^2 phase space, fitting all the existing data.

7.3.5 Some general comments

The DL parametrization provides a good way to check to what value of Q^2 the simple 'soft' Pomeron picture can be extended. It is not meant to be a parameterization which describes the whole DIS regime. The CKMT and BK parametrizations are attempts to get the best possible presentation of the initial conditions to a pQCD evolution. The ALLM does not use the regular pQCD evolution equation but parametrizes the whole of the DIS phase space by a combination of Regge and QCD motivated parametrizations.

All parameterizations make sure that as $Q^2 \to 0$ also $F_2 \to 0$ linearly with Q^2.

7.3.6 Details of the parametrizations

The DL parameterization

The proton structure function F_2 is given by

$$F_2(x,Q^2) \sim A\xi^{-0.0808}\phi(Q^2) + B\xi^{0.4525}\psi(Q^2), \tag{7.3}$$

where ξ is the rescaled variable

$$\xi = x\left(1+\frac{\mu^2}{Q^2}\right), \tag{7.4}$$

with x being the Bjorken–x and the scale variable μ has different values for different flavors: for u and d quarks $\mu = 0.53\,\mathrm{GeV}$, for the strange quark s, $\mu = 1.3\,\mathrm{GeV}$ and for the charm quark c, $\mu = 2\,\mathrm{GeV}$. The two functions $\phi(Q^2)$ and $\psi(Q^2)$ make sure that the structure function vanishes linearly with Q^2 as $Q^2 \to 0$,

$$\phi(Q^2) = \frac{Q^2}{Q^2+a} \qquad \psi(Q^2) = \frac{Q^2}{Q^2+b}. \tag{7.5}$$

The four parameters A, B, a and b are constrained so as to reproduce the total real photoproduction data,

$$\frac{A}{a}(\mu^2)^{-0.0808} = 0.604 \qquad \frac{B}{b}(\mu^2)^{0.4525} = 1.15. \tag{7.6}$$

In addition there is also a higher–twist term $ht(x,Q^2)$ contributing to the structure function,

$$ht(x,Q^2) = D\frac{x^2(1-\xi)^2}{1+\frac{Q^2}{Q_0^2}}, \tag{7.7}$$

with the parameters $D = 15.88$ and $Q_0 = 550\,\mathrm{MeV}$.

The CKMT parameterization

Contrary to the DL parameterization, the CKMT assumes that the power behavior of x is Q^2 dependent,

$$F_2(x,Q^2) = Ax^{-\Delta(Q^2)}(1-x)^{n(Q^2)+4}\left(\frac{Q^2}{Q^2+a}\right)^{1+\Delta(Q^2)} + Bx^{1-\alpha_R}(1-x)^{n(Q^2)}\left(\frac{Q^2}{Q^2+b}\right)^{\alpha_R}, \tag{7.8}$$

where α_R is the Reggeon trajectory intercept, the power $n(Q^2)$ is given by

$$n(Q^2) = \frac{3}{2}\left(1 + \frac{Q^2}{Q^2 + c}\right) \tag{7.9}$$

and the power behavior of x is given by

$$\Delta(Q^2) = \Delta_0\left(1 + \frac{Q^2}{Q^2 + d}\right). \tag{7.10}$$

The constant parameters are determined by the requirement that F_2 and the derivative $\frac{dF_2}{d\ln Q^2}$ at $Q^2 = Q_0^2$ to coincide with that obtained from the pQCD evolution equations. They can do so at $Q_0^2 = 2\,\mathrm{GeV}^2$, provided a higher–twist term is added to that of pQCD,

$$F_2(x,Q^2) = F_2^{pQCD}(x,Q^2)\left(1 + \frac{f(x)}{Q^2}\right) \tag{7.11}$$

for $Q^2 \geq Q_0^2$. The values of the parameters are: $A = 0.1502$, $a = 0.2631\,\mathrm{GeV}^2$, $\Delta_0 = 0.07684$, $d = 1.117\,\mathrm{GeV}^2$, $b = 0.6452\,\mathrm{GeV}^2$, $\alpha_R = 0.415$, $c = 3.5489\,\mathrm{GeV}^2$.

The BK parameterization

The proton structure function is written as the sum of two terms, a vector meson part (V) and a partonic part (par),

$$F_2(x,Q^2) = F_2^V(x,Q^2) + F_2^{\mathrm{par}}(x,Q^2). \tag{7.12}$$

The part representing the contribution from vector mesons which couple to the virtual photon is given by

$$F_2^V(x,Q^2) = \frac{Q^2}{4\pi}\Sigma_V \frac{M_V^4 \sigma_V(W^2)}{\gamma_V^2 (Q^2 + M_V^2)^2}, \tag{7.13}$$

where $\gamma_V^2/(4\pi)$ is the direct photon vector meson coupling, W is the $\gamma^* p$ center of mass energy and σ_V is the total Vp cross section. The sum is over all vector meson satisfying $M_V^2 < Q_0^2$, where M_V is the mass of the vector meson and Q_0 is a parameter.

The partonic part of the structure function is given by the expression

$$F_2^{\mathrm{par}}(x,Q^2) = \frac{Q^2}{Q^2 + Q_0^2} F_2^{AS}(\bar{x}, Q^2 + Q_0^2), \tag{7.14}$$

where the asymptotic structure function F_2^{AS} is given by pQCD at the scaled value of

$$\bar{x} = \frac{Q^2 + Q_0^2}{W^2 + Q^2 - M^2 + Q_0^2}, \tag{7.15}$$

where M is the proton mass. In practice the parameterization uses $Q_0^2 = 1.2\,\mathrm{GeV}^2$ and thus sums over the contribution of the 3 lightest vector mesons ρ, ω and ϕ.

The ALLM parameterization

This parameterization attempts to cover the whole x, Q^2 region above the resonances ($W^2 > 3\,\mathrm{GeV}^2$), at the expense of introducing more parameters than the other parameterizations. The proton structure function has the form

$$F_2(x,Q^2) = \frac{Q^2}{Q^2 + M_0^2}\left(F_2^{\mathcal{P}}(x,Q^2) + F_2^{\mathcal{R}}(x,Q^2)\right), \tag{7.16}$$

where M_0 is the effective photon mass. The functions $F_2^{\mathcal{P}}$ and $F_2^{\mathcal{R}}$ are the contribution of the Pomeron $\mathcal{P}$ or Reggeon $\mathcal{R}$ exchanges to the structure function. They take the form

$$\begin{aligned} F_2^{\mathcal{P}}(x,Q^2) &= c_{\mathcal{P}}(t) x_{\mathcal{P}}^{a_{\mathcal{P}}(t)} (1-x)^{b_{\mathcal{P}}(t)}, \\ F_2^{\mathcal{R}}(x,Q^2) &= c_{\mathcal{R}}(t) x_{\mathcal{R}}^{a_{\mathcal{R}}(t)} (1-x)^{b_{\mathcal{R}}(t)}. \end{aligned} \tag{7.17}$$

The slowly varying function t is defined as

$$t = \ln\left(\frac{\ln\frac{Q^2+Q_0^2}{\Lambda^2}}{\ln\frac{Q_0^2}{\Lambda^2}}\right). \tag{7.18}$$

The two scaled variables $x_{\mathcal{P}}$ and $x_{\mathcal{R}}$ are modified Bjorken–x variables which include mass parameters $M_{\mathcal{P}}$ and $M_{\mathcal{R}}$ which can be interpreted as effective Pomeron and reggeon masses:

$$\begin{aligned} \frac{1}{x_{\mathcal{P}}} &= 1 + \frac{W^2 - M^2}{Q^2 + M_{\mathcal{P}}^2}, \\ \frac{1}{x_{\mathcal{R}}} &= 1 + \frac{W^2 - M^2}{Q^2 + M_{\mathcal{R}}^2}. \end{aligned} \tag{7.19}$$

7.4 Comparison to data

7.4.1 The total $\gamma^* p$ cross section, $\sigma_{tot}^{\gamma^* p}$

The total $\gamma^* p$ cross section, $\sigma_{tot}^{\gamma^* p}$, can be related to the proton structure function F_2 through the relation

$$F_2(x,Q^2) = \frac{Q^2(1-x)}{4\pi^2\alpha}\frac{Q^2}{Q^2 + 4m_p^2 x^2}\sigma_{tot}^{\gamma^* p}(x,Q^2) \tag{7.20}$$

where the total $\gamma^* p$ includes both the cross section for the absorption of transverse and of longitudinal photons. In this expression the Hand [47] definition of the flux of virtual photons is used.

Figure 7.1 presents the dependence of $\sigma_{tot}^{\gamma^* p}$, obtained through equation (7.20) from the measured F_2 values [15, 16], on the square of the center of mass energy W^2, for fixed values of the photon virtuality Q^2. The new preliminary very low Q^2 measurements of the ZEUS collaboration [146], as well as those of the NMC collaboration [52] are included in the figure. Also shown are the measurements of the total real photoproduction cross

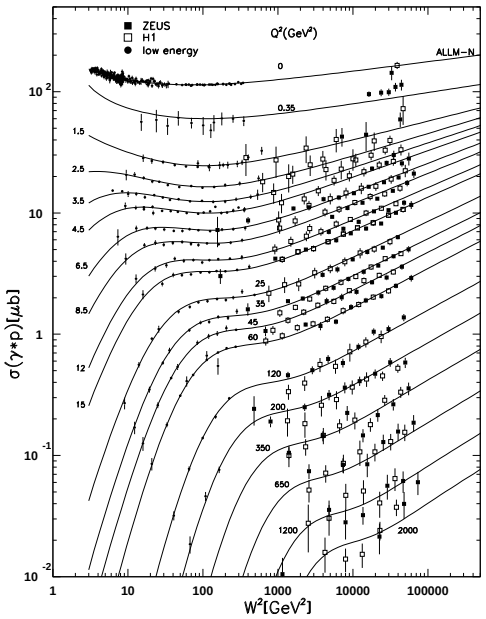

Figure 7.1: The total $\gamma^* p$ cross section as function of W^2 from the F_2 measurements for different Q^2 values. The lines are the expectations of a new ALLM type parametrization.

sections. While the data below $Q^2 = 1\,\mathrm{GeV}^2$ show a very mild W dependence, the trend changes as Q^2 increases. Note that for higher values of Q^2 one sees the typical threshold behaviour for the case when $W^2 < Q^2$ [17]. The curves are the results of a new ALLM type parametrization which added to the earlier data used in the previous fit data from E665 [147] and the published HERA [148, 149] data.

Instead of comparing the data as presented in figure 7.1 with the different parameterizations, it is more economical as well as instructive to study the energy dependence of the $\gamma^* p$ cross section for fixed Q^2 values [59]. In order to see how the slope of the W dependence changes with Q^2, the cross section values in the region where $W^2 \gg Q^2$ were fitted to the form $\sigma_{tot}^{\gamma^* p} = \sigma_1 W^{2\Delta}$ for each fixed Q^2 interval. The resulting values of Δ from the fit are plotted against Q^2 in figure 7.2. Similar results have been obtain by the H1 collaboration [16] who use only their own data to fit the structure function measurements to the form $F_2 \sim x^{-\Delta}$. Also included in the figure are the recent preliminary results of the ZEUS collaboration [146] in the region $0.2 < Q^2 < 0.8\,\mathrm{GeV}^2$. One can see the slow increase of Δ with Q^2 from the value of 0.08 at $Q^2 = 0$, to around 0.2 for $Q^2 \sim 10 \ldots 20\,\mathrm{GeV}^2$ followed by a further increase to around $0.3 \ldots 0.4$ at high Q^2. One would clearly profit

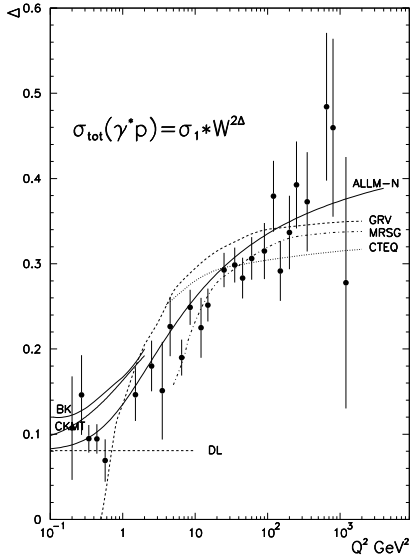

Figure 7.2: The Q^2 dependence of the parameter Δ obtained from a fit of the expression $\sigma_{tot}^{\gamma^* p} = \sigma_1 W^{2\Delta}$ to the data in each Q^2 bin. The curves are the expectations of the parameterizations mentioned in the text.

from more precise data, expected to come soon.

The curves are the expectations of the DL, BK, CKMT, and the updated ALLM parameterization, which includes also some of the recent HERA data in its fit. In addition, the expectations of the GRV [73], CTEQ [72] and MRSG [70] are also shown.

The DL parameterization can describe the data up to $Q^2 \sim 1\,\mathrm{GeV}^2$. All the others give in general the right features of the Q^2 behavior with a smooth transition from soft to hard interactions with an interplay between the two in the intermediate Q^2 range.

7.4.2 Vector meson production in γp and in $\gamma^* p$

Given the behaviour of the $\sigma_{tot}^{\gamma^* p}$ data, what kind of energy behaviour would one expect for the 'elastic' process $\gamma^* p \to Vp$ for real and virtual photons? In case of photoproduction we have seen that the total cross section follows the expectations of a soft DL type $\mathbb{P}$. Thus if one takes into account the shrinkage at the HERA energies, one expects $\sigma(\gamma p \to Vp) \sim W^{0.22}$. In case of DIS production of vector mesons in the range $Q^2 \sim 10 \ldots 20\,\mathrm{GeV}^2$, the expectations are $\sigma(\gamma^* p \to Vp) \sim W^{0.8}$, since in this case one expects almost no shrinkage.

Figure 7.3 presents the measurements of the total and 'elastic' vector meson photopro-

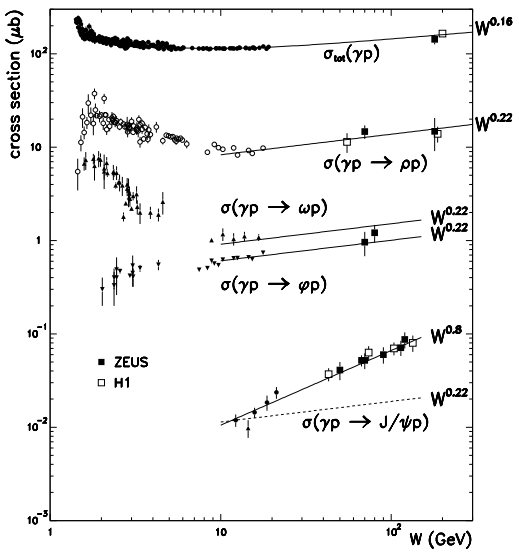

Figure 7.3: The total and 'elastic' vector meson photoproduction measurements as function of W, for the vector mesons ρ, ω, ϕ and J/Ψ. The curve to the total photoproduction cross section is the DL parametrization ($W^{0.16}$). The other lines are curves of the form $W^{0.22}$ and $W^{0.8}$.

duction cross sections as function of the γp center of mass energy W. As one can see, the high energy measurements of the total and the ρ [150, 151], ω [152] and ϕ photoproduction [153] follow the expectations of a soft DL type Pomeron. However, the cross section for the reaction $\gamma p \to J/\Psi p$ [85, 154] rises much faster than the expected $W^{0.22}$ rise from a soft reaction. In fact, it can be well described by a power behaviour of $\sim W^{0.8}$. This surprising behaviour can be understood if one considers the scale which is involved in the interaction. In case of photoproduction reaction, the scale cannot be set by the photon since $Q^2 = 0$. The scale is set by the mass of the vector meson and by the transverse momentum involved in the reaction. Thus, for the lighter vector mesons the scale is still small enough to follow a soft behaviour. However, the mass of the J/Ψ is large enough to produce a scale which would be considered as a hard interaction.

The reaction $\gamma^* p \to \rho^0 p$ has been measured [155, 156] at six Q^2 values from 0.48 to 20 GeV^2 and is shown in figure 7.4. One observes that the W dependence gets steeper as Q^2 increases. In order not to be dependent on the normalizations of different experiments, the ZEUS data alone has been fitted to a W^a form. Though the data has quite large errors which is reflected in the large errors on the power a, one sees the trend of increasing a

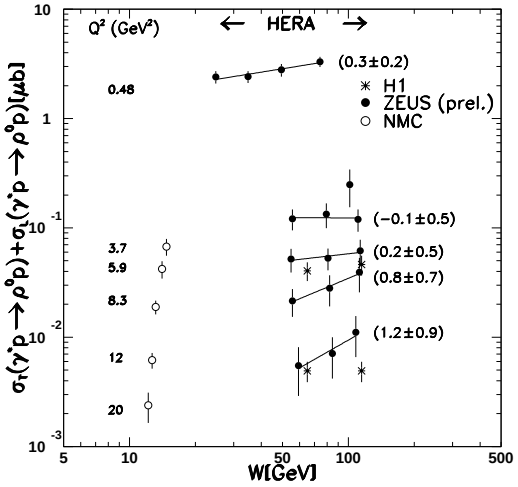

Figure 7.4: The dependence of the cross section for the reaction $\gamma^* p \to \rho^0 p$ on W, for different Q^2 values.

with Q^2.

The reaction $\gamma^* p \to \phi p$ has been measured [157] for Q^2 of 8.2 and 14.7 GeV^2 and is presented in figure 7.5. In this case, one has to use the lower W NMC data to get the slope of the energy dependence. It is steeper than that expected for a soft process and is compatible with the $W^{0.8}$ observed for the photoproduction J/Ψ case. For comparison, the $Q^2 = 0$ photoproduction with the shallow W dependence is also shown.

The J/Ψ vector meson already shows a steep W dependence for the photoproduction case. In figure 7.6 the photoproduction cross section is shown together with measurements of the reaction $\gamma^* p \to J/\Psi p$ at $Q^2 = 10$ and 20 GeV^2.

These results are consistent with the Q^2 dependence of Δ as shown in figure 7.2.

The ratio of the higher mass vector mesons to ρ^0 cross sections is expected according to SU(4) to be:

$$\rho^0 : \omega : \phi : J/\Psi = 9 : 1 : 2 : 8 \tag{7.21}$$

This relation is quite badly broken in photoproduction for ϕ and for J/Ψ. For the case of the ϕ it is about 0.07 and for the J/Ψ it is somewhat W dependent and at the HERA W range it is about 0.005 for $Q^2 = 0$. As Q^2 increases one expects the SU(4) relations to be restored. For much higher Q^2 values one expects these relations to be broken again in the opposite direction.

In figure 7.7 the ratio $R(V^0/\rho^0)$ is presented as function of the vector meson mass

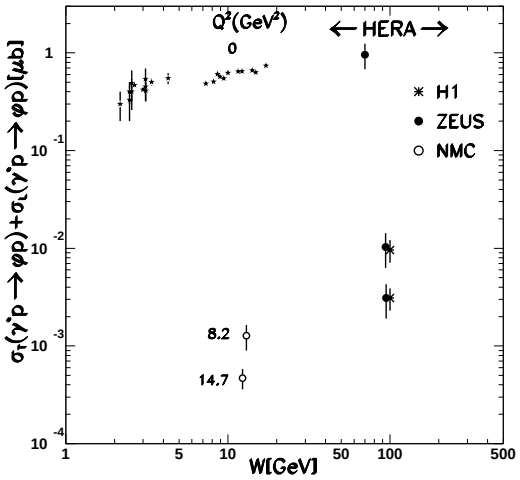

Figure 7.5: The dependence of the cross section for the reaction $\gamma^* p \to \phi p$ on W, for different Q^2 values.

squared M_V^2, for different Q^2 values as indicated next to the data points. One observes first that as the mass of the vector meson gets larger, the ratio becomes smaller and reaches a value of $< 10^{-3}$ for the Ψ'. As Q^2 increases the ratio get larger. It reaches close to the expected value of $2:9$ for the ϕ, close to 0.4 for the ρ', and ≈ 1 for the J/Ψ.

What can we learn from the behaviour of the slope? Does one see any shrinkage? It is not easy to conclude about that since there is no single experiment that has enough of a W range lever arm to measure shrinkage in one experiment. One thus is dependent on the systematics of different experiments. The photoproduction data of all three vector mesons ρ^0, ω and ϕ are consistent with shrinkage (see figure 7.8). What about the vector mesons produced in DIS?

The dependence of the slope of the differential cross section for the reaction $\gamma^* p \to \rho^0 p$ on W, is shown in figure 7.9 for $8 < Q^2 < 50\,\mathrm{GeV}^2$ (H1) and $5 < Q^2 < 30\,\mathrm{GeV}^2$ (ZEUS). The NMC data point is at $Q^2 \approx 10\,\mathrm{GeV}^2$. The HERA data alone can not, with the present measurement errors, distinguish between the shrinkage or non–shrinkage of the slope. Even with the addition of the NMC point the situation is not clear and one has to await more precise data.

One does however see a decrease of the slope with Q^2 in case of the exclusive ρ^0 production in DIS.

One does however see a decrease of the slope with Q^2 in case of the exclusive ρ^0 production in DIS. The slope seems to decrease from a value of about $10\,\mathrm{GeV}^{-2}$ at $Q^2 = 0$

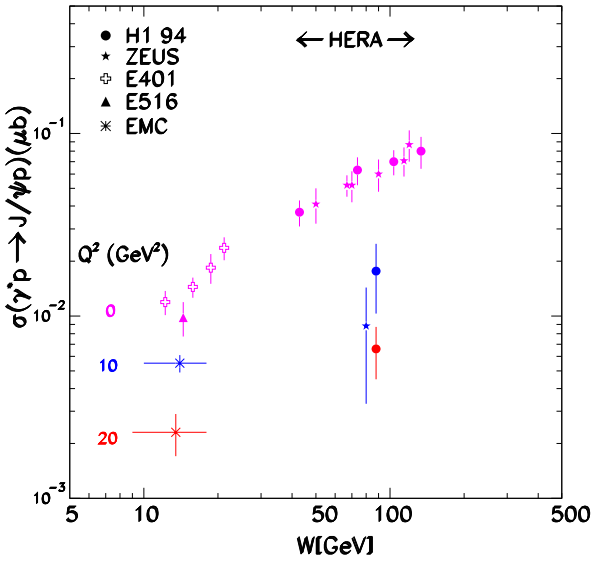

Figure 7.6: The dependence of the cross section for the reaction $\gamma^* p \to J/\Psi p$ on W, for different Q^2 values.

to about $5\,\mathrm{GeV}^{-2}$ at about $Q^2 = 20\,\mathrm{GeV}^2$. This result is consistent with the fact that as the scale gets larger, the reaction becomes harder and in case of hard processes all vector mesons are expected to have the same universal slope. This effect is nicely seen in the case of J/Ψ, where due to its large mass there is a hard scale already at $Q^2 = 0$, and thus the slope shows no change with Q^2.

It is worthwhile to note that the properties observed for vector mesons have a natural explanation in QCD, where vector meson production with a large scale can be described by an exchange mechanism of a Pomeron consisting of two gluon. For example, in the case of the model of Brodsky et al. [158] one expects that the differential ρ^0 cross section produced by longitudinal photons should be proportional to the gluon distribution in the proton:

$$\frac{\mathrm{d}\sigma}{\mathrm{d}t}(\gamma_L^* p \to \rho^0 p) \sim \frac{[\alpha_S(Q^2) x g(x,Q^2)]^2}{Q^6} C_\rho \qquad (7.22)$$

Since at low x values $[\alpha_S(Q^2) x g(x,Q^2)]^2 \sim Q$ and since the k_T dependence of the ρ^0 wave function introduces [159] another $Q^{0.5}$ dependence, the expectations of the QCD calculation are that the data should have a Q^n dependence, where $n = 4.5 \ldots 5$. The ZEUS [155] experiment finds $n = 4.2 \pm 0.8^{+1.4}_{-0.5}$ and the H1 [156] experimental result is $n = 4.8 \pm 0.8$ (statistical error only). The x dependence of the ZEUS [155] measurement is consistent

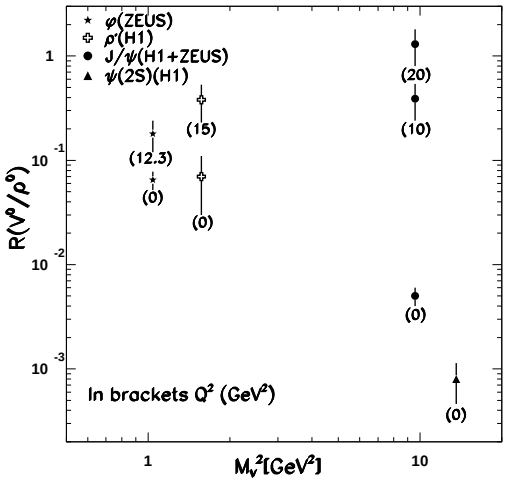

Figure 7.7: The ratio of the cross sections of vector mesons ϕ, ρ', J/Ψ and Ψ' to ρ^0 at different values of Q^2 as indicated in the figure.

with their gluon determination from their F_2 measurement.

7.5 DIS processes - hard or soft?

What have we learned from the behavior of the data with Q^2? What are we actually measuring? At low Q^2 the photon is known to have structure. Does F_2 still measure the structure of the proton? Bjorken [160] pointed out that physics is not frame dependent. The structure of the proton alone has no meaning. One has to study the $\gamma^* p$ interaction.

Let us look at the structure of a photon. It is a well known fact that real photon behave like hadrons when interacting with other hadrons. One way to understand this is by using the argument of Ioffe [87, 88]: the photon can fluctuate into a $q\bar{q}$ pair. The fluctuation time is given by

$$t_f = \frac{2E_\gamma}{m^2_{q\bar{q}}} \tag{7.23}$$

where E_γ is the photon energy in the rest system of the proton and $m_{q\bar{q}}$ is the mass of the $q\bar{q}$ system into which the photon fluctuates. The Vector Dominance Model assumes that the fluctuation of the photon is into vector mesons, $m_{q\bar{q}} \simeq m_V$, where m_V is the vector mesom mass. As long as $t_f \gg t_i$, where the interaction time $t_i \approx r_p$, with r_p being the proton radius, the photon interacts as if it were a hadron. When the photon becomes virtual with

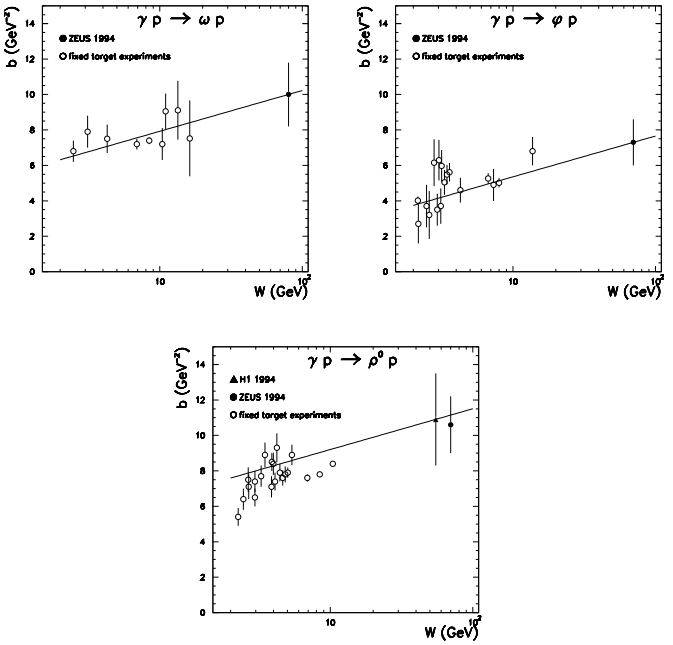

Figure 7.8: The dependence of the slope of the differential cross section

a negative square mass of Q^2, its fluctuation time becomes

$$t_f = \frac{2E_\gamma}{m^2_{q\bar{q}} + Q^2} \tag{7.24}$$

and thus at low energies and moderate Bjorken x, the fluctuation time becomes small and the virtual photon behaves like a point–like structureless object, consistent with the DIS picture described above.

However, at high energies or equivalently in the low x region studied at HERA, the fluctuation time of a virtual photon can be expressed as

$$t_f \approx \frac{1}{2Mx} \tag{7.25}$$

where M is the proton mass. This can be derived easily from formula 5.1 assuming $m^2_{q\bar{q}} \approx Q^2$ [125]. Thus in the HERA regime, a photon of virtuality as high as $Q^2 \sim 2-3\times10^3$ GeV^2 can fluctuate into a $q\bar{q}$ pair, which will survive till arrival on the proton target.

The photon can fluctuate into typically two configurations. A large size configuration will consist of an asymmetric $q\bar{q}$ pair with each quark carrying a small transverse momentum k_T (fig. 7.11(a)). For a small size configuration the pair is symmetric, each quark

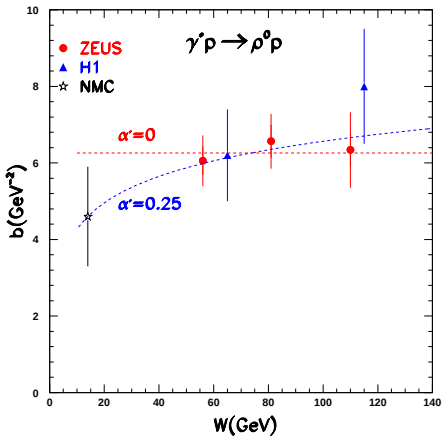

Figure 7.9: The dependence of the slope of the differential cross section for the reaction $\gamma^* p \to \rho^0 p$ on W, for $8 < Q^2 < 50\,\mathrm{GeV}^2$ (H1) and $5 < Q^2 < 30\,\mathrm{GeV}^2$ (ZEUS). The NMC data point is at $Q^2 \approx 10\,\mathrm{GeV}^2$.

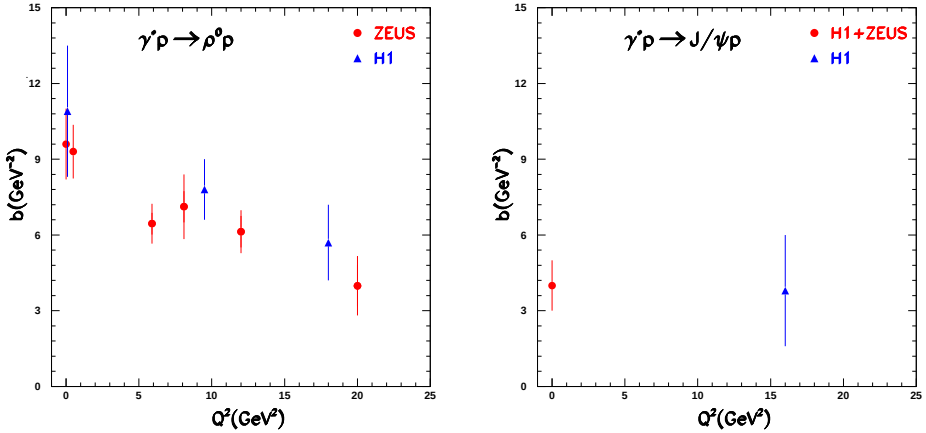

Figure 7.10: The dependence of the slope of the differential cross section for the reactions $\gamma^* p \to \rho^0 p$ (left) and $\gamma^* p \to J/\Psi p$ (right) on Q^2, for $< W > \approx 80\,\mathrm{GeV}$ (ρ^0) and $90\,\mathrm{GeV}$ (J/Ψ).

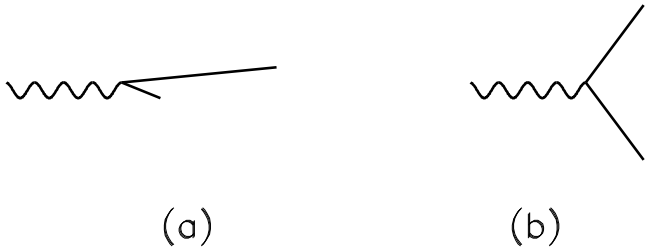

Figure 7.11: Fluctuation of the photon into a $q\bar{q}$ pair in (a) asymmetric small k_T configuration, (b) into a symmetric large k_T configuration

having a large k_T (fig. 7.11(b)). One expects the asymmetric large configuration to produce 'soft' physics, while the symmetric one would yield the 'hard' interactions.

In the aligned jet model (AJM) [161] the first configuration dominates while the second one is the 'sterile combination' because of color screening. In the photoproduction case ($Q^2 = 0$), the small k_T configuration dominates. Thus one has large color forces which produce the hadronic component, the vector mesons, which finally lead to hadronic non–perturbative final states of 'soft' nature. The symmetric configuration contributes very little. In those cases where the photon does fluctuate into a high k_T pair, color transparency suppresses their contribution.

In the DIS regime ($Q^2 \neq 0$), the symmetric contribution becomes bigger. Each such pair still contributes very little because of color transparency, but the phase space for the symmetric configuration increases. However the asymmetric pair still contribute also to the DIS processes. In fact, in the quark parton model (QPM) the fast quark becomes the current jet and the slow quark interacts with the proton remnant resulting in processes which look in the $\gamma^* p$ frame just like the 'soft' processes discussed in the $Q^2 = 0$ case. So there clearly is an interplay between soft and hard interactions also in the DIS region.

This now brings up another question. We are used by now to talk about the 'resolved' and the 'direct' photon interactions. However, if the photon always fluctuates into a $q\bar{q}$ pair even at quite large values of Q^2, what does one mean by a 'direct' photon interaction? To illustrate the problem, let us look at the diagram describing the photon–gluon fusion, which is usually considered in leading order a direct photon interaction and is shown in figure 7.12(a). An example of a resolved process is shown in figure 7.12(b) where a photon fluctuates into a $q\bar{q}$ pair with a given k_T, following by the interaction of one of the quarks with a gluon from the proton to produce a quark and a gluon with a given p_T.

In the diagram shown in figure 7.12(b) there are two scales, k_T and p_T. The classification of the process as 'direct' or 'resolved' depends on the relations between the two scales. If

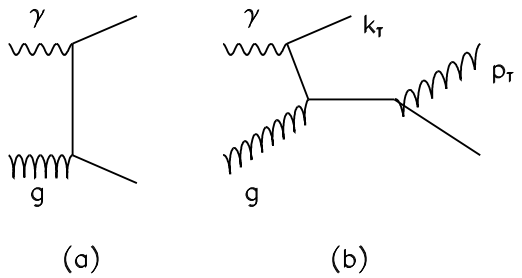

Figure 7.12: Diagrams describing examples of (a) 'direct' photon process, (b) 'resolved' photon process

$k_T \ll p_T$ we call it a resolved photon interaction, while in the case of $k_T \gg p_T$ one would consider this as a direct photon interaction. Practically in the latter case the p_T is too small to resolve the gluon and the quark jets as two separate jets, thus making it look like the diagram in figure 7.12(a). At low Q^2 the more likely case is that of $k_T \ll p_T$ and thus the resolved photon is the dominant component, while at high Q^2 the other case is more likely. A yet open question is how does one deal with the case where $k_T \sim p_T$.

7.6 Summary

We can summarize the results and discussions of this chapter in the following way:

- We have presented an operational definition of what we call soft and hard interactions by using the total cross section and the elastic process. The energy behaviour of the total and the elastic cross section is expected to be much steeper for hard interactions than for soft ones. In addition, the slope of the elastic differential cross section should shrink in the soft interactions while show no or very little shrinkage in case of hard interactions.

- The models describing the low–x low Q^2 region were discussed and compared to data. The energy behaviour of the total $\gamma^* p$ cross section shows a smooth transition from a shallow dependence at low Q^2 to a steeper one at higher Q^2.

- The vector meson exclusive production, which can be considered as the elastic processes for the photon case, follow the energy dependence behaviour of the total cross section. The W dependence get steeper for the ρ^0 and ϕ as Q^2 increases while it is already steep for the J/Ψ produced in the elastic photoproduction process.

- When a large scale is present, being the virtuality of the photon or the mass of the vector meson, the cross section is consistent with a rise driven by the rise of the gluon momentum density $xg(x, Q^2)$ with W. The Pomeron exchange mechanism described by two gluons gives results consistent with the data.

- The ratio of the cross sections of vector mesons compared to that of the ρ^0 is approaching the expectations from SU(4) as Q^2 increases.

- The present measurements of the slopes of the vector mesons are not precise enough to conclude anything about the shrinkage question.

- One would like to separate soft from hard interactions. However nothing is as soft as we would like nor as hard as we would like. There is an interplay of soft and hard processes at all values of Q^2. As Q^2 or any other scale increases, the amount of hard processes seems to increase. In order to resolve the hard processes one needs a good understanding of the soft fragmentation and hadronization. By combining various reactions one can try and extract the perturbative QCD part and to learn more about the interplay.

- The energy behavior of the $\gamma^* p$ cross section shows that there is a smooth transition between the Q^2 region where there is a mild energy dependence to that where the energy behavior is steeper. It happens somewhere in the region of about $1\,\mathrm{GeV}^2$. Does this tell us where soft interactions turn into hard ones? In order to understand the structure of the dynamics, one has to isolate in the transition region the specific configurations in k_T and p_T for a better insight of what is happening.

Acknowledgements

I would like to thank the organizers of the Banz lectures for setting up a special and very pleasant atmosphere during the lectures. I am thankful to Andreas Gute and to Manfred Ferstl from the University of Erlangen who took notes during the lectures and prepared the first draft with most of the Feynman diagrams. Many thanks also to Stephan Boettcher from Tel Aviv University for editing the manuscript.

Bibliography

[1] R. G. Roberts, *The structure of the proton* (Cambridge University Press, 1990).

[2] B. H. Wiik, in *Proceedings of the Workshop Physics at HERA*, edited by W. Buchmüller, G. Ingelman (Hamburg, Germany, 1991), p. 1.

[3] H1 Collab., I. Abt et al., *DESY 93-103* (1993).

[4] ZEUS Collab., M. Derrick et al., *DESY 1993* (1993).

[5] W. Bartel et al., in *Proceedings of the Workshop Future Physics at HERA*, edited by G. Ingelman, A. D. Roeck, R. Klanner (Hamburg, Germany, 1996), p. 1095.

[6] HERMES Collab., K. Coulter et al., *DESY-PRC 90/01* (1990).

[7] HERA-B Collab., T. Lohse et al., *DESY-PRC 94/02* (1994).

[8] G. Ingelman, R. Rückl, *Phys. Lett.* **B 201** (1988) 369.

[9] H1 Collab., I. Abt et al., *Phys. Lett.* **B 324** (1994) 241.

[10] ZEUS Collab., M. Derrick et al., *Phys. Rev. Lett.* **75** (1995) 1006.

[11] ZEUS Collab., M. Derrick et al., *Z. Phys.* **C 67** (1995) 81.

[12] H1 Collab., T. Ahmed et al., *Phys. Lett.* **B 346** (1995) 415.

[13] ZEUS Collab., M. Derrick et al., *Phys. Lett.* **B 363** (1995) 201.

[14] H. Abramowicz, in *Proceedings of the International Conference on High Energy Physics* (Warsaw, Poland, 1996), (and references therein).

[15] ZEUS Collab., M. Derrick et al., *Z. Phys.* **C 72** (1996) 399.

[16] H1 Collab., S. Aid et al., *Nucl. Phys.* **B 470** (1996) 3.

[17] A. Levy, U. Maor, *Phys. Lett.* **B 182** (1986) 108.

[18] H. Abramowicz et al., *Phys. Lett.* **B 269** (1991) 465.

[19] A. Marcus, Energy dependence of the $\gamma^* p$ cross section, Master's thesis, Tel Aviv University, 1996, TAUP 2350-96.

[20] ZEUS Collab., M. Derrick et al., *Phys. Lett.* **B 315** (1993) 481.

[21] H1 Collab., T. Ahmed et al., *Nucl. Phys.* **B 429** (1994) 477.

[22] M. Gell-Mann, Y. Ne'eman, *The Eightfold Way* (Benjamin, New York, 1964).

[23] E. Leader, Lecture Notes, 1987.

[24] P. D. B. Collins, A. D. Martin, *Hadron Interactions* (Adam Hilger, 1984).

[25] G. F. Chew, S. C. Frautschi, *Phys. Rev. Lett.* **8** (1962) 41.

[26] M. Froissart, *Phys. Rev.* **123** (1961) 1053.

[27] A. Martin, *Nuovo Cimento* **42** (1966) 930.

[28] K. Goulianos, *Phys. Rep.* **C 101** (1983) 169, (and references therein).

[29] I. Y. Pomeranchuk, *Sov. Phys. JETP* **7** (1958) 499.

[30] G. Jaroszkiewicz, P. V. Landshoff, *Phys. Rev.* **D 10** (1974) 170.

[31] A. Donnachie, P. V. Landshoff, *Phys. Lett.* **B 296** (1992) 227.

[32] J. J. Sakurai, *Ann. Phys.* **11** (1960) 1.

[33] G. A. Schuler, J. Terron, in *Proceedings of the Workshop Physics at HERA*, edited by W. Buchmüller, G. Ingelman (Hamburg, Germany, 1991), p. 599.

[34] H1 Collab., T. Ahmed et al., *Z. Phys.* **C 66** (1995) 525.

[35] D. Kisielewska et al., *DESY-HERA 85-25* (1985).

[36] J. Andruszkow et al., *DESY 92-066* (1992).

[37] K. Piotrzkowski, *DESY-F35D-93-06* (1993).

[38] ZEUS Collab., M. Derrick et al., *Phys. Lett.* **B 293** (1992) 465.

[39] H1 Collab., T. Ahmed et al., *Phys. Lett.* **B 299** (1992) 374.

[40] F. Eisele, in *Proceedings of the International Europhysics Conference on High Energy Physics*, edited by J. Lemonne, C. V. Velde, F. Verbeure (Brussels, Belgium, 1995).

[41] A. Caldwell, in *Proceedings of the 17th International Symposium on Lepton-Photon Interactions*, edited by Z. Zhi-Peng, C. He-Sheng (Beijing, China, 1995), p. 505.

[42] S. Bentvelsen, J. Engelen, P. Koijman, in *Proceedings of the Workshop Physics at HERA*, edited by W. Buchmüller, G. Ingelman (Hamburg, Germany, 1991), p. 23.

[43] F. Jacquet, A. Blondel, in *Proceedings of the study of an ep facility for Europe*, edited by U. Amaldi (1979), p. 391.

[44] M. N. Rosenbluth, *Phys. Rev.* **79** (1950) 615.

[45] E. Leader, E. Predazzi, *An Introduction to Gauge Theories and the New Physics* (Cambridge University Press, 1982).

[46] F. J. Gilman, *Phys. Rev.* **167** (1968) 1365.

[47] L. N. Hand, *Phys. Rev.* **129** (1963) 1834.

[48] H. Spiesberger et al., in *Proceedings of the Workshop Physics at HERA*, edited by W. Buchmüller, G. Ingelman (Hamburg, Germany, 1991), p. 798.

[49] C. G. Callan, D. Gross, *Phys. Rev. Lett.* **22** (1969) 156.

[50] H. Abramowicz, A. Caldwell, R. Sinkus, *Nucl. Instrum. Meth.* **A 365** (1995) 569.

[51] L. W. Whitlow et al., *Phys. Lett.* **B 250** (1990) 193.

[52] NMC Collab., M. Arneodo et al., *hep-ph/9610231*, accepted for publication in Nuc. Phys. B.

[53] H. Abramowicz et al., *DESY 90-019*

[54] J. C. Collins, D. E. Soper, G. Sterman, in *Perturbative Quantum Chromodynamics*, edited by A. H. Mueller (World Scientific, Singapore, 1989).

[55] G. 't Hooft, M. Veltman, *Nucl. Phys.* **B 50** .

[56] V. N. Gribov, L. N. Lipatov, *Sov. J. Nucl. Phys.* **15** (1972) 438,675.

[57] Y. L. Dokshitzer, *Sov. Phys. JETP* **46** (1977) 641.

[58] G. Altarelli, G. Parisi, *Nucl. Phys.* **B 126** (1977) 298.

[59] A. Levy, in *Proceedings of the International Europhysics Conference on High Energy Physics*, edited by J. Lemonne, C. V. Velde, F. Verbeure (Brussels, Belgium, 1995), p. 700.

[60] E. A. Kuraev, L. N. Lipatov, V. S. Fadin, *Sov. Phys. JETP* **44** (1976) 443.

[61] E. A. Kuraev, L. N. Lipatov, V. S. Fadin, *Sov. Phys. JETP* **45** (1977) 199.

[62] Y. Y. Balitski, L. N. Lipatov, *Sov. J. Nucl. Phys.* **28** (1978) 822.

[63] A. H. Mueller, *Nucl. Phys.* **B 307** (1988) 34.

[64] A. H. Mueller, N. Navelet, *Nucl. Phys.* **B 282** (1987) 727.

[65] M. Ciafaloni, *Nucl. Phys.* **B 296** (1988) 49.

[66] G. Marchesini, *Nucl. Phys.* **B 445** (1995) 49.

[67] S. Catani, F. Fiorani, G. Marchesini, *Nucl. Phys.* **B 336** (1990) 18.

[68] L. V. Gribov, E. M. Levin, M. G. Ryskin, *Phys. Rep.* **C 100** (1983) 1.

[69] E. Gotsman, E. Levin, U. Maor, *Phys. Lett.* **B 379** (1996) 186.

[70] A. D. Martin, R. G. Roberts, W. J. Stirling, *Phys. Lett.* **B 354** (1995) 155.

[71] A. D. Martin, R. G. Roberts, W. J. Stirling, *RAL-TR-96-037* (1996) .

[72] R. Brock et al., *Rev. Mod. Phys.* **67** (1995) 157.

[73] M. Gluck, E. Reya, A. Vogt, *Z. Phys.* **C 67** (1995) 433.

[74] A. Donnachie, P. V. Landshoff, *Z. Phys.* **C 61** (1994) 139.

[75] K. Prytz, *Phys. Lett.* **B 311** (1993) 286.

[76] K. Prytz, *Phys. Lett.* **B 332** (1994) 393.

[77] R. K. Ellis, Z. Kunszt, E. M. Levin, *Nucl. Phys.* **B 420** (1994) 517.

[78] H1 Collab., S. Aid et al., *Nucl. Phys.* **B 449** (1995) 3.

[79] H1 Collab., S. Aid et al., *Nucl. Phys.* **B 472** (1996) 3.

[80] ZEUS Collab., M. Derrick et al., ICHEP96, pa02-047.

[81] ZEUS Collab., M. Derrick et al., *Phys. Lett.* **B 349** (1995) 225.

[82] ZEUS Collab., presented by J. Bulmahn, ICHEP96, pa02-028.

[83] H1 Collab., S. Aid et al., *Nucl. Phys.* **B 472** (1996) 32.

[84] H1 Collab., S. Aid et al., *Z. Phys.* (1996) , to be published.

[85] ZEUS Collab., M. Derrick et al., *Phys. Lett.* **B 350** (1995) 120.

[86] M. G. Ryskin et al., *hep-ph/9511228* (1995) .

[87] B. L. Ioffe, *Phys. Lett.* **B 30** (1969) 123.

[88] B. L. Ioffe, V. A. Khoze, L. N. Lipatov, *Hard Processes* (North–Holland, 1984), p. 185.

[89] T. H. Bauer et al., *Rev. Mod. Phys.* **50** (1978) 261.

[90] J. C. Sens, in *Proceedings of the VIIIth International Workshop on Photon-Photon Collisions*, edited by U. Karshon (Shoresh, Israel, 1988), p. 143.

[91] V. M. Budnev et al., *Phys. Rep.* **C 15** (1975) 181.

[92] C. F. von Weizsäcker, *Z. Phys.* **88** (1934) 612.

[93] E. J. Williams, *Phys. Rev.* **45** (1934) 729.

[94] C. Berger, W. Wagner, *Phys. Rep.* **C 146** (1987) 1.

[95] H. Abramowicz et al., *Int. J. Mod. Phys.* **A 8** (1993) 1005.

[96] R. J. D. Witt et al., *Phys. Rev.* **D 19** (1979) 2046.

[97] C. Peterson, T. F. Walsh, P. M. Zerwas, *Nucl. Phys.* **B 229** (1983) 301.

[98] M. Glück, E. Reya, *Phys. Rev.* **D 28** (1983) 2749.

[99] A. Levy, *J. Phys.* **G 19** (1993) 1489.

[100] ZEUS Collab., M. Derrick et al., *Phys. Lett.* **B 297** (1992) 404.

[101] H1 Collab., T. Ahmed et al., *Phys. Lett.* **B 297** (1992) 205.

[102] ZEUS Collab., M. Derrick et al., *Phys. Lett.* **B 354** (1995) 163.

[103] E. Witten, *Nucl. Phys.* **B 120** (1977) 189.

[104] G. Rossi, *Phys. Rev.* **D 29** (1984) 852.

[105] OPAL Collab., presented by J. Lauber, ICHEP96, pa03-007.

[106] M. Gluck, E. Reya, A. Vogt, *Phys. Rev.* **D 45** (1992) 3986.

[107] L. E. Gordon, J. K. Storrow, *Z. Phys.* **C 56** (1992) 307.

[108] G. A. Schuler, T. Sjostrand, *Z. Phys.* **C 68** (1995) 607.

[109] J. H. Field, F. Kapusta, L. Poggioli, *Phys. Lett.* **B 181** (1986) 362.

[110] M. Drees, K. Grassie, *Z. Phys.* **C 28** (1985) 451.

[111] H. Abramowicz, K. Charchula, A. Levy, *Phys. Lett.* **B 269** (1990) 450.

[112] H1 Collab., T. Ahmed et al., *Nucl. Phys.* **B 445** (1995) 195.

[113] A. Levy, in *Proceedings of the Workshop on Deep Inelastic Scattering*, edited by G. D'Agostini, A. Nigro (Rome, Italy, 1996).

[114] PLUTO Collab.,Ch. Berger et al., *Phys. Lett.* **B 142** (1984) 119.

[115] ZEUS Collab., M. Derrick et al., EPS-ICHEP95, EPS-0384.

[116] A. H. Mueller, *Phys. Rev.* **D 2** (1970) 2963.

[117] R. D. Field, G. C. Fox, *Nucl. Phys.* **B 80** (1974) 367.

[118] M. Kasprzak, Ph.D. thesis, Warsaw University, 1996, DESY F35D-96-16.

[119] B. Burow, Ph.D. thesis, University of Toronto, 1994, DESY F35D-94-01.

[120] M. Krzyzanowski, Ph.D. thesis, Warsaw University, 1997.

[121] H1 Collab., S. Aid et al., *Z. Phys.* **C 69** (1995) 27.

[122] ZEUS Collab., M. Derrick et al., *Phys. Lett.* **B 338** (1994) 483.

[123] H1 Collab., S. Aid et al., *Z. Phys.* **C 70** (1996) 609.

[124] H1 Collab., T. Ahmed et al., *Phys. Lett.* **B 348** (1995) 681.

[125] H. Abramowicz, L. Frankfurt, M. Strikman, *DESY 95-047*

[126] UA8 Collab., R. Bonino et al., *Phys. Lett.* **B 211** (1988) 239.

[127] UA8 Collab., A. Brandt et al., *Phys. Lett.* **B 297** (1992) 417.

[128] ZEUS Collab., M. Derrick et al., *Phys. Lett.* **B 332** (1994) 228.

[129] H1 Collab., T. Ahmed et al., *Nucl. Phys.* **B 435** (1995) 3.

[130] ZEUS Collab., M. Derrick et al., *Z. Phys.* **C 68** (1995) 569.

[131] G. Ingelman, P. E. Schlein, *Phys. Lett.* **B 152** (1985) 256.

[132] A. Donnachie, P. V. Landshoff, *Phys. Lett.* **B 191** (1987) 309.

[133] A. Donnachie, P. V. Landshoff, *Nucl. Phys.* **B 303** (1988) 634.

[134] ZEUS Collab., M. Derrick et al., *Phys. Lett.* **B 356** (1995) 129.

[135] H1 Collab., presented by J. P. Phillips, ICHEP96, pa02-061.

[136] A. Metha for the H1 Colaboration, in *Proceedings of the Conference on Hard Diffractive Scattering* (Eilat, Israel, 1996), p. 710.

[137] ZEUS Collab., presented by G. Barbagli, ICHEP96, pa02-026.

[138] ZEUS Collab., M. Derrick et al., *Z. Phys.* **C 70** (1996) 391.

[139] J. C. Collins, J. Kwiecinski, *Nucl. Phys.* **B 316** (1989) 307.

[140] J. Kwiecinski, A. D. Martin, P. J. Sutton, *Phys. Rev.* **D 44** (1991) 2640.

[141] A. Donnachie, P. V. Landshoff, *Nucl. Phys.* **B 244** (1984) 322.

[142] A. Kaidalov, L. Ponomarev, K. A. Ter-Martirosyan, *Sov. J. Nucl. Phys.* **44** (1986) 468.

[143] A. Capella et al., *Phys. Lett.* **B 337** (1994) 358.

[144] J. Kwiecinski, B. Badelek, *Z. Phys.* **C 43** (1989) 251.

[145] B. Badelek, J. Kwiecinski, *Phys. Lett.* **B 295** (1992) 263.

[146] Q. Zhu for the ZEUS Colaboration, in *Proceedings of the Workshop on Deep Inelastic Scattering*, edited by G. D'Agostini, A. Nigro (Rome, Italy, 1996).

[147] A. V. Kotwal for the E665 Colaboration, in *Proceedings of the XXXth Recontres de Moriond, QCD and High Energy Interactions* (Moriond, 1995).

[148] ZEUS Collab., M. Derrick et al., *Z. Phys.* **C 65** (1995) 379.

[149] H1 Collab., T. Ahmed et al., *Nucl. Phys.* **B 439** (1995) 471.

[150] ZEUS Collab., M. Derrick et al., *Z. Phys.* **C 69** (1995) 39.

[151] H1 Collab., S. Aid et al., *Nucl. Phys.* **B 463** (1996) 3.

[152] ZEUS Collab., M. Derrick et al., *DESY 96-159*, accepted for publ. in Z. Phys. C.

[153] ZEUS Collab., M. Derrick et al., *Phys. Lett.* **B 377** (1996) 259.

[154] H1 Collab., S. Aid et al., *Nucl. Phys.* **B 472** (1996) 3.

[155] ZEUS Collab., presented by J. Bulmahn, ICHEP96, pa02-028.

[156] H1 Collab., S. Aid et al., *Nucl. Phys.* **B 468** (1996) 3.

[157] ZEUS Collab., M. Derrick et al., *Phys. Lett.* **B 380** (1996) 220.

[158] S. J. Brodsky et al., *Phys. Rev.* **D 50** (1994) 3134.

[159] L. Frankfurt, W. Koepf, M. Strikman, *Phys. Rev.* **D 54** (1996) 3194.

[160] J. D. Bjorken, in *Proceedings of the Workshop on Deep Inelastic Scattering*, edited by A. Levy (Eilat, Israel, 1994), p. 151.

[161] J. D. Bjorken, in *Proceedings of the International Symposium on Electron and Photon Interactions at High Energies* (Cornell, 1971), p. 281.